ABSTRACT

Title of dissertation: CHARACTERISTICS OF PLASMA SOLITONS PRODUCED BY SMALL ORBITAL DEBRIS

Alexis Truitt
Doctor of Philosophy, 2020

Dissertation directed by: Professor Christine Hartzell
Department of Aerospace Engineering

Sub-centimeter orbital debris is currently undetectable using ground-based radar and optical methods. However, pits in Space Shuttle windows produced by paint chips demonstrate that small debris can cause serious damage to spacecraft. Recent analytical, computational and experimental work has shown that charged objects moving quickly through a plasma will cause the formation of plasma density solitary waves, or solitons. Due to their exposure to the solar wind plasma environment, even the smallest space debris will be charged. Depending on the debris size, charge and velocity, debris may produce plasma solitons that propagate along the debris velocity vector and could be detected with existing sensor technology. Plasma soliton detection would be the first collision-free method of mapping the small debris population.

The first major contribution of this thesis is the identification of orbital locations where solitons will be produced, as a function of debris size and speed. Using the Chan & Kerkhoven pseudospectral method, we apply the Forced Korteweg-de

Vries equation to describe the amplitude, width, and production frequency of solitons that may be produced by mm-cm scale orbital debris, as a function of the debris' size, velocity, and location (altitude, latitude, longitude) about Earth.

Analytical solutions result in solitons that propagate forever without damping, assuming a uniform plasma environment. However, Earth's space plasma is complex, with processes that could cause the solitons to dampen. Damped solitons will have a limit to the distance they will travel before becoming undetectable. For our second major contribution, we calculated the propagation distance of solitons in the presence of damping processes. We applied the Damped Forced Korteweg-de Vries equation to calculate the damping rate of the solitons, and estimate the resulting soliton propagation distance. We demonstrate that Landau damping dominates over collisional damping for these solitons. It is necessary to understand the damping of solitons in order to assess the feasibility of on-orbit debris detection.

In our first contribution, we demonstrate that one dimensional simulations are sufficient to model the orbital debris solitons that propagate along the debris velocity vector. However, in order to fully understand the soliton signatures in a 3D spatial environment, it is necessary to extend the Damped Forced Korteweg-de Vries model to three spatial dimensions. For our final major contribution, we apply the Damped Forced Kadomtsev-Petviashvili Equation, which is a natural extension for waves described by the Damped Forced Korteweg-de Vries equation. Transverse solitonic perturbations extend across the width of the debris, with predictable amplitudes and speeds that can be approximated by the one dimensional Damped Forced Korteweg-de Vries equation at the transverse soliton location. The trans-

verse perturbations form soliton rings that advance ahead of the debris in the three dimensional simulations, allowing for additional opportunity for detection.

With the current absence of a dedicated, calibrated, on-orbit debris detection sensor, plasma soliton detection would be the first collision-free method of mapping the small debris population. The characteristics of plasma solitons described here are necessary to evaluate the feasibility of orbital debris detection via soliton detection with future debris detection systems.

CHARACTERISTICS OF PLASMA SOLITONS PRODUCED BY SMALL ORBITAL DEBRIS

by

Alexis S. Truitt

Dissertation submitted to the Faculty of the Graduate School of the
University of Maryland, College Park in partial fulfillment
of the requirements for the degree of
Doctor of Philosophy
2020

Advisory Committee:
Dr. Christine Hartzell, Chair/Advisor
Dr. David Akin
Dr. James Baeder
Dr. James Drake
Dr. Raymond Sedwick

Dedication

To my daughter, my greatest inspiration.

Acknowledgments

I owe my gratitude to all who have made this thesis possible.

First and foremost I'd like to thank my advisor, Dr. Christine Hartzell, for giving me the incredible opportunity to work on a project with immediate relevance to the safety of space navigation. I had been in the workforce for years before returning to school, however, she was patient and supportive as I relearned everything I forgot during my absence. Without her direction and guidance, the completion of this thesis would not have been realized. Christine is extraordinary individual, and I am beyond grateful for the opportunity to work with and learn from her.

I would also like to thank my thesis committee, Dr. David Akin, Dr. James Baeder, Dr. James Drake, and Dr. Raymond Sedwick, for sparing their time to provide invaluable feedback during this process, greatly improving several major aspects of this research.

My colleagues in the Planetary Surfaces and Spacecraft Lab have been incredibly supportive during this process. Dr. Dylan Carter, Dr. Anthony DeCicco, Thomas Leps, Anand Patel, Charles Pett, and Jackson Shannon all helped me to study for the qualifying and comprehensive exams, making sure that I was prepared to answer a multitude of questions. They also provided great feedback and suggestions on my research topic.

I owe my deepest thanks to my family. My mother has always nurtured my childhood aspirations, and instilled in me the persistence and work ethic necessary to fulfill those dreams. All of my family members have entertained my various

childhood space hypotheses, participated in my random science experiments, and ultimately helped to build my confidence in STEM to pursue a career in space, in an environment where STEM careers were nonexistent. This thesis would not have been possible without the unwavering support from my husband, who encouraged me to return to school and kept me grounded throughout the entire process. A special thanks goes to our daughter, who kept my spirits up during the most challenging tasks, serving as my tutor, correcting my homework, and providing entertainment with musical performances before my exams.

I would like to acknowledge financial support from my employer, who also allowed me to take time off to complete this thesis. More importantly, I would like to thank my mentors for their advice and inspiration.

I cannot possibly thank everyone who provided assistance with this thesis, and hope that this work may contribute to safety and resilience in the exploration of space.

Table of Contents

List of Tables

List of Figures

Chapter 1: Introduction and Motivation

Orbital debris collisions are a significant risk to Earth-orbiting spacecraft. With an average impact velocity of 10 km/s in low Earth orbit (LEO), even the smallest pieces of debris can cause serious damage, as demonstrated by the 3.8 mm diameter pit produced by a 0.2 mm paint chip on STS-7 [3]. Currently, there are over 500,000 debris between 1 and 10 cm in diameter, and over 100 million particles smaller than 1 cm [4, 5] orbiting the Earth. The debris population is dynamic due to the influence of drag, driving the need for persistent monitoring. However, sub-centimeter debris cannot be detected with ground based methods, and on-orbit detectors (e.g., the Long Duration Exposure Facility) can only sample the population at the detector altitude. Since the retirement of the Space Shuttle program in 2011, NASA no longer has a dedicated, calibrated on-orbit sub-centimeter orbital debris detection sensor [6, 7].

Orbital debris becomes charged due to its interaction with the solar wind plasma and the solar UV radiation [8]. It has been theorized that charged orbital debris will cause perturbations in the ion density in the ionospheric plasma, creating ion acoustic solitary waves (IASWs, or solitons) [9]. Sen *et al.* conducted computational simulations [9, 10] and experiments [11] to investigate the general properties

of plasma solitons produced by charged debris. Solitons are solitary waves that preserve their velocity and shape during translation, assuming transmission through a uniform, constant medium. Solitons remain unaltered if colliding with other solitons. The product of a soliton's amplitude with the square of its width remains constant, and solitons are generated at predictable intervals depending on the amplitude of the source. Solitons can be found throughout nature in a variety of media, to include shallow water, the atmosphere, and plasma [1, 12, 13, 14, 15, 16].

In Chapter 3, we derive the Forced Korteweg-de Vries equation from the plasma fluid equations for orbital debris, and apply the Chan & Kerkhoven pseudospectral method to simulate undamped solitons generated by debris, considering relevant ionospheric plasma properties, with a special emphasis on precursor solitons, which advance upstream of the debris and propagate along the debris velocity vector. Regions where precursor solitons could be generated were identified using the plasma conditions downloaded from the International Reference Ionosphere (IRI) model [17], as a function of the altitude, latitude, local time, and debris size. The formation of a precursor soliton depends on the relative velocity between the ions and the orbital debris. The range of velocities for which precursor solitons can be generated are calculated. Finally, we calculate the range of orbital eccentricities, and the percentage of each altitude where precursors could be created as a function of debris size.

Analytical solutions result in solitons that propagate forever without damping, assuming a uniform environment. However, Earth's space plasma is complex and influenced by seasonal and diurnal effects. A nonuniform environment or kinetic col-

lisions between solitons and ions or electrons in the plasma could cause the solitons to dampen. Damped solitons will have a limit to the distance they will travel before becoming undetectable. In Chapter 4, we investigate the propagation distance of solitons in the presence of damping processes. We apply the Damped Forced Korteweg-de Vries (dfKdV) equation, derived from the plasma fluid equations, and simulate the propagation of pinned and precursor solitons in the presence of damping processes. These propagation distances are necessary to assess the detectability of precursor solitons via satellite or ground observations, the time required to map detectable debris, and the number of sensors needed for mapping in a given mission window.

Chapter 3 demonstrates that one dimensional simulations are sufficient to model the orbital debris solitons, which propagate along the debris velocity vector. However, in order to fully understand the soliton signatures in a 3D spatial environment, it is necessary to extend the dfKdV model to three spatial dimensions. In Chapter 5, we will apply the Damped Forced Kadomtsev-Petviashvili Equation (dfKP), which is a natural extension for waves described by the dfKdV equation. Soliton characterization in three spatial dimensions can allow for additional opportunity to measure previously undetectable orbital debris, in a region where the characteristics of the sub-centimeter debris population are largely uncertain.

1.1 Contributions

This thesis is concerned with the prediction of the signatures of plasma density waves created by the presence of charged sub-centimeter orbital debris, potentially enabling the design of collision-free detection systems for the small debris population. The main contributions of this work are:

- Theoretical development to apply the Forced Korteweg-de Vries equation to the orbital debris plasma density soliton system (Chapter 3).
- Creation of models to predict soliton amplitude, width and speed as a function of debris size and speed (Chapter 3).
- Identification of the orbital altitudes and latitudes where solitons can be created as a function of debris size and speed (Chapter 3).
- Calculation of the propagation distance of solitons in the presence of relevant damping processes (Chapter 4).
- Extension of the one dimensional predictions to three spatial dimensions (Chapter 5).

1.2 Publications

The publications related to this thesis are listed below for reference.

- Truitt, A. S., and Hartzell, C. M., "Simulating Plasma Solitons from Orbital

Debris using the Forced Korteweg–de Vries Equation," Journal of Spacecraft and Rockets, accepted.

- Truitt, A. S., and Hartzell, C. M., "Simulating Damped Ion Acoustic Solitary Waves from Orbital Debris," Journal of Spacecraft and Rockets, accepted.

- Truitt, A. S., and Hartzell, C. M., "3D Kadomtsev-Petviashvili Damped Forced Ion Acoustic Solitary Waves from Orbital Debris," Journal of Spacecraft and Rockets, submitted.

- Truitt, A. S., and Hartzell, C. M., "Characteristics of Plasma Solitons Produced by Small Orbital Debris," First International Orbital Debris Conference, Dec 2019.

Chapter 2: Literature Review

While orbital debris solitons have not yet been detected, current orbital debris detection methods, as well as prior research on solitons in a variety of fluid systems, are relevant to assess whether orbital debris will produce detectable solitons. The soliton research can be divided into three categories: observational evidence of solitons, computational simulation of solitons, and experimental production of solitons in a laboratory environment.

2.1 Orbital Debris Detection

Small orbital debris has become a great hazard to Earth orbiting spacecraft. Debris smaller than 1 cm has shown the ability to chip ISS windows, penetrate extravehicular activity (EVA) suits, and damage spacecraft components such as radiators, thermal protection system (TPS) tiles, and cargo bay walls [5, 18].

NASA estimates that there are over 100 million particles smaller than 1 cm orbiting the Earth. However, estimates for sub-centimeter debris are largely based on collisional detections during the space shuttle mission, which has now retired. These collisional detections were restricted to measuring debris strikes at altitudes below 600 km, the upper limit of space shuttle operations, and were then used to

estimate the small debris population at a range of altitudes. Further, for debris between 2 mm - 10 cm in LEO, the exposed surface will need to be larger than that of a typical satellite in order to obtain a meaningful sample of impacts. [18].

While ground based sensors continue to improve their detection capabilities, the ground sensor detection sensitivity rapidly decreases with increasing altitude, and is limited to observing high latitudes. The ground sensors in the Space Surveillance Network (SSN) are able to detect 10 cm objects at 2000 km altitude in LEO and 1 m objects at 35,786 km altitude in GEO [18]. Unfortunately, ground based sensors are not able to track sub-centimeter objects due debris' relatively high angular velocity, and remain in staring mode to count the number of objects passing through their small fields of view [18]. The largest source of uncertainty exists in the ability to interpret the signal strength in order to determine the size or mass of the object passing through the field of view. Additionally, debris from objects in a Molniya-type orbit cannot be detected, since the U.S. ground-based sensor systems are in the Northern Hemisphere [18].

Most of the small orbital debris population resides in high LEO, with a mean altitude of 850 km [5]. More orbital debris is created than removed due to the diminished atmospheric drag at high altitudes, making our current orbit characterization for sub-centimeter debris even more uncertain [19].

An estimate from the SSN for the number of debris greater than 10 cm is displayed in Fig 2.1, published by the NASA Orbital Debris Program office [5]. Two events are responsible for adding 40% to the LEO debris estimates: the Chinese Anti-satellite Test (ASAT) in 2007 and the collision of the Cosmos–Iridium satellites

in 2009. These two events significantly increased the challenges of operating in LEO.

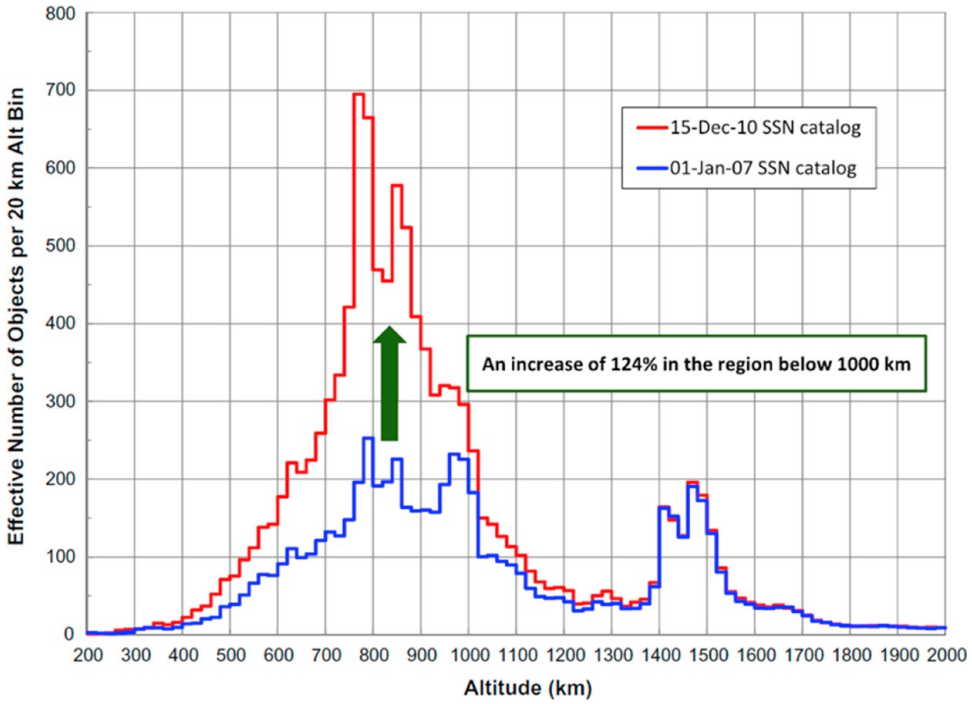

Figure 2.1: Space Surveillance Network estimate of the number of debris objects greater than 10 cm as a function of altitude. Image from NASA/ODPO [5].

With the increase in the number of satellite launches over time, there is potential for rapid growth of the debris population. Therefore, active means are necessary for quickly characterizing the dynamic orbital debris environment, allowing for the ability to prevent satellite damage through mitigation and remediation. A non-collisional capability to detect sub-centimeter debris from the ground and *in situ* with existing sensor technology would provide for the most immediate contribution for understanding the small debris population.

2.2 Observation of Solitons

The first recorded solitary wave was observed by John Scott Russell in 1834, who observed a solitary wave in the Union Canal in Scotland, as shown in Fig 2.2(a). He then reproduced a soliton in a lab experiment using a wave tank, and described the phenomenon in an 1844 publication [20]. Russell described the wave in the Union Canal as follows: "I was observing the motion of a boat which was rapidly drawn along a narrow channel by a pair of horses, when the boat suddenly stopped – not so the mass of water in the channel which it had put in motion; it accumulated round the prow of the vessel in a state of violent agitation, then suddenly leaving it behind, rolled forward with great velocity, assuming the form of a large solitary elevation, a rounded, smooth and well-defined heap of water, which continued its course along the channel apparently without change of form or diminution of speed. I followed it on horseback, and overtook it still rolling on at a rate of some eight or nine miles an hour, preserving its original figure some thirty feet long and a foot to a foot and a half in height." [20] In 1895, Diederick Korteweg and Gustav de Vries derived a nonlinear partial differential equation to describe Russell's soliton experiment, now known as the Korteweg–de Vries (KdV) Equation [21]:

$$\frac{\partial U}{\partial t} + U\frac{\partial U}{\partial x} + \frac{\partial^3 U}{\partial x^3} = 0 \tag{2.1}$$

More recently, oceanic solitons have been observed with satellite-based synthetic aperture radar [14, 16], with an example shown in Fig 2.2(b). These oceanic

surface solitons can be thought of as analogs of solitons generated by orbital debris. Historically, oceanic solitons were described as bands of choppy water or ripplings in the presence of local bathymetry, observed even in calm weather at well known locations. These solitons are often generated when a current of shallow water flows over a submerged obstacle. The solitons propagate radially outward from the obstacle, forming semicircular rings of solitary waves. The height, width, and speed of the solitons, as well as the extent of the semicircular arc, depend on the speed of the current, depth of the water, and the size and shape of the obstacle.

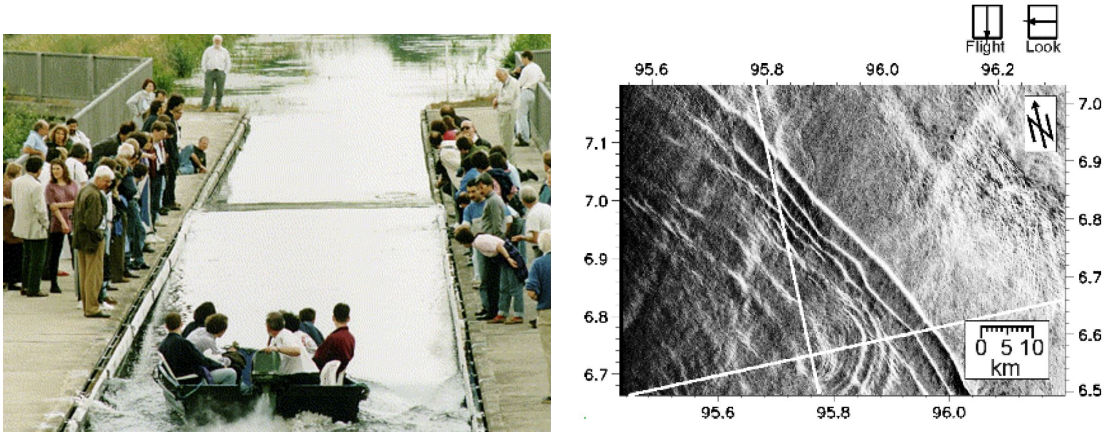

(a) Soliton in Channel

(b) Oceanic Soliton

Figure 2.2: (a) A soliton observed on the Scott Russell Aqueduct on the Union Canal in 1995. Image reproduced from [22]. (b) ERS-2 SAR image of solitons generated near the shallowest point (crosshair) of the Dreadnought Bank in the Andaman Sea on May 4, 1996. Secondary solitons are also observed due to activity further west. Image from Alpers et al. [16].

While many variations of the KdV equation have been studied, we will focus on the forced KdV (fKdV) equation, where the soliton wave, U, is generated due to the presence of a forcing term, $f(x,t)$, as shown in Eqn 2.2. In oceanic solitons,

the submerged obstacle acts as the force term. Analogously, in the ionosphere, the charged debris is represented by the forcing term.

$$\frac{\partial U}{\partial t} + U\frac{\partial U}{\partial x} + \frac{\partial^3 U}{\partial x^3} = f(x,t) \tag{2.2}$$

While plasma solitons resulting from charged orbital debris have not yet been detected, the existence of ion acoustic solitons in unmagnetized plasma due to other disturbances has already been demonstrated [15]. Solitons have also previously been observed in the 3D plasma environment of the ionosphere. The Freja scientific satellite observed nonlinear density waves in the upper ionosphere [12], and simulations were conducted to support the observations [13]. Solitons were also observed by the Cluster II satellites at the Earth's magnetopause, created due to turbulence at the boundary [23].

2.3 Computational Simulation of Solitons

In 1965, Norman Zabusky and Martin Kruskal were the first known to conduct numerical experiments with the KdV equation, using a finite difference method. They showed that travelling waves can be produced by specific initial conditions, similar to the wave described by Russell. In their computational studies, they observed that the travelling waves remain unaltered when colliding with other travelling waves, and this particle-like behavior of the waves is why the Zabusky and Kruskal called the travelling waves "solitons" [24].

The work done by Zabusky and Kruskal allowed for exact solutions of the KdV

equation to be derived. In 1975, Bona and Smith [25] published the first analytical solitons for the KdV equation. Subsequently, in 1978, Fornberg and Whitham [26] developed a Fourier pseudospectral method for the KdV equation, which uses three Fourier transforms per time step. The development of this pseudospectral scheme was the first of many numerical methods for solving the KdV, including a Petrov-Galerkin method, a hopscotch method by Geig and Morris, and another pseudospectral scheme by Chan and Kerkhoven [27] which uses a Crank-Nicholson method for the spatial derivatives, reducing the number of Fourier transforms required per time step. Thus, Chan-Kerkhoven is recognized as the fastest method to date for solving the KdV equations [28].

In [9], Sen *et al.* derived the fKdV equation from the plasma fluid equations for an orbital debris system, showing that the orbital debris will influence the density of ions and electrons in the Poisson equation and consequently be represented as the forcing function in the fKdV equation. Notional results were simulated for plasma density solitons produced by orbital debris, with the charged orbital debris source approximated as a Gaussian shape. A variety of constants were applied to the system to observe how the plasma density solitons may change in size and frequency. Subsequently, Tiwari and Sen [10] published computational results investigating the existence region of pinned and pursor solitons as a function of forcing function speed and soliton amplitude.

2.4 Experimental Production of Solitons

Solitons have been studied experimentally in a variety of fluid systems. The generation of solitons in electron beam experiments was recorded as early as 1939, by Simon Ramo and W. C. Hahn [29, 30]. For shallow water waves, Feir published results of solitons from wave pulse experiments in 1967 [31]. Additionally, Yuen and Lake observed solitons in deep water experiments [32, 33] in 1975 and 1982.

In addition to their theoretical results [9], Sen *et al.* have successfully created solitons in a dusty plasma laboratory experiment [11]. In their experiment, nonlinear solitary dust acoustic waves are produced by a supersonic mass flow of dust particles over an electrostatic potential hill. Micron-sized kaolin particles were negatively charged and levitated in the argon plasma, which was confined due to a charged copper wire creating a potential hill barrier. The production of solitons was investigated as a function of fluid speed by systematically reducing the height of the barrier. Results show that the unique properties of ion acoustic solitons, such as their amplitude and width, are predictable and depend on the relative speed between the charged source and the fluid medium.

2.5 Summary

Solitons have been observed experimentally in a variety of applications, including fully 3D systems and space plasmas. The observation of plasma density solitons in the Earth's plasma environment due to other disturbances, combined

with the computational and experimental work done by Sen *et al.* for orbital debris, suggest that orbital debris may produce plasma density solitons as well. The referenced soliton computational and experimental studies serve as the foundation for additional theoretical development and application to existing models of the Earth's ionosphere.

We build on Sen *et al.*'s work by simulating solitons generated using relevant ionospheric plasma and debris properties, with a special emphasis on precursor solitons, which advance upstream of the debris. We determine the debris size and velocity that will produce solitons, as well as the altitude range where solitons can be produced and their propagation distance in the presence of damping processes. We extend the one dimensional approximations to three spatial dimensions in order to understand the full 3D signature of the solitons. The characteristics of solitons generated by orbital debris will influence future evaluations of whether or not solitons can be detected *in situ* in order to identify orbital debris that is currently too small to be observed.

Chapter 3: Simulating Undamped Solitons from Orbital Debris in One Spatial Dimension

In this chapter, as published in [34], we will investigate Earth's plasma environment and the properties of charged orbital debris to evaluate whether solitons will be produced in their presence. Since Earth's plasma environment is dynamic and complex due to seasonal and diurnal processes, we will focus on average plasma parameters before applying an existing plasma model. We will seek to determine the altitude, latitude, and local time where solitons can be created as a function of debris size and speed.

The content of this chapter has been accepted for publication as Truitt and Hartzell, "Simulating Plasma Solitons from Orbital Debris using the Forced Korteweg–de Vries Equation," Journal of Spacecraft and Rockets, 2020. [34]

3.1 The Plasma Environment

The ionospheric plasma varies with altitude, latitude and illumination. Low Earth orbit (LEO, 200-1000 km altitude) lies within the ionosphere's F2 region. The mid-latitudes of the F2 region consist of low energy, high density plasma (see Table 3.1), and the dominant ion species is oxygen. Above the F2 layer, between

Table 3.1: Plasma properties in the mid-latitude ionosphere, derived from ground-based and space-based observations. V_d is the velocity of debris in a circular orbit.

	Low LEO [35]	High LEO 1 [36, 37, 38]	High LEO 2 [36, 37, 38]	GEO [39, 40]
Altitude (km)	700	1,200	1,400	35,786
Latitude (deg)	0-55	0-55	0-55	0-90
n_e (cm^{-3})	2x10^5	10^5	10^4	1
T_e (eV)	0.25	0.35	0.35	1,000
Ion Species	O^+	H^+	H^+	O^+ / H^+
m_i (m_p)	16	1	1	16 / 1
λ_D (cm)	0.83	1.38	4.36	23,504.00
V_d (km/s)	7.51	7.26	7.16	3.08
V_{ia} (km/s)	1.22	5.75	5.75	77.43 / 309.73

1000-2000 km altitude, the number of oxygen ions decreases and lighter ions such as hydrogen and helium become dominant. The plasma surrounding geostationary orbits is also high energy and low density, similar to the high latitude LEO regions. Nominal plasma properties for the mid-latitude regions are listed in Table 3.1 and were derived from various ground-based and space-based observations in [35, 36, 37, 38, 39, 40]. For GEO, the dominant ion could be oxygen or hydrogen depending on solar activity, so m_i and V_{ia} are listed for both species.

The high latitude, or polar, regions of LEO contain open magnetic field lines, allowing for the escape of particles as well as the entry of high energy particles from the solar wind. The combination of these processes, in addition to geomagnetic storms, creates a highly variable environment [41, 42]. Examples of the plasma environment at high latitudes are provided in Table 3.2. In general, the plasma density is 10-100x less than the density at mid-latitude regions, with areas of precipitating high energy electrons from the solar wind [41, 42]. For Polar LEO 1, the dominant ion could be oxygen or hydrogen depending on solar activity, so m_i and V_{ia} are listed

Table 3.2: Plasma properties in high-latitude ionosphere [41, 42].

	Polar LEO 1	Polar LEO 2	Polar LEO 3
Altitude (km)	600	600	950
Latitude (deg)	55-90	55-90	55-90
n_e (cm^{-3})	10	10^4	10^3
T_e (eV)	1,000	0.25	0.35
Ion Species	O^+ / H^+	O^+	H^+
m_i (m_p)	16 / 1	16	1
λ_D (cm)	7,432.00	3.72	13.91
V_d (km/s)	7.56	7.56	7.38
V_{ia} (km/s)	77.43 / 309.73	1.22	5.75

for both species.

3.2 Plasma Fluid Equations

In the LEO plasma environment, we can model the equations of state in the plasma using a fluid model. The fluid equations can be derived mathematically by taking moments of the Boltzmann equation. These moments are the standard plasma fluid equations for continuity, momentum, and Poisson's equation, and are used to derive the ion acoustic wave behavior:

$$\frac{\partial n}{\partial t} + \frac{\partial (nu)}{\partial x} = 0 \tag{3.1}$$

$$\frac{\partial u}{\partial t} + u\frac{\partial u}{\partial x} + \frac{\partial \phi}{\partial x} = 0 \tag{3.2}$$

$$\frac{\partial^2 \phi}{\partial x^2} - e^{\phi} + n = f(x,t) \tag{3.3}$$

where n is the ion density, u is the ion velocity, ϕ is the electrostatic potential, and $f(x,t)$ is a forcing function described as a charge density source [9].

We normalize the domain as follows:

$$n = \frac{n}{n_0}, \quad x = \frac{x}{\lambda_D}, \quad t = \frac{V_{ia}}{\lambda_D}t, \quad u = \frac{u}{V_{ia}}, \quad \phi = \frac{e\phi}{k_b T_e} \tag{3.4}$$

where n_0 is the initial ion density, $\lambda_D = \sqrt{\epsilon_o k_B T_e / q^2 n_e}$ is the Debye length, $V_{ia} = \sqrt{k_B T_e / m_i}$ is the ion acoustic velocity, k_B is the Boltzmann constant, m_i is the ion mass, and T_e is the electron temperature.

In the weakly nonlinear limit, we invoke the long wave assumption that the amplitude of the wave is much smaller than the length of the wave. In this weakly nonlinear limit, the plasma fluid equations can be approximated by the KdV Equation, derived by linearizing the plasma fluid equations using the reductive perturbation technique [43]. To conduct the perturbation analysis, we create stretched variables, ξ and τ, for the independent variables, x and t:

$$\xi = \epsilon^{1/2}(x - vt) \tag{3.5}$$

$$\tau = \epsilon^{3/2}t \tag{3.6}$$

$$\frac{\partial}{\partial x} = \epsilon^{1/2}\frac{\partial}{\partial \xi} \tag{3.7}$$

$$\frac{\partial}{\partial t} = -\epsilon^{1/2} v \frac{\partial}{\partial \xi} + \epsilon^{3/2} \frac{\partial}{\partial \tau} \tag{3.8}$$

We then expand the n, u, and ϕ around the unperturbed states in powers of ϵ, where ϵ is a small parameter that measures the weakness of dispersion.

$$n = 1 + \epsilon n_1 + \epsilon^2 n_2 + ... \tag{3.9}$$

$$u = 0 + \epsilon u_1 + \epsilon^2 u_2 + ... \tag{3.10}$$

$$\phi = 0 + \epsilon \phi_1 + \epsilon^2 \phi_2 + ... \tag{3.11}$$

$$f(x,t) = \epsilon^2 f(\xi, \tau) + ... \tag{3.12}$$

Next, we substitute Eqn 3.5-Eqn 3.12 into Eqn 3.1-Eqn 3.3. The perturbed continuity equation becomes:

$$\Big(-\epsilon^{1/2} v \frac{\partial}{\partial \xi} + \epsilon^{3/2} \frac{\partial}{\partial \tau}\Big)\Big(1 + \epsilon n_1 + \epsilon^2 n_2\Big) + \Big(\epsilon^{1/2} \frac{\partial}{\partial \xi}\Big)\Big(\Big(1 + \epsilon n_1 + \epsilon^2 n_2\Big)\Big(\epsilon u_1 + \epsilon^2 u_2\Big)\Big) = 0 \tag{3.13}$$

The perturbed momentum equation becomes:

$$\begin{aligned}\Big(-\epsilon^{1/2} v \frac{\partial}{\partial \xi} + \epsilon^{3/2} \frac{\partial}{\partial \tau}\Big)\Big(\epsilon u_1 + \epsilon^2 u_2\Big) + \Big(\epsilon u_1 + \epsilon^2 u_2\Big)\Big(\epsilon^{1/2} \frac{\partial}{\partial \xi}\Big)\Big(\epsilon u_1 + \epsilon^2 u_2\Big) \\ + \Big(\epsilon^{1/2} \frac{\partial}{\partial \xi}\Big)\Big(\epsilon \phi_1 + \epsilon^2 \phi_2\Big) = 0\end{aligned} \tag{3.14}$$

The perturbed Poisson equation, using a Taylor expansion of $e^{\phi} \approx 1 + \phi + \frac{\phi^2}{2}$

becomes:

$$\left(\epsilon^{1/2}\frac{\partial}{\partial\xi}\right)^2\left(\epsilon\phi_1+\epsilon^2\phi_2\right)-\left(1+\left(\epsilon\phi_1+\epsilon^2\phi_2\right)+\frac{1}{2}\left(\epsilon\phi_1+\epsilon^2\phi_2\right)^2\right) \\ +\left(1+\epsilon n_1+\epsilon^2 n_2\right)=\epsilon^2 f(\xi,\tau) \tag{3.15}$$

After comparing the coefficients of different powers of ϵ, and performing substitution in the set of resulting equations, we arrive at the forced Korteweg–de Vries (fKdV) Equation [9]:

$$\frac{\partial\phi}{\partial\tau}+\phi\frac{\partial\phi}{\partial\xi}+\frac{1}{2}\frac{\partial^3\phi}{\partial\xi^3}=\frac{1}{2}\frac{\partial f}{\partial\xi} \tag{3.16}$$

Understanding that fluctuations in the electrostatic potential, ϕ, will drive the nonlinear wave, U, we rewrite the equation using the traditional wave equation form and compare to the fKdV equation often seen in literature:

$$\frac{\partial U}{\partial\tau}+\mu\frac{\partial U}{\partial\xi}+\alpha U\frac{\partial U}{\partial\xi}+\beta\frac{\partial^3 U}{\partial\xi^3}=\frac{1}{2}\frac{\partial f}{\partial\xi} \tag{3.17}$$

In Eqn 3.17, U(ξ,τ) is the derived ion acoustic wave, manifested as an electric potential in the plasma surrounding the debris and a perturbation in the ion density. The spatial and temporal variables, ξ and τ, are the derived stretched coordinates of the initial boundary-value problem.

Soliton solutions can be derived for many mathematical and physical systems that are modeled by weakly nonlinear partial differential equations, and are caused when the nonlinear and dispersive forces are balanced. The coefficients α and β

define the weighting of the steepening and dispersion terms, and μ is the speed of the medium flowing over the submerged obstacle. Note that in our derivation of Eqn 3.16 for LEO plasma, $\alpha = 1$, $\beta = 1/2$, and $\mu = 0$ since our reference frame assumes that the medium is static and the submerged obstacle is in motion. The coefficients are discussed in further detail in 3.2.1.

Thus, the forced KdV equation has been derived from first principles to describe perturbations in the ion density as a result of charged debris, assuming: (a) a cold Maxwellian plasma ($T_i < T_e$), (b) a collisionless plasma, meaning that the dust density is negligible ($n_{dust} << n_{ions}$), (c) a weakly nonlinear system, where the amplitude of the wave is much smaller than the length of the wave, and (d) magnetic field effects are negligible and wave propagation can be described in a 1D system, further discussed in 3.2.1.

The forced KdV equation will be used in the remainder of this study. In the absence of a forcing term, Eqn 3.17 reduces to the standard unforced KdV equation in Eqn 3.18, which is often used in unforced, weakly nonlinear wave studies.

$$\frac{\partial U}{\partial \tau} + \alpha U \frac{\partial U}{\partial \xi} + \beta \frac{\partial^3 U}{\partial \xi^3} = 0 \tag{3.18}$$

While many studies detail the application of the unforced KdV equation for a variety of fluid systems, there are only a few that discuss application of the forced KdV equation. The works that discuss the generation of IASWs by orbital debris use the fully nonlinear plasma fluid equations instead of the fKdV [9, 10, 11]. Based on the properties of plasma in LEO, we estimate that the amplitude is much smaller

than the length of the waves, validating the long wave assumption and allowing for use of the fKdV equation to characterize the solitons. Detailed derivations of the fKdV equation can be found in [2, 44].

3.2.1 Derived Coefficients

Traditionally, the coefficients α and β, when applied to shallow water waves, describe the geometry of the water channel with respect to the flow of the medium and height of the obstacle at the floor of the channel [2, 44]. In our derivation of Eqn 3.16 for LEO plasma, assuming a collisionless Maxwellian plasma, $\alpha = 1$ and $\beta = 1/2$. We verify these coefficients through study of the derived coefficients for other plasma environments.

For IASWs, these coefficients have been derived in literature for complex plasmas consisting of strong magnetic fields, dust, and superthermal electrons with $\kappa-$distributions using a damped KdV (dKdV) equation as shown in Eqn 3.19, where γ is the coefficient for the additional damping term due to ion-neutral collisions [45, 46, 47, 48].

$$\frac{\partial U}{\partial \tau} + \alpha U \frac{\partial U}{\partial \xi} + \beta \frac{\partial^3 U}{\partial \xi^3} + \gamma U = 0 \tag{3.19}$$

It can be shown that for a cold plasma with negligible dust density and a weak magnetic field, the complex plasma coefficients reduce to [45, 46]:

$$\alpha = \frac{3a_\kappa(1/\rho^{1/2}) - 2b_\kappa(\rho^{1/2}/z_i)}{2a_\kappa^{3/2}} \tag{3.20}$$

$$\gamma = \frac{\vartheta}{2} \tag{3.21}$$

$$\beta = \frac{\rho^{1/2}}{2a_\kappa^{3/2}} \tag{3.22}$$

where

$$a_\kappa = \frac{2\kappa - 1}{2\kappa - 3} \qquad b_\kappa = \frac{4\kappa^2 - 1}{2(2\kappa - 3)^2} \tag{3.23}$$

$$\rho = \frac{z_i^2 n_{0i}}{n_{0e}} \qquad \vartheta = \frac{\omega_{Bi}}{\omega pi} << 1 \tag{3.24}$$

Here, n_{0i} and n_{0e} are the unperturbed ion and electron densities, z_i is the ion charge state, ϑ is the ion-neutral collision frequency, ω_{Bi} is the ion cyclotron frequency, and ω_{pi} is the ion plasma frequency. Assuming a Maxwellian plasma ($\kappa \to \infty$) for the plasma regions in Table 3.1 and Table 3.2, the coefficients using Eqn 3.20 - Eqn 3.24 are again calculated as $\alpha = 1$, $\beta = 1/2$, and $\gamma = 0$, agreeing with our derivation of Eqn 3.16. It is important to note that these coefficients are simplified since we have assumed a collisionless Maxwellian plasma, with negligible dust density and the magnetic field effects. However, the velocity distribution functions of space plasmas typically have a suprathermal tail and are modeled with kappa distribution functions instead of a Maxwellian model [49, 50]. Considering the estimated kappa value from recent Earth magnetospheric models ($\kappa = 100$) [51, 52], the coefficients become:

$$\alpha = 1.0051 \qquad \beta = 0.4925 \qquad \gamma = 0 \tag{3.25}$$

We will use the $\kappa-$distribution coefficients in 3.25 for the remainder of this investigation.

One must consider the dispersion relation to see if kinetic collisions or magnetic field effects will have an influence on the coefficients or the velocity of the normalized forcing function [45, 46]. Since $\omega_{Bi} << \omega_{pi}$, the effect of the magnetic field is negligible [53] and 1D wave solutions are sufficient. In some polar regions, the plasma density is low, so the ion plasma frequency decreases and becomes comparable to the ion cyclotron frequency. In that case, the angle between the velocity and the magnetic field lines also needs to be considered.

Knowing that magnetic field effects are negligible, we need to assess whether ion-neutral collisions will affect soliton production. In general, $\gamma > 0$ in regions where the neutral density is at least three orders of magnitude greater than the electron density [53]. The boundary between the O+ dominant plasma and the H+ dominant plasma defines the transition between the ionosphere and plasmasphere, with the plasmasphere being fully ionized [54], and $\gamma = 0$. Since the dissipation coefficient $\gamma = 0$, we can assume that solitons will propagate in this region without collisional damping in a uniform environment.

Typical damping processes introduced into the damped KdV equation include (a) magnetosonic waves damped by electron-ion collisions, (b) ion sound waves damped by ion-neutral collisions, (c) ion sound waves with Landau damping, and (d)

shallow water waves damped by viscosity [48]. The cases that apply to ion acoustic solitons are ion-neutral collisions and Landau damping. It can be shown analytically that in the presence of damping, soliton amplitude decays as $A(t) = A_0 e^{-2\gamma t/3}$, soliton speed decays as $V(t) = V_0 e^{-2\gamma t/3}$, and soliton width grows as $W(t) = W_0 e^{\gamma t/3}$ [2, 46]. However, these estimates are based on unforced solitons, and it is expected that solitons will propagate farther than these estimates in the presence of a persistent force. We have addressed the ion-neutral collisions here, and will investigate Landau damping in Chapter 4.

3.2.2 Derived Force

Orbital debris will become charged due to the electrons and ions in the plasma environment, and will create a perturbation in the electric potential and density of the surrounding plasma. We will approximate the forcing term of the fKdV equation as a function of the debris surface potential and size.

For a spherical debris object immersed in a plasma, the charge Q of the sphere is related to the capacitance C and surface potential Φ_s by:

$$Q = C\Phi_s \tag{3.26}$$

For a spherical particle with radius $a < \lambda_D$, the capacitance is estimated in the orbit motion limited (OML) regime as [8]:

$$C = 4\pi\epsilon_o a \tag{3.27}$$

We refer to Bibhas [55] for a general expression of the surface potential of the debris. The radius, s, of the plasma sheath around a sphere is defined as:

$$s = a + \lambda_D \tag{3.28}$$

The surface potential of the debris (Φ_s) is calculated as [55]:

$$\exp\left[\frac{e\Phi_s}{k_B T}\right] = \left(\frac{m_e}{m_i}\right)^{1/2}\left(\frac{s}{a}\right)^2\left[1 - \frac{s^2 - a^2}{s^2}\exp\left[\frac{a^2}{s^2 - a^2}\frac{e\Phi_s}{k_B T}\right]\right] \tag{3.29}$$

In the thin sheath domain ($a > \lambda_D$), for a negative Φ_s, Eqn 3.29 simplifies to:

$$\exp\left[\frac{e\Phi_s}{k_B T}\right] = \left(\frac{m_e}{m_i}\right)^{1/2} \tag{3.30}$$

In the thick sheath domain ($a < \lambda_D$), Eqn 3.29 simplifies to:

$$\exp\left[\frac{e\Phi_s}{k_B T}\right] = \left(\frac{m_e}{m_i}\right)^{1/2}\left[1 - \frac{e\Phi_s}{k_B T}\right] \tag{3.31}$$

Next, we calculate the plasma potential Φ_p due to the surface potential of the debris (Φ_s) using Eqn 3.32, at one Debye length away from the surface of the spherical debris [56], $r = \lambda_D$. In our normalized coordinate system, plasma potential is divided by the electron temperature, as shown in Eqn 3.33:

$$\Phi_p = \Phi_s \exp\left[\frac{-r}{\lambda_D}\right] \tag{3.32}$$

$$\Phi_{p,n} = \Phi_s \exp\left[\frac{-r}{\lambda_D}\right]\left(\frac{e}{k_B T_e}\right) \tag{3.33}$$

Fig 3.1 shows the resulting calculations of the normalized plasma potential, $\Phi_{p,n}$, using Eqn 3.29 and Eqn 3.33.

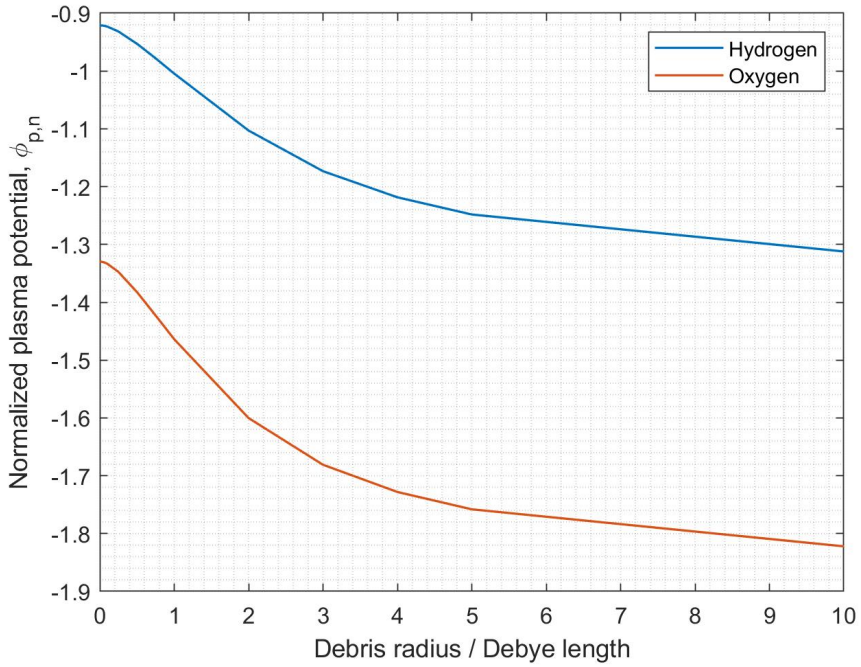

Figure 3.1: Normalized plasma potential, $\Phi_{p,n}$, calculated from Eqn 3.33, for two different dominant plasma species (oxygen and hydrogen).

Finally, the forcing term is estimated as a Gaussian shape with $\Phi_{p,n}$, the amplitude, and G, the full width at half maximum [57]:

$$f(\xi,\tau) = \Phi_{p,n} \exp\left[-\left(\frac{\xi - V_d\tau}{G}\right)^2\right] \tag{3.34}$$

where the G is radius of the orbital debris is normalized by λ_D:

$$G = \frac{a}{\lambda_D} \tag{3.35}$$

3.3 Numerical Methods

A pseudospectral scheme developed by Chan & Kerkhoven (CK) [27] was used to simulate the solitons, using Fourier transforms of the fKdV terms. While there are many examples of the pseudospectral method applied to the unforced KdV equation, there are few that describe its application to the forced KdV equation. We apply the Fourier transform to the forcing function as prescribed by Shen [44]. The scheme was written in Matlab and applied to known analytic solutions to the fKdV, given by [1, 2, 58].

The spatial domain $[-L, L]$ is discretized into N equidistant points and is normalized to $[0, 2\pi]$. Now, $\Delta\xi = \frac{2\pi}{N}$ and $\xi = s(x + L)$, where $s = \frac{\pi}{L}$ so that the solution is periodic from 0-2π. The resulting normalized fKdV equation is:

$$\frac{\partial U}{\partial \tau} + \alpha s U \frac{\partial U}{\partial \xi} + \beta s^3 \frac{\partial^3 U}{\partial \xi^3} = \frac{1}{2} s \frac{\partial f}{\partial \xi} \tag{3.36}$$

The time derivative is expressed as a finite difference approximation:

$$\frac{\partial U_j}{\partial \tau} \approx \frac{1}{2\Delta\tau}(U_j^{n+1} - U_j^{n-1}) \tag{3.37}$$

where the subscripts are the spatial domain and the superscripts are in the temporal domain. Thus, $j = \Delta\xi$, $n + 1 = \tau + \Delta\tau$, and $n - 1 = \tau - \Delta\tau$.

The discrete Fourier transform is:

$$\hat{U} = \mathscr{F}(U) = \frac{1}{\sqrt{N}} \sum_{j=0}^{N-1} U_j e^{(-2\pi jk/N)i} \qquad k = -\frac{N}{2}, -\frac{N}{2}+1, ..., \frac{N}{2}-1 \tag{3.38}$$

where $\mathscr{F}$ is the Fourier transform, and $\mathscr{F}^{-1}$ is the inverse Fourier transform.

An important property of the Fourier transform is that it represents differentiation as multiplication by ik, since the partial derivative commutes. Thus, we can rewrite the Fourier transform of the partial derivative of a wave, U, as:

$$\mathscr{F}\Big(\frac{\partial U}{\partial \xi}\Big) = \int_{-\infty}^{\infty} \Big(\frac{\partial U}{\partial \xi}\Big) e^{-ik\xi}\, \mathrm{d}\xi = -\int_{-\infty}^{\infty} U\Big(\frac{\partial e^{-ik\xi}}{\partial \xi}\Big)\, \mathrm{d}\xi = ik \int_{-\infty}^{\infty} U e^{-ik\xi}\, \mathrm{d}\xi \tag{3.39}$$

The Chan-Kerkhoven scheme uses a leapfrog finite difference method in the spectral space, thereby reducing the number of Fourier transforms required for each time step. Thus, Chan-Kerkhoven is recognized as the fastest method to date for solving the KdV equations [28]. The approximation for the dispersion term is:

$$\frac{\partial^3 U}{\partial \xi^3} \approx \frac{1}{2} \frac{\partial^3 (U_j^{n+1} + U_j^{n-1})}{\partial \xi^3} \tag{3.40}$$

$$\mathscr{F}^{-1}(\mathscr{F} \frac{\partial^3 U}{\partial \xi^3}) \approx \mathscr{F}^{-1}((ik)^3 \frac{1}{2} \mathscr{F}(U_j^{n+1} + U_j^{n-1})) \tag{3.41}$$

The nonlinear term becomes:

$$\mathscr{F}^{-1}(\mathscr{F}\frac{\partial U^2}{\partial \xi}) \approx \mathscr{F}^{-1}(iks\mathscr{F}(U_j^n)^2) \tag{3.42}$$

Applying Eqn 3.41 and Eqn 3.42 to Eqn 3.36 results in the following:

$$\frac{1}{2\Delta t}(U^{n+1} - U^{n-1}) + \alpha\mathscr{F}^{-1}(iks\mathscr{F}(U^n)^2) + \beta s^3\mathscr{F}^{-1}(i^3k^3\frac{1}{2}\mathscr{F}(U^{n+1} + U^{n-1})) = \frac{1}{2}s\mathscr{F}^{-1}(ik\mathscr{F}(f)) \tag{3.43}$$

After rearranging terms, the solution for U is:

$$U^{n+1} = \mathscr{F}^{-1}\Big[\frac{1}{1 - \Delta t\beta is^3k^3}((1 + \Delta t\beta is^3k^3)\mathscr{F}(U^{n-1}) - \Delta t\alpha isk\mathscr{F}(U^n)^2 + \Delta tisk\mathscr{F}(f))\Big] \tag{3.44}$$

To implement the Chan-Kerkhoven method, we first define the input parameters α, β, N, L, V_d, $\Phi_{p,n}$, G, $\Delta\tau$, τ_0, and τ_{final}. Next, we define the mesh space, ξ, and the wave numbers, k. For narrow forcing functions, it is important that the shape of the Gaussian is well resolved with the given mesh size so that the force will propagate appropriately as it translates in space. Increasing N to accommodate a narrow forcing function and large τ_{final} may result in exponentially larger computation times. One may consider defining a smaller L and non-periodic boundary so

that the wave solution does not wrap from the right to left spatial boundaries. It has been theorized that the precursor solitons comes solely from the depression zone between the upstream and downstream regions [2]. Thus, when simulating precursor solitons and defining non-periodic boundaries, it is important to ensure that L is large enough such that the depression zone between the upstream and downstream regions, as well as the upstream solitons, are well defined, as illustrated in Fig 3.2.

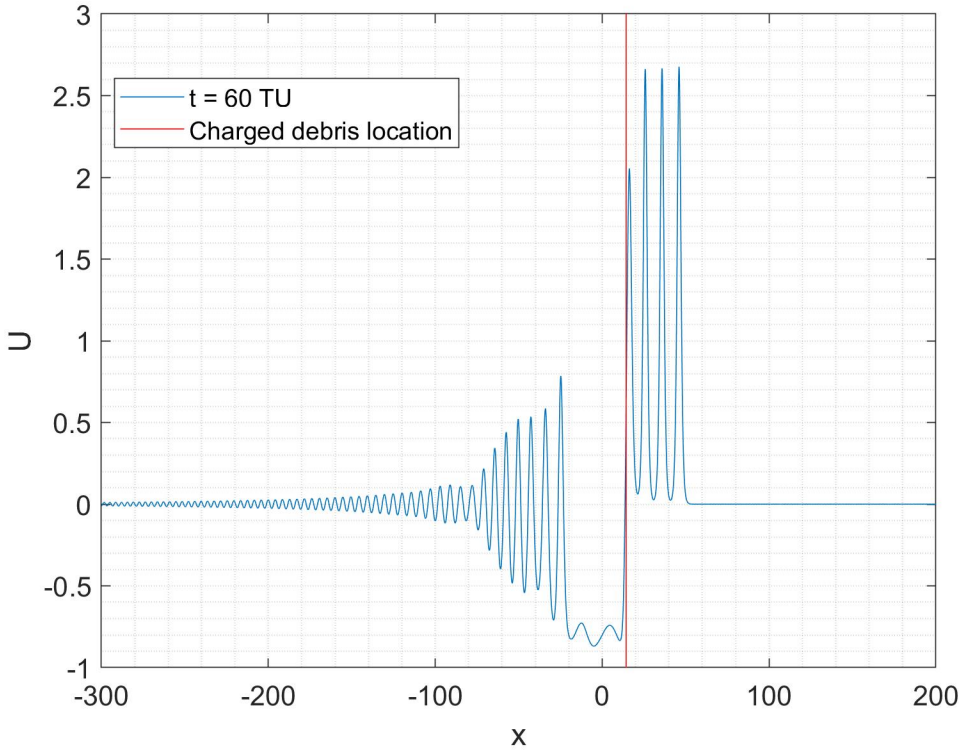

Figure 3.2: Example of depression zone ($-20 < x < 10$) between downstream wake ($x < -20$) and upstream precursor solitons ($x > 10$).

The solution for U is then marched forward in time using Eqn 3.44. For large propagation times, it is recommended to store every 100th or 1000th solution for U and the time vector in a matrix. Since the CK pseudospectral method requires

information from the previous time step, we are required to define the initial wave, U_0 at τ_0. To simulate from a rest state, initialize $U = 0$ and then march forward in time with Eqn 3.44, using a small time step $\Delta\tau/10$ to grow the wave for ten steps to remove any numerical instabilities for the initial approximation of U_0 [44]. The total time at this point is now $\Delta\tau$. Once U_0 is obtained, the code marches forward in time using Eqn 3.44 and $\Delta\tau$ to τ_{final}. To simulate analytically derived pinned solitons, it is important to initialize U with the soliton solution at $t = 0$ and $t = -\Delta\tau$. As shown in 3.4, a pinned soliton will not propagate in the numerical simulation unless its analytic solution is defined at U_0.

3.4 Numerical Validation

This section describes the validation of the numerical simulation described in 3.3. Several analytical solutions for the forced and unforced KdV equations were chosen with a variety of input parameters. Differences between the numerical and analytical solutions were calculated in order to assess accuracy of the code.

The code was first tested on an unforced analytic solution from [1], with the input parameters in Table 3.3 and initial condition $U_0 = 12\text{sech}^2(x)$. This solution falls within the family of exact N-soliton solutions of the form in Eqn 3.45 [59], with $N = 3$. The 3-soliton solution was produced as expected, and shown in Fig 3.3.

$$U(x, 0) = N(N + 1)\text{sech}^2(x) \tag{3.45}$$

Once the code was validated against an unforced KdV analytic solution, we

Table 3.3: Input parameters for 3-soliton analytic solution from [1].

α	β	N	L	dt
6	1	1024	50	0.001

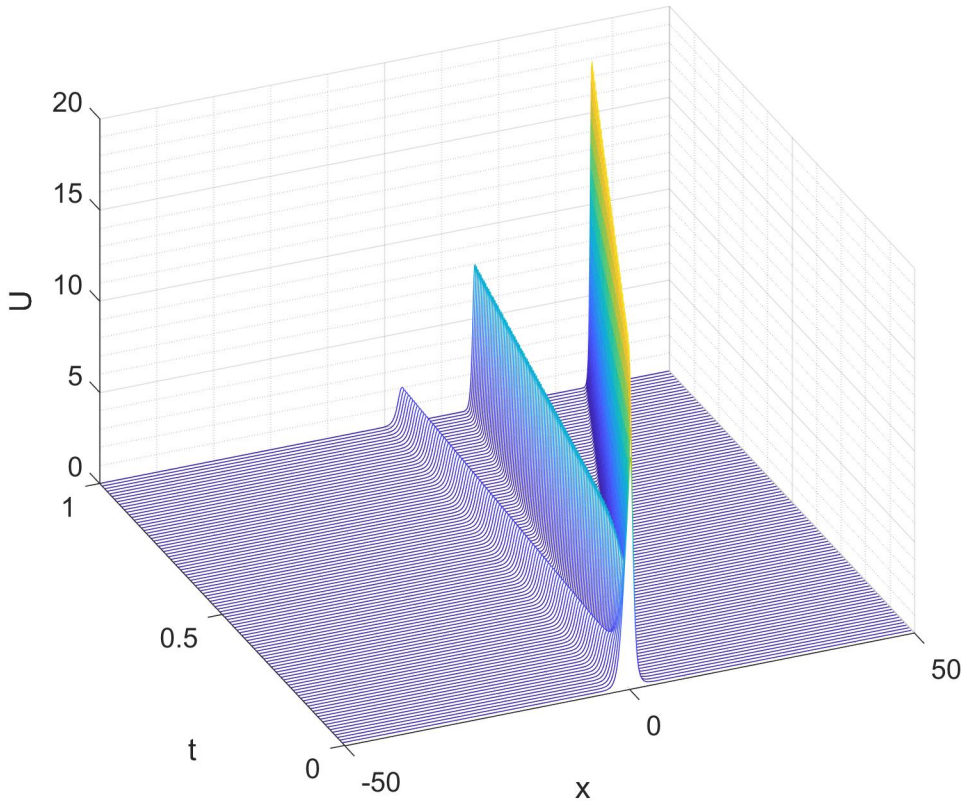

Figure 3.3: Reproduction of unforced 3-soliton solution from [1]. The initial condition is $12\text{sech}^2(x)$, with $\alpha = 6$ and $\beta = 1$.

proceeded with several forced KdV analytic solutions of various coefficients, propagation times, and forcing terms that are either static or change with space and time.

Two analytic forced KdV solutions were tested from [58]. The forcing term for both examples is given as Eqn 3.46, and the solution is given as Eqn 3.47.

$$f(x,t) = \frac{12k\beta}{\alpha}\left(k^3(4\beta - \delta) - \frac{\partial a(t)}{\partial t}\right) \tag{3.46}$$

Table 3.4: Input parameters for the analytic solution described Eqn 3.48 and Eqn 3.49 plotted in Fig 3.4.

k	δ	α	β	b_1	b_0	b_2
1	4	-2	1/6	2	-1	-1

$$U(x,t) = 12\beta k^2 \text{sech}^2\big(k(x-\delta k^2 t) - a(t)\big) \tag{3.47}$$

For the example in Fig 3.4, $a(t)$ is defined as $a(t) = \exp\big(b_2 t^2 + b_1 t + b_0\big)$, where b_2, b_1, and b_0 are constants. This results in the traveling-wave forcing term in Eqn 3.48, with the resulting wave solution in Eqn 3.49. It is important to initialize the numerical simulation with the analytical solution of the wave in Eqn 3.49 at $t = 0$. The input parameters for Fig 3.4 are provided in Table 3.4. As expected, difference between the numerical and analytic solution is on the order of $\Delta t = 10^{-4}$s due to the discretized addition of the forcing function at each time step.

$$f(x,t) = \frac{12k\beta}{\alpha}\Big(k^3(4\beta-\delta) - (2b_2 t + b_1)\exp(b_2 t^2 + b_1 t + b_0)\Big)\text{sech}^2(k(x-\delta k^2 t) \\ -\exp(b_2 t^2 + b_1 t + b_0)) \tag{3.48}$$

$$U(x,t) = 12\beta k^2 \text{sech}^2\big(k(x-\delta k^2 t) - \exp\big(b_2 t^2 + b_1 t + b_0\big)\big) \tag{3.49}$$

For the example in Fig 3.5, $a(t)$ is defined as $a(t) = b_2 \arctan(At) + b_1 t + b_0$, where b_2,b_1,b_0, and A are constants. This results in the dromion forcing term in Eqn 3.50, with the resulting wave solution in Eqn 3.51. It is important to initialize the

Table 3.5: Input parameters for the analytic solution described Eqn 3.50 and Eqn 3.51 plotted in Fig 3.5.

k	A	δ	α	β	b_1	b_0	b
1	3	4	2	1/4	-3	0	-1

numerical simulation with the analytical solution of the wave in Eqn 3.51 at $t = 0$. The input parameters for Fig 3.5 are provided in Table 3.5. As expected, difference between the numerical and analytic solution is on the order of $\Delta t = 10^{-4}$s due to the discretized addition of the forcing function at each time step.

$$f(x,t) = \frac{12k\beta}{\alpha}\Big(k^3(4\beta-\delta) - \frac{bA}{1+A^2t^2} - b_1\Big)\text{sech}^2(k(x-\delta k^2 t) - (b\arctan(At) + b_1 t + b_0)) \tag{3.50}$$

$$U(x,t) = 12\beta k^2 \text{sech}^2\big(k(x-4k^2t) - (b\arctan(At) + b_1 t + b_0)\big) \tag{3.51}$$

A pinned soliton solution was modeled from Wu [2], and the results are shown in Fig 3.6. The force is $f(x) = 2b_1\text{sech}(Kx)^2$, where $b_1 = -0.1250$ and $K = 0.6124$. The pinned soliton is initialized at U_0 with its solution of $U(x) = a\text{sech}(Kx)^2$, where $a = 0.5$. The difference between the numerical and analytical solutions are shown on the right hand side of Fig 3.6. The solution is highly stable, with the difference between the numerical and analytical solutions on the order of 10^{-9} for a soliton with amplitude = 0.5.

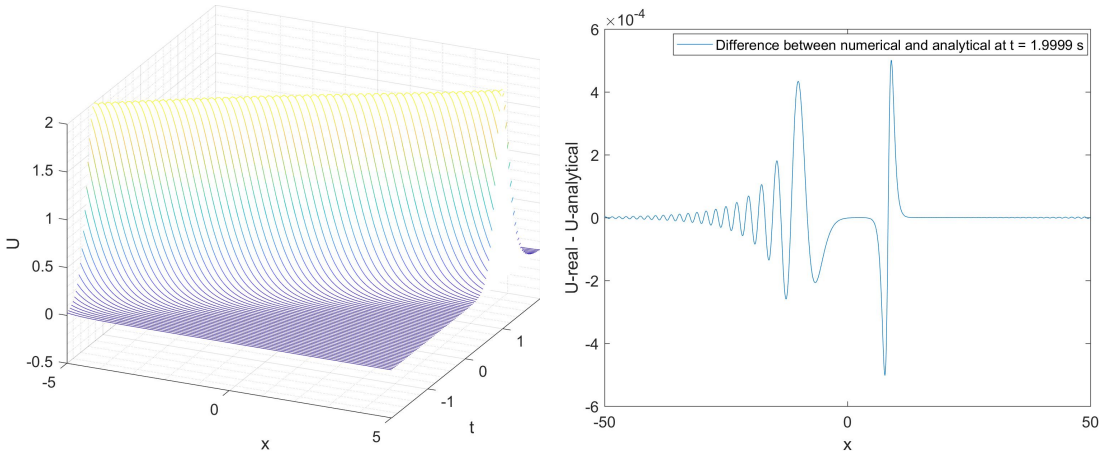

(a) Numerical simulation (b) Numerical accuracy

Figure 3.4: (a) Reproduction of an analytic solution for a moving hyperbolic secant force defined as Eqn 3.48 and wave solution defined as Eqn 3.49 [58]. (b) Accuracy of the numerical solution.

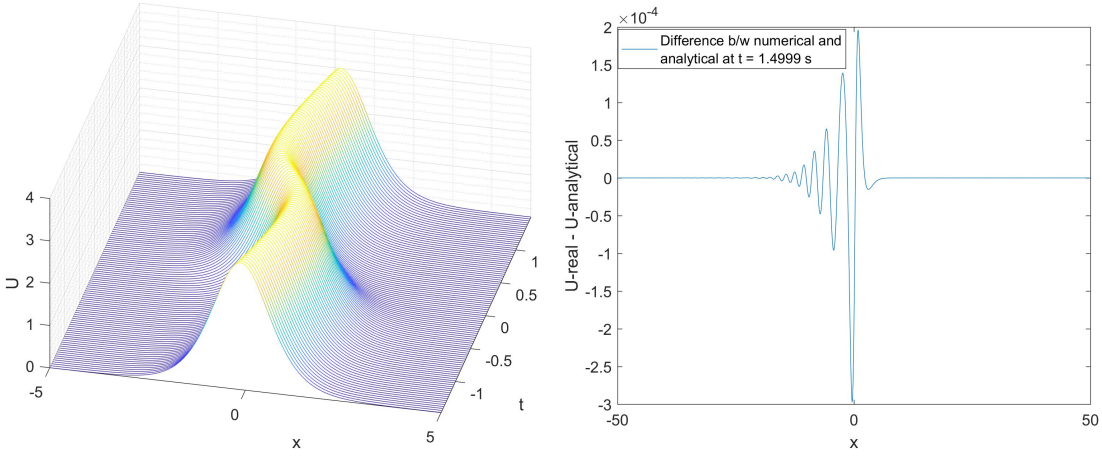

(a) Numerical simulation (b) Numerical accuracy

Figure 3.5: (a) Reproduction of an analytic solution for a moving hyperbolic secant force defined as Eqn 3.50 and solution defined as Eqn 3.51 [58]. (b) Accuracy of the numerical solution.

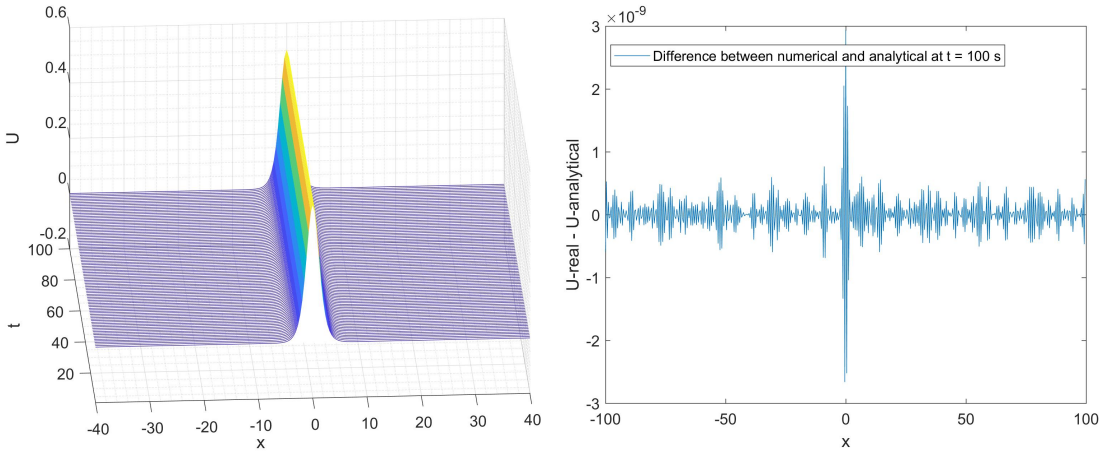

Figure 3.6: Reproduction of Wu [2] pinned soliton solution. The force is $f(x) = 2b_1\text{sech}(Kx)^2$, where $b_1 = -0.1250$ and $K = 0.6124$. Right: Accuracy of the numerical solution.

3.5 Orbital Debris Simulation Results

Having validated our simulations of the fKdV equation, we now simulate solitons using ionospheric plasma and orbital debris characteristics. Using the CK method in Eqn 3.44 and the forcing function in Eqn 3.34, we simulated the response of the plasma to a charged debris object for the plasma regions in Table 3.1 and debris radii ranging from $0.1 - 10$ cm, for a maximum propagation time of 1800 TU. The coefficients used are provided in 3.25. The circular orbit velocity from Table 3.1 was used for the debris velocity. Note that as G, the dimensionless debris size, decreases, L and N are adjusted to ensure that the force is sufficiently resolved as it is propagated with time, and that the wave does not reflect across periodic boundaries in the pseudospectral scheme. The domain in these simulations is normalized as in Eqn 3.4. For all figures in this section, the x domain is in units of the Debye length, and time is units of Debye length divided by the ion acoustic velocity (one time unit (TU) is λ_D/V_{ia}). The solitons propagate along the debris velocity vector.

3.5.1 Low LEO

Low energy, high density plasma is found in the mid-latitude regions of LEO. The dominant ion species is O+. The debris orbital velocity is much faster than the ion acoustic velocity. In this regime, pinned solitons were produced, traveling at the same speed as the orbital debris, as shown in Fig 3.7. For the Low LEO region specified in Table 3.1 and a circular orbit velocity of 7.51 km/s, pinned solitons were observed for the full range of debris sizes (0.1 - 10cm) examined. For 1mm

and 1cm radius debris, the pinned soliton amplitude was approximately 1.04 and 1.14 times the unperturbed background density, respectively. Since pinned solitons travel with the debris, they are not useful for on-orbit detection efforts since they would not be sensed prior to collision. However, pinned solitons can be detected from ground sensors using the same techniques used to measure plasma density irregularities. Small scale plasma irregularities are frequently studied with existing sensor technology, including ground based radar [60], ionosondes [61], and space-based sensors [62, 63]. The amplitude of the density waves that can be detected is less than 0.1% of the unperturbed density [63]. Therefore, the amplitude of the pinned solitons is within the range of detectability of current sensors.

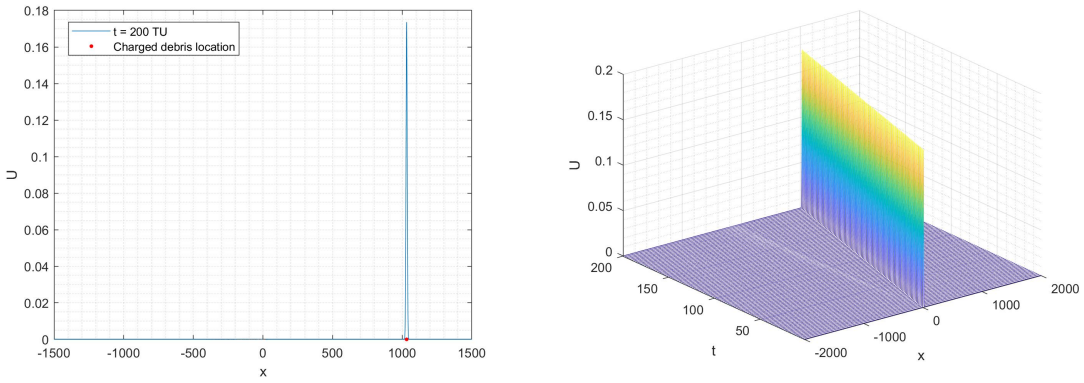

(a) Instantaneous Debris and Soliton Signature

(b) Soliton Propagation with Time

Figure 3.7: Pinned soliton created by 5 cm radius charged debris in Low LEO region of Table 3.1, with a circular orbit velocity.

3.5.2 High LEO Region 1

As the altitude increases, the plasma density decreases. In this topside ionosphere environment, the dominant ion species is H+, which is much lighter than O+. The ion acoustic velocity is comparable to the debris orbital velocity, and the Debye length is comparable to the debris size. As opposed to pinned solitons which travel with the debris, precursor solitons are produced, which advance ahead of the debris, as shown in Fig 3.8 and Fig 3.10. Since the precursor solitons will advance ahead of the debris, they will allow for the potential to detect the debris without collision.

In our normalized system, the soliton amplitude displayed in Fig 3.7 - Fig 3.11 is the perturbed ion density normalized by the unperturbed ion density, $U = (n - n_0)/n_0$. For example, Fig 3.11 has a soliton amplitude of 2, corresponding to 3x the unperturbed ion density in High LEO 2. In High LEO 2, the unperturbed ion density is 10^4 cm^{-3}, so the perturbed ion density will be 3x10^4 cm^{-3}.

Fig 3.8 and Fig 3.10 show the solitons generated by 2.5 mm and 0.5 cm radius debris using the κ-distribution coefficients in 3.25, $\alpha = 1.0051$, $\beta = 0.4925$, $\gamma = 0$, while Fig 3.9 shows a comparison to the Maxwellian distribution coefficients, $\alpha = 1$, $\beta = 0.5$, $\gamma = 0$. Using the κ distribution results in more wave steepening and less wave dissipation, allowing for more precursor solitons to be produced in the 1400TU simulation time shown. A discussion of how the soliton characteristics change as a result of the debris characteristics is given in 3.7.

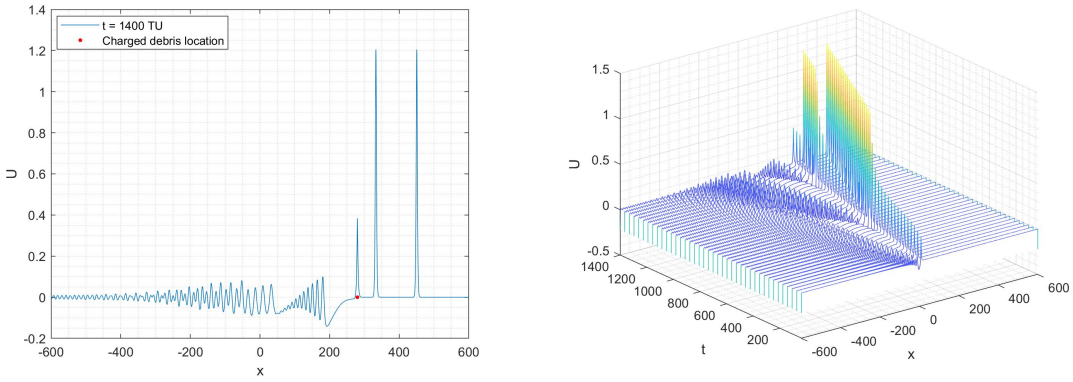

(a) Instantaneous Plasma Response

(b) Time Varying Plasma Response

Figure 3.8: Precursor solitons created by 2.5 mm radius charged debris in High LEO Region 1 of Table 3.1, in an elliptical orbit with $V = 1.2V_{ia}$, $\Phi_{p,n} = -0.93$, and κ coefficients.

3.5.3 High LEO Region 2

In this region, the lower limit to the topside ionosphere plasma density is used. Precursor solitons are produced, advancing ahead of the debris, as shown in Fig 3.11. While the ion acoustic velocity is still comparable to the debris orbital velocity, the Debye length is increasingly larger than the debris size. When compared to High LEO Region 1, smaller debris do not produce precursor solitons in this region, and the limits for debris size and velocity that produce precursor solitons are discussed in 3.6.

3.5.4 Polar LEO

In Polar LEO 1, the plasma is high energy and low density. As a result, the ion acoustic velocity exceeds the debris orbital velocity, and the Debye length is much

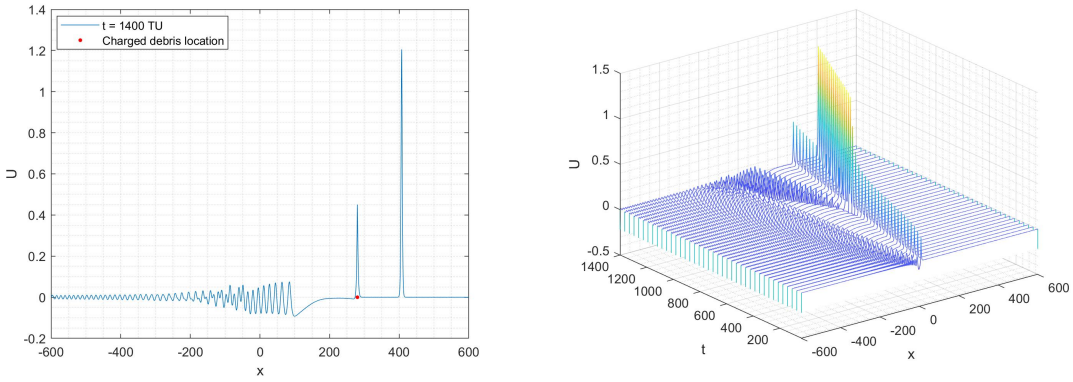

(a) Instantaneous Plasma Response

(b) Time Varying Plasma Response

Figure 3.9: Precursor solitons created by 2.5 mm radius charged debris in High LEO Region 1 of Table 3.1, in an elliptical orbit with $V = 1.2V_{ia}$, $\Phi_{p,n} = -0.93$, and Maxwellian coefficients.

larger than the debris size. The forcing function in Eqn 3.34 approaches a Dirac function moving downstream with respect to the plasma. It is possible to generate ion acoustic waves with a Dirac function with a speed comparable to the ion acoustic speed. However, the debris speed in this case is much slower than the ion acoustic speed. Over the full range of sizes considered and the circular orbit velocity of 7.56 km/s for Polar LEO 1 in Table 3.2, low amplitude wake perturbations are present, but no coherent waves were produced. Similar to Low LEO, pinned solitons are produced in Polar LEO 2, since the orbital debris velocity is much greater than the ion acoustic velocity. Precursor solitons are generated in Polar LEO 3, since the orbital debris velocity is comparable to the ion acoustic velocity. However, the range of velocities that can produce precursor solitons is reduced since the Debye length is greater in Polar LEO 3 when compared to High LEO 1 and High LEO 2. These limits are further discussed in 3.6. The limits for debris size and velocity that

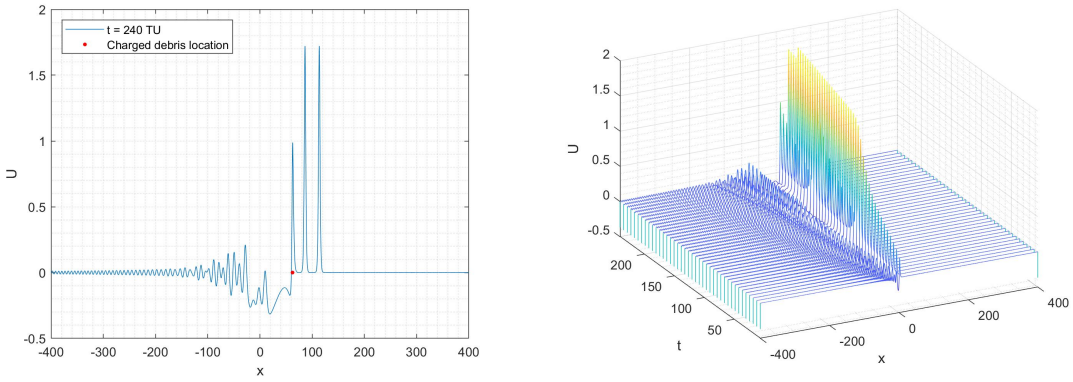

(a) Instantaneous Plasma Response

(b) Time Varying Plasma Response

Figure 3.10: Precursor solitons created by 0.5 cm radius charged debris in High LEO Region 1 of Table 3.1. The debris has a circular orbit velocity, with $\Phi_{p,n} = -0.94$, and κ coefficients.

produce precursor solitons in Polar LEO 2 and Polar LEO 3 are discussed in 3.7.

3.5.5 GEO

Like the Polar LEO 1, the plasma environment at GEO consists of high energy, low density electrons. The ion acoustic velocity is much larger than the debris orbital velocity, and the Debye length is much larger than the debris size for mm-cm sized debris. Similar to results in the Polar LEO 1, no waves were produced.

3.6 Velocity Threshold for Precursor Soliton Generation

The ability for orbital debris to produce pinned or precursor solitons depends on the relative velocity between the debris and the plasma medium. The transcritical regime, where precursor solitons are produced that advance ahead of the debris, resides between the subcritical and supercritical velocity limits. In the transcritical

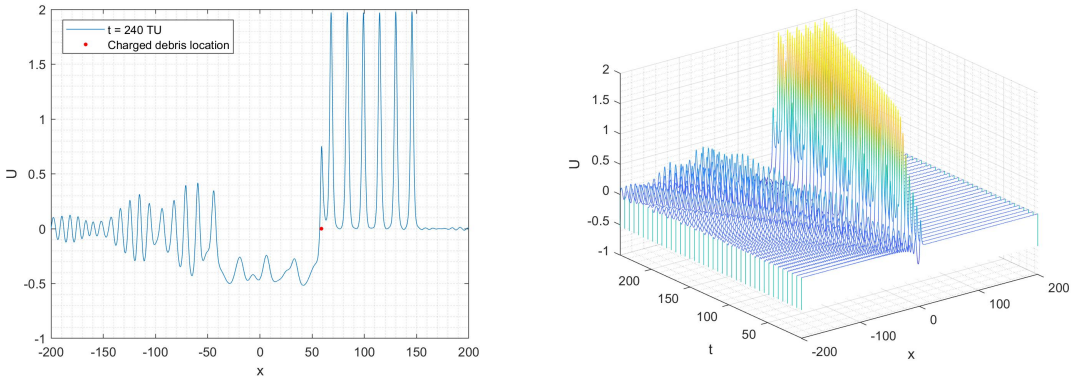

(a) Instantaneous Plasma Response

(b) Time Varying Plasma Response

Figure 3.11: Precursor solitons created by 2.5 cm radius charged debris in High LEO Region 2 of Table 3.1. The debris is in a circular orbit, $\Phi_{p,n} = -0.96$, and κ coefficients.

regime, the velocity of the debris that can produce precursor solitions is usually referenced in literature as $1 - 1.5$x the velocity of the medium [9, 57]. This estimate can be refined by deriving the velocity limits at the subcritical and supercritical boundaries. The velocity thresholds required for soliton production can be derived from Eqn 3.17, by solving for μ, the velocity of the plasma medium moving over a static disturbance. The derivation also applies to a static plasma medium and a moving disturbance, or in general, the relative velocity between the plasma and the disturbance [44].

Since we are looking for solitary wave solutions of Eqn 3.17, the wave must satisfy boundary conditions $U(x = \pm\infty) = U'(x = \pm\infty) = 0$. By direct integration of Eqn 3.17, all solutions to the ordinary differential equation boundary value problem can be written as [44]:

$$U(x) = \begin{cases} -\frac{3\mu}{2\alpha}\text{sech}^2\sqrt{\frac{-\mu}{4\beta}}(x - L_+) & x > 0 \\ -\frac{3\mu}{2\alpha}\text{sech}^2\sqrt{\frac{-\mu}{4\beta}}(x - L_-) & x < 0 \end{cases} \tag{3.52}$$

where L_+ and L_- are constants [44]. The forcing term requires a jump discontinuity for $U'(x)$ at $x = 0$:

$$U'(0_+) - U'(0_-) = \frac{A}{2\beta} \tag{3.53}$$

where the area of the Gaussian forcing disturbance is:

$$A = |\Phi_{p,n}|G\sqrt{\pi} \tag{3.54}$$

Recall that the spatial domain, x, and the debris width, G, are normalized by the Debye length according to Eqn 3.4 and Eqn 3.35. The normalized plasma potential,$\Phi_{p,n}$, is nondimensionalized by the electron temperature, according to Eqn 3.33.

Rewriting Eqn 3.53 using Eqn 3.52 demonstrates that the given conditions hold for a nonzero force only if $L_+ \neq L_-$, requiring that $L_+ = -L_-$ [44]. The resulting expression leads to a relationship between the area of the forcing disturbance, steepening coefficient, and dissipation coefficient [44, 64] for the supercritical limit:

$$V_{sup} = 1 + \left(\frac{3(\alpha/2)^2 A^2}{16\beta}\right)^{1/3} \tag{3.55}$$

At the subcritical limit, the boundary conditions become $U(x = -\infty) =$

$U'(x = -\infty) = 0$, and $U(x) \equiv 0$ when $x \leq 0$ [44]. Thus, the relationship for the velocity at the subcritical limit becomes:

$$V_{sub} = 1 - \left(\frac{3(\alpha/2)^2 A^2}{4\beta} \right)^{1/3} \tag{3.56}$$

Thus, for a 0.5 cm radius debris in High LEO Region 1 and Debye length of 1.38 cm, the supercritical velocity limit is $V_{sup} = 1.33V_{ia}$. Note that the velocity threshold is proportional to the area of the forcing function. Smaller debris will have a smaller transcritical velocity range, and larger debris will have a larger transcritical velocity range. For debris with 0.25 cm radius in High LEO Region 1, $V_{sup} = 1.20V_{ia}$ and $V_{sub} = 0.68V_{ia}$. The supercritical and subcritical velocities for the regions in Table 3.1 and Table 3.2 are listed in Table 3.6 and Table 3.7. For GEO and Polar LEO 1, the dominant ion could be oxygen or hydrogen depending on solar activity, so V_{ia} is included for both species.

In Table 3.6 and Table 3.7, the transcritical velocity limits are listed in units of the ion acoustic velocity. For $V > V_{ia}$, the debris is traveling faster than the ion acoustic velocity, along the same direction. For $0 < V < V_{ia}$, the debris is traveling slower than the ion acoustic velocity, along the same direction. For $V < 0$, the debris is traveling in the opposite direction as the ion acoustic velocity. Examples of soliton generation with $V < 0$ are provided in Fig 3.12. In the left figure, solitons are generated by charged debris with 2.5 cm radius. The debris is traveling to the left along the x axis, $V_d = -0.25V_{ia}$ and $\Phi_{p,n} = -1.08$. In the right figure, solitons are propagating from charged debris with 5 cm radius. The debris is traveling to

Table 3.6: Normalized plasma potential, $\Phi_{p,n}$, and orbital velocity range required for 5 cm, 2.5 cm, 0.5 cm, 2.5 mm, and 0.5 mm radius debris to produce precursor solitons in the mid-latitude ionosphere.

	Low LEO	High LEO 1	High LEO 2	GEO
Altitude (km)	700	1,200	1,400	35,786
Latitude (deg)	0-55	0-55	0-55	0-90
λ_D (cm)	0.83	1.38	4.36	23,504.00
V_d (V_{ia})	6.16	1.26	1.24	0.04 / 0.01
5 cm radius debris				
$\Phi_{p,n}$	-1.77	-1.20	-1.02	-0.92
V_{sup} (V_{ia})	4.25	2.79	1.74	1.00
V_{sub} (V_{ia})	-4.16	-1.84	-0.18	1.00
2.5 cm radius debris				
$\Phi_{p,n}$	-1.68	-1.08	-0.96	-0.92
V_{sup} (V_{ia})	2.98	2.05	1.45	1.00
V_{sub} (V_{ia})	-2.14	-0.67	0.28	1.00
0.5 cm radius debris				
$\Phi_{p,n}$	-1.40	-0.94	-0.92	-0.92
V_{sup} (V_{ia})	1.60	1.33	1.15	1.00
V_{sub} (V_{ia})	0.05	0.48	0.76	1.00
2.5 mm radius debris				
$\Phi_{p,n}$	-1.35	-0.93	-0.92	-0.92
V_{sup} (V_{ia})	1.37	1.20	1.09	1.00
V_{sub} (V_{ia})	0.41	0.68	0.85	1.00
0.5 mm radius debris				
$\Phi_{p,n}$	-1.33	-0.92	-0.92	-0.92
V_{sup} (V_{ia})	1.12	1.07	1.03	1.00
V_{sub} (V_{ia})	0.80	0.89	0.95	1.00

Table 3.7: Normalized plasma potential, $\Phi_{p,n}$, and orbital velocity range required for 5 cm, 2.5 cm, 0.5 cm, 2.5 mm, and 0.5 mm radius debris to produce precursor solitons in the high-latitude ionosphere.

	Polar LEO 1	Polar LEO 2	Polar LEO 3
Altitude (km)	600	600	950
Latitude (deg)	55-90	55-90	55-90
λ_D (cm)	7,432.00	3.72	13.91
V_d (V_{ia})	0.1 / 0.02	6.20	1.28
5 cm radius debris			
$\Phi_{p,n}$	-0.92	-1.51	-0.94
V_{sup} (V_{ia})	1.00	2.08	1.33
V_{sub} (V_{ia})	0.99	-0.71	0.48
2.5 cm radius debris			
$\Phi_{p,n}$	-0.92	-1.41	-0.93
V_{sup} (V_{ia})	1.00	1.65	1.20
V_{sub} (V_{ia})	1.00	-0.03	0.68
0.5 cm radius debris			
$\Phi_{p,n}$	-0.92	-1.34	-0.92
V_{sup} (V_{ia})	1.00	1.21	1.07
V_{sub} (V_{ia})	1.00	0.66	0.86
2.5 mm radius debris			
$\Phi_{p,n}$	-0.92	-1.33	-0.92
V_{sup} (V_{ia})	1.00	1.13	1.04
V_{sub} (V_{ia})	1.00	0.79	0.93
0.5 mm radius debris			
$\Phi_{p,n}$	-0.92	-1.33	-0.92
V_{sup} (V_{ia})	1.00	1.05	1.01
V_{sub} (V_{ia})	1.00	0.93	0.98

the left along the x axis, $V_d = -0.25V_{ia}$ and $\Phi_{p,n} = -1.20$.

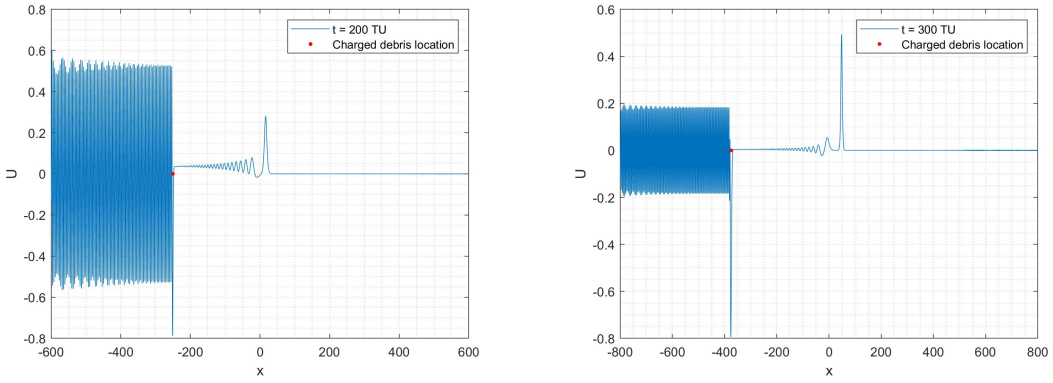

(a) 2.5 cm radius debris

(b) 5 cm radius debris

Figure 3.12: Solitons are generated from charged debris traveling in the opposite direction as the plasma, left along the x axis, in High LEO Region 1.

Orbital debris in High LEO with circular and elliptical orbits will fall within the transcritical velocity threshold for a range of sub-centimeter debris sizes. For example, the velocity of debris in circular orbit at 1,200 km altitude is $1.26V_{ia}$. For debris in an elliptical orbit with 1,200 km apogee and 200 km perigee, $V_d = 1.22V_{ia}$ at 1,200 km. Precursor solitons are expected for the subset of elliptical orbits that fall within the supercritical and subcritical velocity limits in Table 3.6, with a wider range of orbits falling within the velocity limits in the High LEO 1 region than other altitude regions for mm-cm size debris. The soliton generation will be limited by the amount of time the debris spends in the H+ dominated plasma.

Numerical simulations show that sub-centimeter orbital debris produces pinned solitons in mid-latitude Low LEO regions. For circular orbits, the debris velocity is much larger than the ion acoustic velocity in Low LEO. The debris velocity is

comparable to the ion acoustic velocity for circular orbits in the High LEO region, thus the creation of precursor solitons is possible in High LEO.

3.7 Precursor Soliton Characteristics

In order to evaluate the feasibility of detecting small orbital debris via soliton detection, it is necessary to understand the properties of the generated solitons as a function of debris size and speed. These properties include soliton height, width, velocity, and generation interval. Solitons retain their velocity and shape in an undamped system and the product of the amplitude with the square of its width remains constant. Additionally, the generation interval is predictable depending on the amplitude of the source [2, 44], potentially allowing for characterization of the force that created them.

Dimensionless simulations were conducted to model the orbital debris soliton amplitude, speed, width, and generation intervals in the Earth's plasmasphere. Simulations were conducted for 21 dimensionless debris sizes ranging from G = 3.623 - 0.072 and 16 orbital debris velocities, expressed in terms of the supercritical velocity of that debris size, ranging from $V = 0.48V_{sup}$ to $1V_{sup}$. Note that each debris size has its own supercritical velocity. Computational parameters for the simulations are as follows: N = 51,200, L = 800, dt = 0.001. The soliton properties were modeled with biharmonic interpolation, with the data interpolated linearly along the velocity vector at 0.01 increments. The 3D fit for soliton speed is shown in Fig 3.13. The accuracy of the 3D fit models was confirmed through comparison to solitons

generated with absolute velocities.

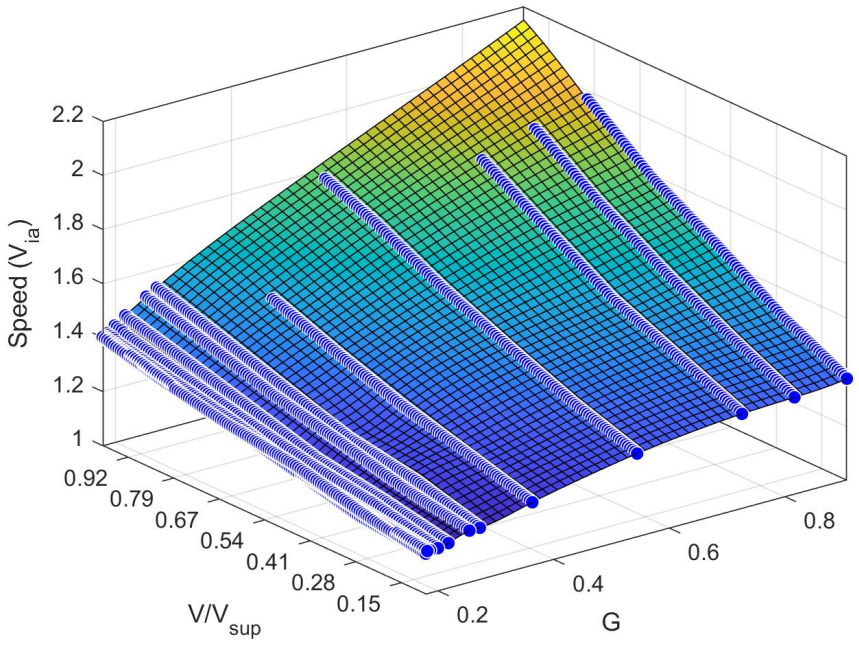

Figure 3.13: Precursor soliton speed as a function of debris size and velocity. Points represent data, and the surface represents a 3D fit.

Fig 3.14, Fig 3.15, and Fig 3.16 show the amplitude, width, speed, and time to generate precursor solitons as a function of dimensionless debris size and velocity relative to the debris' supercritical velocity. Table 3.8 shows dimensionalized example debris sizes using High LEO Region 1 and High LEO Region 2 plasma parameters from Table 3.1. As the plasma density increases, the Debye length decreases, allowing for a better resolved debris force and a wider transcritical range. As shown in Fig 3.14, as the debris size decreases, the time required to generate a precursor soliton becomes significantly longer and the transcritical velocity range is smaller. As shown in Fig 3.15 and Fig 3.16, as the debris size decreases, the soliton

speed and amplitude decrease, while the width increases. In Fig 3.14 - Fig 3.16, the lower limit of velocities that produce precursor solitons varies from case to case since the debris is traveling slower than the plasma and the solution can become numerically unstable. Time units (TU) are defined by the plasma frequency. As an example of time units, in High LEO Region 1, one TU $= \lambda_D/V_{ia} = 2.4\text{x}10^{-6}$ s.

As shown in Fig 3.14, the time between precursor solitons ranges from $10-1000$ TU, corresponding to a frequency of $0.4-4$ kHz, which is within the range of other electromagnetic wave phenomena in the Earth's plasmasphere caused by naturally occurring energy transfer between hot or streaming plasma or man-made activity. These wave phenomena include ion cyclotron whistlers, ELF hiss, LHR noise, electron whistlers, and UHR noise. Both ion cyclotron whistlers and electron whistlers travel along magnetic field lines, LHR/UHR noise occur near the plasmapause, and the ELF hiss is observed throughout the plasmasphere at all local times [65].

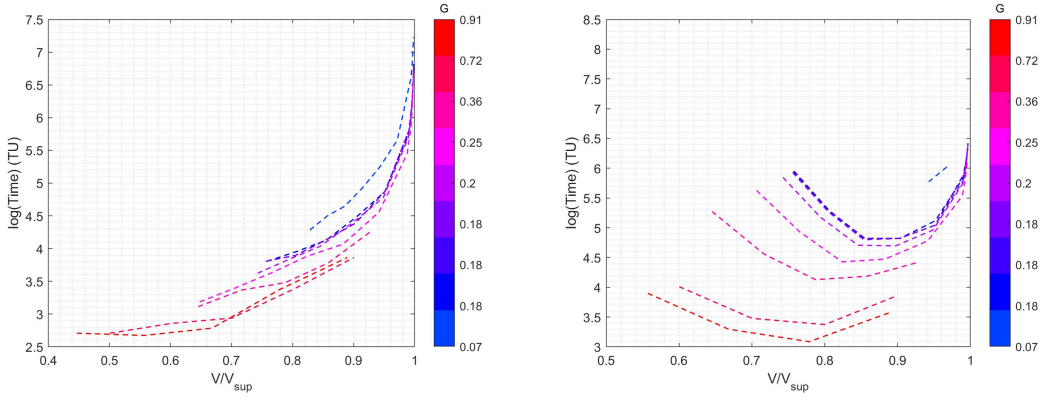

(a) First Soliton Generation Time

(b) Intersolitonic Interval

Figure 3.14: (a) Time required to produce the first precursor soliton as a function of debris size and velocity relative to the debris supercritical velocity. (b) Time between generation of subsequent precursor solitons.

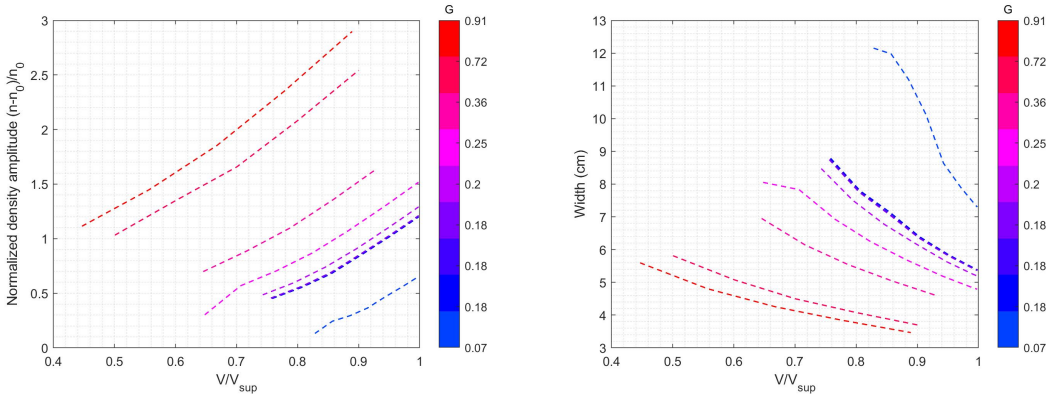

(a) Soliton Amplitude

(b) Soliton Width

Figure 3.15: (a) Precursor soliton amplitude as a function of debris size and velocity relative to the debris' supercritical velocity, where amplitude is the perturbation of the ion density normalized by the unperturbed ion density. (b) Precursor soliton width as a function of debris size and velocity.

Fig 3.17 shows that as the absolute velocity of the debris increases, the amplitude of the soliton increases. Fig 3.18 shows that as the absolute velocity of the debris increases, the speed of the soliton also increases. Note that this trend is only valid for velocities below the supercritical velocity. Additionally, as the debris size increases, the amplitude and speed of the soliton also increases. While Fig 3.14 - Fig 3.16 show the soliton properties as a function of debris size and velocity relative to the debris supercritical velocity, Fig 3.17 - Fig 3.21 show the soliton properties as a function debris size for one absolute velocity. For a debris radius of 5 cm in High LEO 1, G = 0.362. For a debris velocity of $1.1449V_{ia}$, the soliton width is 4.5 cm, and the soliton speed is $1.57V_{ia}$, and the normalized amplitude of the precursor soliton is 1.74, which equates to a wave density of 2.74x10^5 cm^{-3}, compared to the background density of 10^5 cm^{-3}.

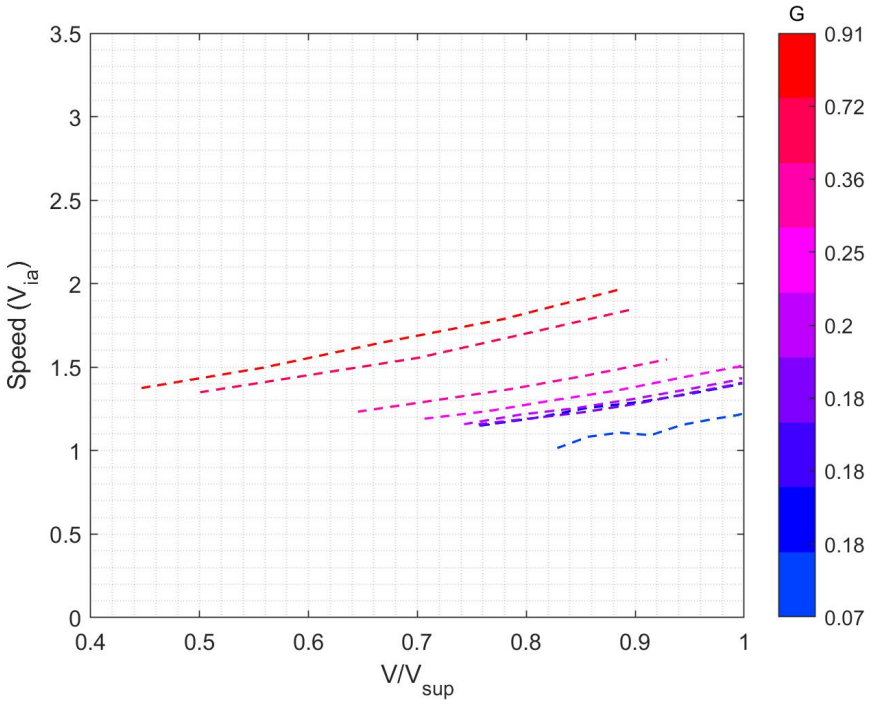

Figure 3.16: Precursor soliton speed as a function of debris size and velocity relative to the debris supercritical velocity.

An important distinction between Fig 3.16 and Fig 3.18 can be seen when comparing to the 3D plot in Fig 3.13. Fig 3.16 shows slices of Fig 3.13, taken at varying values of G. However, since Fig 3.18 has an absolute velocity axis, it is best represented as a slice of Fig 3.13 at an angle between the relative velocity and debris width, where the absolute velocity at each debris size is a different relative velocity with respect to the debris supercritical limit. Fig 3.18 is meaningful when evaluating the feasibility of precursor soliton generation from debris in actual orbits, since orbital velocity is independent of debris size.

For the regions in High LEO where precursor solitons can be generated, $V_{ia} =$ 5.75 km/s, $\lambda_D = 1 - 5$ cm, and one TU ranges from $10^{-5} - 10^{-6}$ s. Therefore, the

Table 3.8: Example debris sizes for Fig 3.14, Fig 3.15, and Fig 3.16 using the Debye length for High LEO Region 1 (1.38 cm) and High LEO Region 2 (4.36 cm) from Table 3.1.

G	Debris Size (cm) in High LEO 1	Debris Size (cm) in High LEO 2
0.072	0.100	0.314
0.178	0.246	0.776
0.180	0.249	0.785
0.181	0.250	0.789
0.199	0.275	0.868
0.254	0.350	1.107
0.362	0.500	1.578
0.725	1.000	3.161
0.906	1.250	3.950

generation of the first precursor soliton, as shown in Fig 3.20, occurs in a fraction of a second. One can expect that precursor solitons will be generated as soon as the debris enters the precursor generation region. Results in Fig 3.20 - Fig 3.21 are consistent with the prediction that the time to generate solitons will become exponentially longer as the debris velocity approaches the transcritical velocity limits.

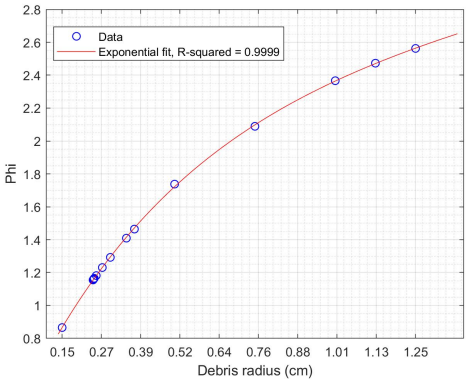

(a) $V = 1.1449V_{ia}$

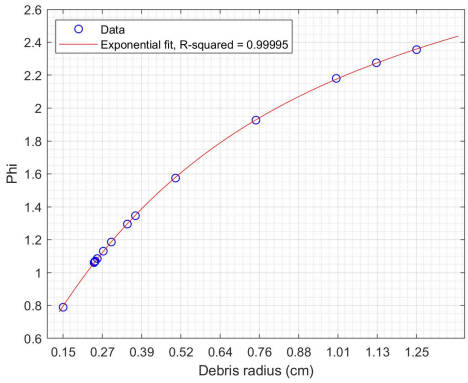

(b) $V = 1.0304V_{ia}$

Figure 3.17: Precursor soliton amplitude in High LEO Region 1 as a function of debris size for one velocity.

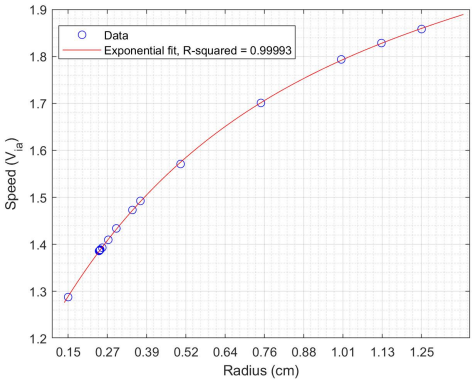

(a) $V = 1.1449V_{ia}$

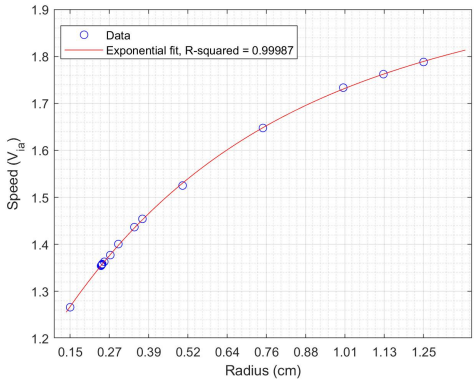

(b) $V = 1.0304V_{ia}$

Figure 3.18: Precursor soliton speed as a function of debris size for one velocity in High LEO Region 1.

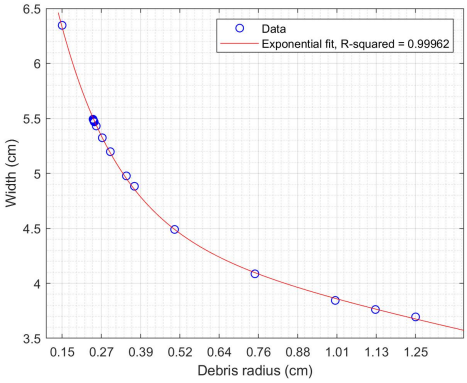

(a) $V = 1.1449V_{ia}$

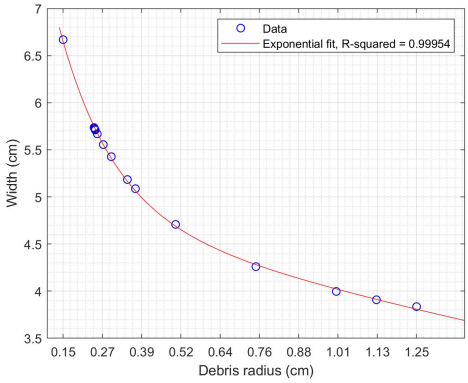

(b) $V = 1.0304V_{ia}$

Figure 3.19: Precursor soliton width as a function of debris size for one velocity in High LEO Region 1.

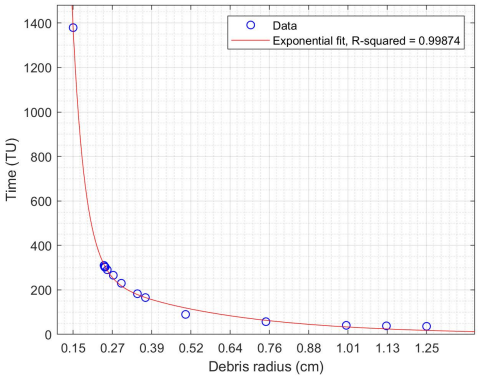

(a) $V = 1.1449V_{ia}$

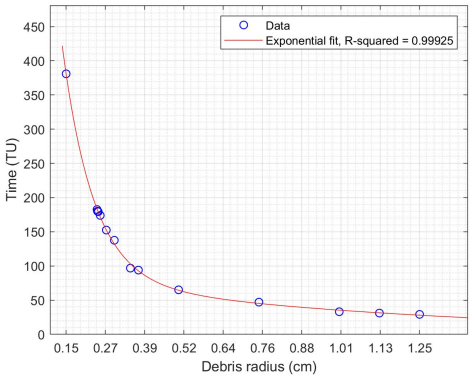

(b) $V = 1.0304V_{ia}$

Figure 3.20: Time required to produce the first precursor soliton as a function of debris size for one velocity in High LEO Region 1.

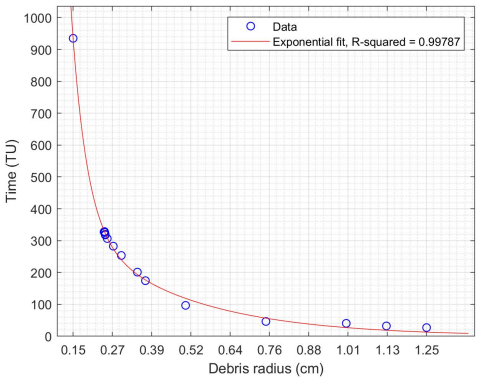

(a) $V = 1.1449V_{ia}$

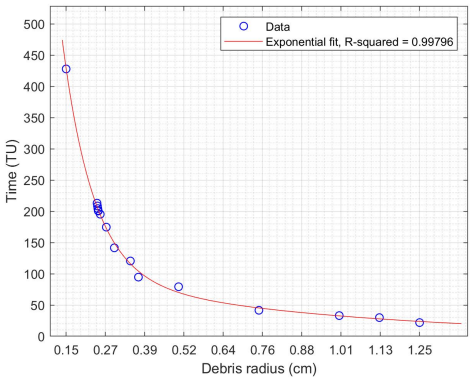

(b) $V = 1.0304V_{ia}$

Figure 3.21: Time between subsequent precursor solitons as a function of debris size for one velocity in High LEO Region 1.

3.8 Global Precursor Soliton Generation Trends

After investigating the size, charge, and speed of debris that will generate precursor solitons for the nominal plasma conditions in Table 3.1 and Table 3.2, we investigated precursor soliton generation using a global ionosphere plasma model in order to find the limiting altitude and latitude for precursor soliton generation. Using the global model, we queried plasma parameters at varying altitudes and latitudes to find the range of possible debris orbital velocities and eccentricities that would produce precursor solitons. From this investigation, we characterize the percentage of each altitude where precursor solitons can be generated, as a function of debris size.

3.8.1 Ionospheric Data

Ionospheric data was downloaded from the International Reference Ionosphere (IRI) model [17], hosted on NASA's Community Coordinated Modeling Center website, in order to explore seasonal and diurnal variations in soliton production. The IRI is an international project sponsored by the Committee on Space Research (COSPAR) and the International Union of Radio Science (URSI) to produce an empirical standard model of the ionosphere, based on all available data sources. For a given location, time and date, IRI provides averages of the electron density, electron temperature, ion temperature, and ion composition in the ionospheric altitude range from 60 km - 2000 km. The major data sources are the worldwide network of ionosondes, incoherent scatter radars (Jicamarca, Arecibo, Millstone Hill, Malvern,

St. Santin), ISIS and Alouette topside sounders, and *in situ* instruments flown on many satellites and rockets [17].

IRI data is available below 2000 km altitude. We downloaded ionosphere properties at 200 km - 2000 km altitude in 100 km increments, and -90 to 90 degrees latitude at 10 degree increments, for July 1, 2000 and January 1, 2000 to represent plasma conditions in the summer and winter, respectively. For each date, the data was downloaded at zero degree longitude for eight different local times: 12am/pm, 3am/pm, 6am/pm, and 9am/pm.

We interpolated between the altitudes and latitudes to calculate the ion acoustic velocity, the dominant ion species, and Debye length at each altitude/latitude location. Then, for a range of sub-centimeter debris sizes, the supercritical and subcritical velocities were calculated at each altitude/latitude queried according to Eqn 3.55 and Eqn 3.56.

3.8.2 Corotation

The Earth's plasmasphere rotates with the Earth in a rigid corotation [51, 53, 66]. The corotation velocity at a given altitude and latitude is given by:

$$V_{co} = \frac{2\pi(R_E + R_{alt})\cos(\theta_{lat})}{t_{sd}} \quad \text{(m/s)} \tag{3.57}$$

where V_{co} is in the eastward direction, R_E is the radius of the Earth, R_{alt} is the orbital altitude, θ_{lat} is the orbital latitude, and $t_{sd} = 86164$ s is the number of seconds in a sidereal day. The production of precursor solitons depends on the

speed of the debris relative to the background plasma. If the orbital debris velocity is parallel to the corotation direction, then the debris velocity relative to the ion acoustic velocity is $V_r = V_d - V_{co}$. If the orbital debris velocity is at an angle with respect to the corotation direction, then one must rotate both the debris velocity and the corotation velocity to the same coordinate system, and calculate the magnitude of the corotation velocity in the debris velocity direction. A precursor soliton will be generated if:

$$V_{sub} \leq \frac{V_d - \vec{V}_{co} \cdot \hat{V}_d}{V_{ia}} \leq V_{sup} \tag{3.58}$$

The angle between the debris velocity vector and the corotation velocity vector determines the contribution of the corotation velocity in the debris velocity direction:

$$\vec{V}_{co} \cdot \hat{V}_d = V_{co}\cos(\theta_{co}) \tag{3.59}$$

Thus, Eqn 3.58 becomes:

$$V_{sub}V_{ia} \leq V_d - V_{co}\cos(\theta_{co}) \leq V_{sup}V_{ia} \tag{3.60}$$

When corotation is included in the relative debris velocity, the range of valid transcritical velocities is increased, allowing for precursors to be created in a larger range of altitudes and latitudes. In general, in LEO, the ion acoustic velocity is less than the velocity of a circular orbit. For example, for High LEO with $V_{ia} = 5.75$ km/s, the circular orbit velocity for debris is $V_{d,circ} = 7.07$ km/s at 1600 km alti-

tude. When corotation is not included in the relative debris velocity, only elliptical orbits with the debris at apoapsis are possible when $V_d = V_{ia}$, which may result in periapsis below the Earth's surface. The corotation speed is $V_{co} = 0.58$ km/s at 0° latitude at 1600 km altitude, so $V_r = 6.49$ km/s, assuming that the debris velocity and corotation velocity are parallel. Since the circular orbit velocities in LEO are typically higher than the ion acoustic velocity, and the transcritical velocity limits are on the order of the ion acoustic velocity, the corotating ions in the background plasma effectively increase the number of valid elliptical and circular orbits that produce solitons.

For each orbit and queried altitude/latitude, if the relative debris velocity falls within the supercritical and subcritical velocity limits for the debris size, precursor solitons can be generated and the location is referenced in the subsequent figures as a 'precursor generation region'.

3.8.3 Orbits

For each debris size and altitude/latitude queried, a range of ten velocities between the V_{sup} and V_{sub} was used to calculate the valid orbits at that point, using Eqn 3.60. We define 'valid orbits' as orbits with an eccentricity $0 \leq e < 1$, periapsis greater than the radius of the Earth ($R_p > R_E$), and the magnitude of the flight path angle less than 90°. To find the range of eccentricities for real orbits that create precursor solitons, we need to consider orbits for all orbital elements. To consider a range of orbital debris velocity directions, the corotation velocity unit vector was

defined in the IJK coordinate system, then rotated about each of the three axes in 30° increments, to represent potential orbital debris unit vectors. The angle between the position and debris velocity vectors defines the flight path angle, γ_{F}:

$$\sin(\gamma_{\mathrm{F}}) = \hat{r} \cdot \hat{V}_d \tag{3.61}$$

where the magnitude of the position vector is $r = R_E + R_{alt}$.

In order to determine the range of eccentricities that produce precursor solitons, we combine the relationships for orbital angular momentum, h, and semilatus rectum, p.

$$h = rV_d\cos(\gamma_{\mathrm{F}}) = \sqrt{\mu_E p} \tag{3.62}$$

$$p = a(1 - e^2) \tag{3.63}$$

Substituting Eqn 3.63 into Eqn 3.62 leads to an expression for eccentricity:

$$e = \left(1 - \frac{(rV_d\cos(\gamma_F))^2}{\mu_E a}\right)^{1/2} \tag{3.64}$$

where μ_E is the Earth's gravitational parameter, and the semi-major axis, a, is given by the vis-viva equation:

$$a = \left(\frac{2}{r} - \frac{V_d^2}{\mu_E}\right)^{-1} \tag{3.65}$$

3.8.4 Resulting Debris Velocity and Eccentricity

Precursor soliton generation regions were identified using the IRI ionospheric data, the supercritical and subcritical velocity limits from Eqn 3.55 - Eqn 3.56, and the orbital limits described in 3.8.3. Each altitude, latitude, date, and time represents a grid point for which transcritical velocity limits and orbital parameters were calculated. For all of the IRI data, Fig 3.22 shows the minimum and maximum velocities as a function of debris size, that produce precursor solitons. Fig 3.23 shows the resulting minimum and maximum eccentricities. Precursor generation regions are shown in Fig 3.24 for 0.5 cm radius debris during the winter at 6am UTC on January 1 2000, with the reader at the Sun. Altitude increases outward from the Earth. The minimum and maximum debris velocities, V_d, for valid orbits shown in Fig 3.24 are shown in Fig 3.25.

Fig 3.26 shows the plasma characteristics for the simulation in Fig 3.24, which illustrates the requirements for the plasma conditions that must be met in order to produce precursors in LEO. In general, the location of the precursor generation region is first defined by the location of the dominant hydrogen ions, since the ion acoustic velocity will be comparable to the orbital velocity. Next, the precursor generation region will be defined by ratio of debris size to the Debye length, since the dimensionless debris size defines the transcritical velocity threshold in that region. Finally, the ion acoustic velocity is defined by the ion temperature, which increases with increasing altitude.

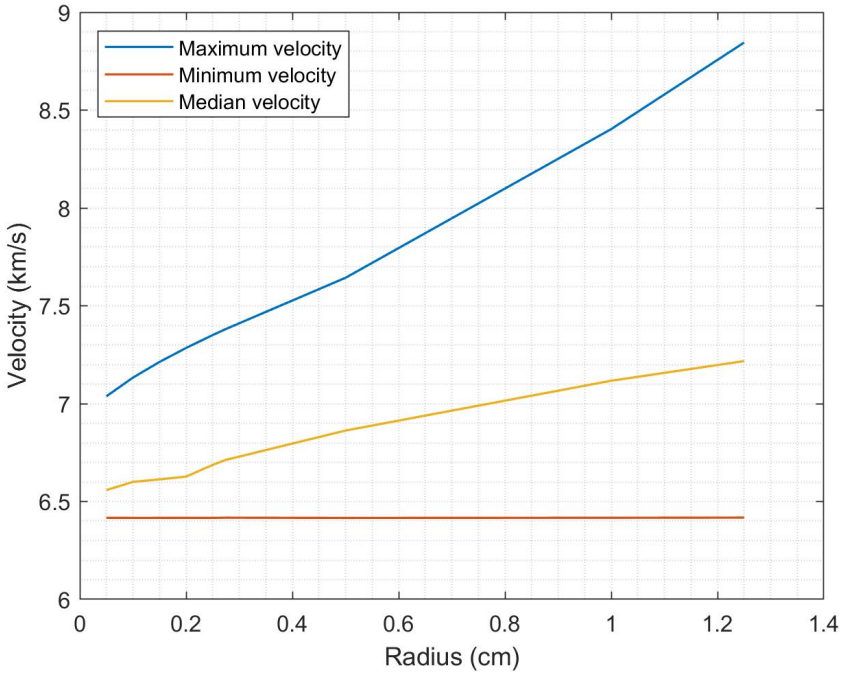

Figure 3.22: Minimum and maximum debris velocities, V_d, for valid orbits in LEO as a function of debris size.

3.8.5 Likelihood of Soliton Generation

For all of the IRI simulation data downloaded (described in 3.8.1), the minimum and maximum latitude and altitude for precursor soliton generation were calculated as a function of debris size, as shown in Fig 3.27. The plasma parameters change dynamically due to corotation, diurnal variations, and the intersection between the Earth's rotational and magnetic axes, causing some asymmetry in the precursor generation regions along the altitude and latitude lines, as shown in Fig 3.24 - Fig 3.27. The intersection between the rotational and magnetic axes is not located at the center of the Earth. Since the center points do not coincide, ge-

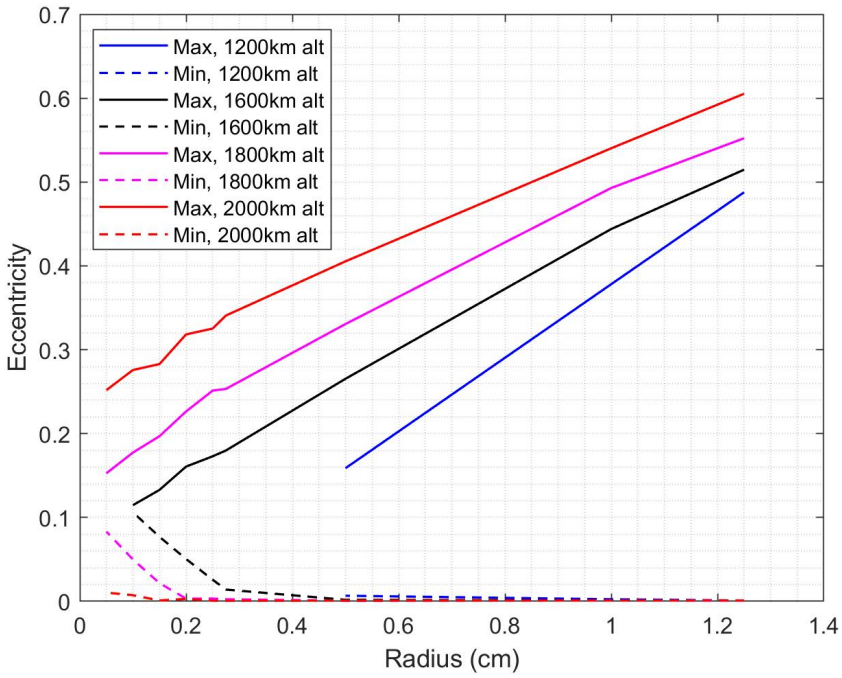

Figure 3.23: Minimum and maximum eccentricities for valid orbits in LEO as a function of debris size and altitude.

ographic and geomagnetic coordinates do not coincide, with differences shown in [67]. Due to the difference in axes, the inner radiation belt reaches low altitudes, down to 200 km, in a region known as the South Atlantic Anomaly. This region spans from $-50° \leq \theta_{lat} \leq 0°$ geographic latitude and $-90° \leq \theta_{lat} \leq 40°$ geographic longitude, and is more susceptible to high energy particles reaching low altitudes of the ionosphere.

Since the plasmasphere corotates with the Earth, it is exposed to the same diurnal alternation as the Earth's surface. There is zero ionization in the plasmasphere at night, and ionization increases during the day [54]. While recombination is low during the day, it increases at night. Additionally, at latitudes greater than

approximately $\theta_{lat} = \pm 60^{\circ}$ and altitudes above 2000 km, plasma is trapped along closed magnetic field lines, which are filled by plasma traveling outward from the ionosphere. The plasma is more dense on the morning side, after the recombination occurring at night. As a result, the plasmasphere on the night side extends to $6-7R_E$, while the maximum altitude on the day side plasmasphere is typically $4R_E$ [54]. In general, the plasma density is higher during the summer when compared to winter, and higher during the day when compared to night, as shown in [41]. The plasma density influences the transcritical velocity range, since the radius of the debris is normalized by the Debye length, which depends on density. A higher density will result in a larger transcritical velocity range, while a lower density will result in a smaller range. The difference in precursor generation regions for summer/winter and day/night using the IRI simulation results are shown in Fig 3.28.

The likelihood of precursor soliton generation was also calculated as a function of altitude. For all of the IRI simulation data results, a grid of points at a given altitude and latitude were generated. For eight different local times, 37 altitudes between 200 - 2000 km, and 37 latitudes between $-90^{\circ} - 90^{\circ}$, there are a total of 10,952 grid points for one day. For one altitude at all latitudes, there are a total of 296 grid points for one day. Two days, January 1, 2000, and July 1, 2000, were used to represent two different seasons. For each grid point, a range of velocities between the transcritical limits were considered, and the number of grid points for which valid orbits are produced were counted. If a grid point produced a precursor soliton for one or more velocities, it was counted once in the total number of grid points for which precursor solitons are produced. The number of grid points where precursor

solitons are generated for one altitude, divided by the total number of grid points for that altitude, is referred to as the 'percent of altitude' where precursor solitons are generated. Fig 3.29 shows the percentage of the grid points at a given altitude where precursor solitons are created as a function of debris size for July 1, 2000. As the debris size decreases, the transcritical velocity range decreases. The circular orbit velocity decreases as the altitude increases and approaches the ion acoustic velocity, allowing for debris with a small transcritical velocity range to produce precursor solitons. Additionally, the plasma density is higher at equatorial latitudes than at polar latitudes. The higher plasma density results in a smaller Debye length, which increases the transcritical velocity range. Thus, small debris are more likely to produce precursors at high altitudes and equatorial latitudes. Precursor solitons are more likely to be generated in summer when compared to winter. For 0.5 cm radius debris and considering all latitudes, 28% of the grid points with 2000 km altitude produce precursor solitons in the summer. When considering the equator only, 0° latitude, 63% of the equator grid points at 2000 km altitude produce precursors for 0.5 cm radius debris in the summer.

As shown in Table 3.6, debris much smaller than the Debye length will have $V_{sup} = V_{sub} = V_{ia}$. Therefore, even the smallest debris will produce precursor solitons if the debris velocity equals the ion acoustic velocity. There are some regions in the IRI simulation data where the ion acoustic velocity exceeds 6.5 km/s, approaching the velocity of a circular orbit. These regions mostly occur during the Summer at 9am and 3pm UTC, at altitudes greater than 1850 km and latitudes between $-60° \leq \theta_{lat} \leq 40°$. After querying the IRI simulation data with the incorporation of

corotating plasma as described in 3.8.2 and the orbital limits described in 3.8.3, the range of valid orbital velocities is $6.42 - 6.88$ km/s, and the range of eccentricities is $0.03 - 0.22$, where $V_{sup} = V_{sub} = V_{ia}$. At 2000 km altitude, these regions occur in 10% of all latitudes and 18.75% of equatorial latitudes. When the ion acoustic velocity approaches the velocity of a circular orbit, debris of any size will produce precursor solitons. While there is no lower limit to the debris size that will produce precursor solitons in these regions, the low amplitude of solitons produced by very small debris may not be detectable with existing technology.

3.9 Debris Precursor Solitons in other Plasma Environments

After identifying the minimum and maximum altitudes and latitudes where precursor solitons are generated in LEO in 3.8, we extend the analysis to other planetary bodies, medium Earth orbit (MEO), and geosynchronous orbit (GEO) inside the Earth's plasmasphere wake. Additionally, we discuss extending the precursor soliton simulations in 3D space, with two spatial dimensions and one wave amplitude dimension.

3.9.1 Precursor Solitons about other Planetary Bodies

In addition to detecting orbital debris at Earth, there is also an interest in detecting small, charged grains (e.g., dust ejected from a surface) at other planetary bodies. We investigate the ability for sub-centimeter grains to produce precursor solitons in other plasma environments. Solar wind plasma will interact with aster-

oids and other planetary bodies, producing plasma sheath around airless bodies, ionospheres around bodies with magnetic fields, and exospheres around bodies with atmospheres. Generally, the ion temperature in an ionospheric or exospheric environment will be lower than that of the free stream solar wind plasma, creating an ion acoustic velocity within the regime of orbital velocities for solar system bodies. Precursor solitons will be produced for a range of orbital velocities on the same order as the ion acoustic velocity. In the case of Ceres, the dominant ion is water in regions near the outgassing of water vapor from its surface, with an exospheric density of 10 cm^{-3} that extends for several Debye lengths [68]. Ceres is one of the asteroids most likely to produce solitons because since its large mass allows for a fast circular orbit velocity, and the water vapor outgassing allows for the slowest ion acoustic velocity. In the case of the Moon, an exosphere is present with density of approximately 10 cm^{-3} at 10 m altitude, and the exosphere extends to 50 m altitude [69]. The dominant ion in the lunar exosphere could be argon, neon, or helium, depending on surface composition interaction with the solar wind [70]. For Europa, which has a magnetic field to confine the plasma and thus increase the plasma density, the dominant ion is carbon dioxide, with densities of $5x10^3$ cm^{-3} at 50 km altitude and $2x10^3$ cm^{-3} at 200 km altitude [71].

Assuming a circular orbit, the minimum debris radius which can produce precursor solitons can be found by equating the orbital velocity to the transcritical velocity limits in Eqn 3.55 - Eqn 3.56, which results in the following expressions for debris radius, a, at the subcritical limit:

$$a = \begin{cases} -4\sqrt{3}\beta\lambda_D\sqrt{(V_{ia}-V_d)^3/(\beta V_{ia}^3)}/(3\sqrt{\pi}\alpha|\Phi_{p,n}|) & \text{if } V_{ia} < V_d \\ 4\sqrt{3}\beta\lambda_D\sqrt{(V_{ia}-V_d)^3/(\beta V_{ia}^3)}/(3\sqrt{\pi}\alpha|\Phi_{p,n}|) & \text{if } V_{ia} > V_d \end{cases} \tag{3.66}$$

Similarly, the minimum debris radius at the supercritical limit is:

$$a = \begin{cases} 4\sqrt{3}\beta\lambda_D\sqrt{-(V_{ia}-V_d)^3/(\beta V_{ia}^3)}/(3\sqrt{\pi}\alpha|\Phi_{p,n}|) & \text{if } V_{ia} < V_d \\ -4\sqrt{3}\beta\lambda_D\sqrt{-(V_{ia}-V_d)^3/(\beta V_{ia}^3)}/(3\sqrt{\pi}\alpha|\Phi_{p,n}|) & \text{if } V_{ia} > V_d \end{cases} \tag{3.67}$$

Fig 3.30 shows the resulting minimum debris radii that can produce precursor solitons as a function of electron temperature for Europa. The electron temperature influences both the Debye length and ion acoustic velocity. For the cases of Ceres and the Moon, assuming an electron temperature greater than 5 eV, objects must have at least a meter radius to produce precursor solitons. Since the exosphere altitudes about Ceres and the Moon are also on the order of meters, it is not expected that precursor solitons will be generated. Since Ceres represents the best case for precursor soliton production about asteroids, it is not expected that precursor solitons will be produced about other asteroids. However, for electron temperatures on the order of 1 eV, it is possible for sub-cm orbital debris to produce precusor solitons about Europa. For an electron temperature of 10 eV at Europa, the minimum debris radius for soliton generation is tens of centimeters.

3.9.2 Precursor Soliton Generation in Medium Earth Orbit

The small debris population in MEO, which is defined at altitudes between 2000 - 38268 km ($6R_E$), is not well understood, and NASA believes that previous *in situ* measurements in LEO underestimate the amount of debris at higher altitudes [6]. The ability for ground based radar to detect small debris objects decreases rapidly with altitude. Currently, the minimum sized object that can be detected with ground based radar and optical methods is 1 meter in diameter at 5000 km[72]. With the increase in number of satellites planned for MEO orbits, the likely increase in debris objects in MEO will drive the need for understanding the growing debris population in order to reduce the risk for satellite failure.

The transition between the oxygen to hydrogen dominated regions in plasmasphere occurs below 2000 km altitude [36, 37, 38], with the transition region modeled in the IRI data used in 3.8.4. While the IRI data is limited to 2000 km altitude, precursor generation will likely extend above 2000 km altitude assuming that the plasma density gradually changes at the same rate as the plasma in the topside ionosphere, without geomagnetic disturbances [54]. The density of the plasmasphere extending into MEO depends on solar activity [73]. For our simulations we assume the density of the quiet pre-disturbance plasmasphere. To examine the likelihood of precursor soliton generation in MEO, plasma density was assumed to vary gradually as shown in [73], with a linear transition from $10^4 - 10^2$ cm^{-3} between 2000 - 38268 km ($6R_E$) altitude [54, 73] for latitudes $-50^\circ \leq \theta_{lat} \leq 50^\circ$. For polar latitudes, it was assumed that the density decreases by 10 percent, and ranges from

$10^3 - 10^1$ cm^{-3} between 2000 - 38268 km ($6R_E$) altitude. Results were modeled with typical ion temperatures in MEO of $T_e = T_i = 1$ eV [54].

Given these plasma conditions, the potential for precursor generation extends into MEO for sub-centimeter debris. Similar to the LEO results shown in 3.8.4, the maximum altitude where precursor solitons are generated is shown in Fig 3.31. The minimum altitude for all cases is 2000 km, which is the limiting altitude for MEO. Precursor solitons are generated at all latitudes. A grid of points for 73 altitudes between 2000 - 38268 km and 37 latitudes between $-90°$ to $90°$ was used to calculate the likelihood of soliton generation as a function in MEO, for a total of 2701 grid points. For one altitude, there are 37 grid points for all latitudes. The number of grid points where precursor solitons are generated for one altitude, divided by the total number of grid points for that altitude, is referred to as the 'percent of altitude' where precursor solitons are generated. The percentage of altitude in MEO where precursor solitons are generated as a function of debris size is displayed in Fig 3.32, assuming $T_e = T_i = 1$ eV. The minimum and maximum orbital eccentricity for a 0.5 cm radius debris is shown in Fig 3.33. The ion acoustic velocity is $V_{ia} = 9.79$ km/s for $T_e = 1$ eV, which is greater than circular orbit velocities in MEO. Therefore, the resulting valid orbits for which precursor solitons are created have a high eccentricity.

Note that at 2000 km altitude, typically $T_e = T_i = 0.35$ eV in the IRI data, in contrast to the $T_e = T_i = 1$ eV assumed in our calculations for MEO. Lower plasma temperatures will decrease the ion acoustic velocity, thereby bringing it closer to the circular orbit velocity, resulting in a larger precursor generation region and greater range of eccentricities than predicted here.

3.9.3 Precursor Soliton Generation inside the Earth Plasmasphere in Geosynchronous Orbit

We also consider debris in geosynchronous orbit about the Earth. The debris will cross into the Earth's plasmasphere on the wake side of the Earth, which extends to six Earth radii [54, 73]. The dominant ion in this plasma is hydrogen, with a density of 10 cm^{-3}, electron temperature of 1 eV [54, 73], and Debye length of 2.35 m. For geosynchronous orbit in the Earth's plasmasphere, using Eqn 3.66-Eqn 3.67, the object radius must be at least 92.5 cm in size to produce precursor solitons. Thus, the dimensionless force width is $G = 0.39$, which is captured in our numerical model.

3.9.4 Future Work: Soliton Propagation Direction and Distance

In this investigation, we have considered the propagation of plasma solitons in a uniform, constant plasma environment. However, the plasma environment changes with time of day and location. Future work will investigate the dissipation of solitons produced by orbital debris as those solitons encounter varying plasma environments. Solitons will propagate without collisional damping until they reach an area of turbulence or a higher energy kappa distribution, which could have a different α or β, and $\gamma > 0$. Additionally, the forcing function will change in width due to the changing Debye length at varying altitudes. Future work will investigate the propagation of solitons in regions where the damping coefficient transitions from

$\gamma = 0$ to $\gamma > 0$.

Typically, the Boussinesq equations [44] are used to describe full water wave theory, which allow for wave propagating in multiple directions, and wave influence in the transverse direction as well. However, the KdV approximation is a simplification of the Boussinesq equations and only admits waves traveling in one direction [2, 44, 57]. From the dispersion relation, it is shown that the wave is dispersive and propagates in only one direction, since there is only one sign for a given wavenumber. Using the KdV approximation, it is expected that solitons generated from orbital debris will propagate unidirectionally from the debris location [44]. Our current results model the solitons generated at the peak height of the Gaussian forcing term, but it is possible that solitons will also be generated along the width of the Gaussian as the height decreases, similar to the semicircular shape observed in [16] and recent ocean wave simulations [74]. To understand the 3D (2+1) propagation of solitons, with two spatial dimensions and one wave amplitude dimension, future work will employ the forced Kadomtsev-Petviashvili (KP) equation, which extends the forced KdV equation into three dimensions [75, 76]. The KP equation has been used to model ion-acoustic waves in weakly magnetized or unmagnetized, cold, Maxwellian plasmas [77, 78, 79].

3.10 Conclusions

An on-orbit, non-collisional method to detect sub-centimeter debris at a range of altitudes would advance our understanding of the small debris population. For

the first time, we have applied the forced KdV equation to charged orbital debris using conditions defined by the Earth's plasma environment, and simulated the resulting plasma density solitons which propagate along the debris velocity vector. We have demonstrated that small charged orbital debris can create pinned solitons in the O+ dominated regions of mid-latitude low LEO, up to 800 km altitude, and precursor solitons in H+ dominated high LEO, between 800 km - 2,000 km altitude. Pinned solitons can be detected from ground sensors using the same techniques used to measure plasma density irregularities. Precursor solitons could be detected using on-orbit Langmuir probes, since the solitons advance ahead of the debris. These solitons can be used to map previously non-trackable sub-centimeter orbital debris, providing a new capability to characterize the small orbital debris population. Results show that 0.5 cm radius debris can produce precursor solitons at altitudes down to 1000 km, 0.5 mm radius debris can produce precursor solitons at altitudes down to 1700 km, and micron sized debris can produce precursor solitons at altitudes down to 1850 km. Precursor solitons are more likely to occur in mid-latitude regions, which cannot be observed by current ground based radar and optical methods. We have also developed equations for the maximum and minimum debris velocities that will produce precursor solitons. Precursor soliton properties such as the amplitude, width, speed, and frequency are predicted as a function of debris size, velocity and location. The properties of precursor solitons that are outlined here enable the design of orbital debris detection methods.

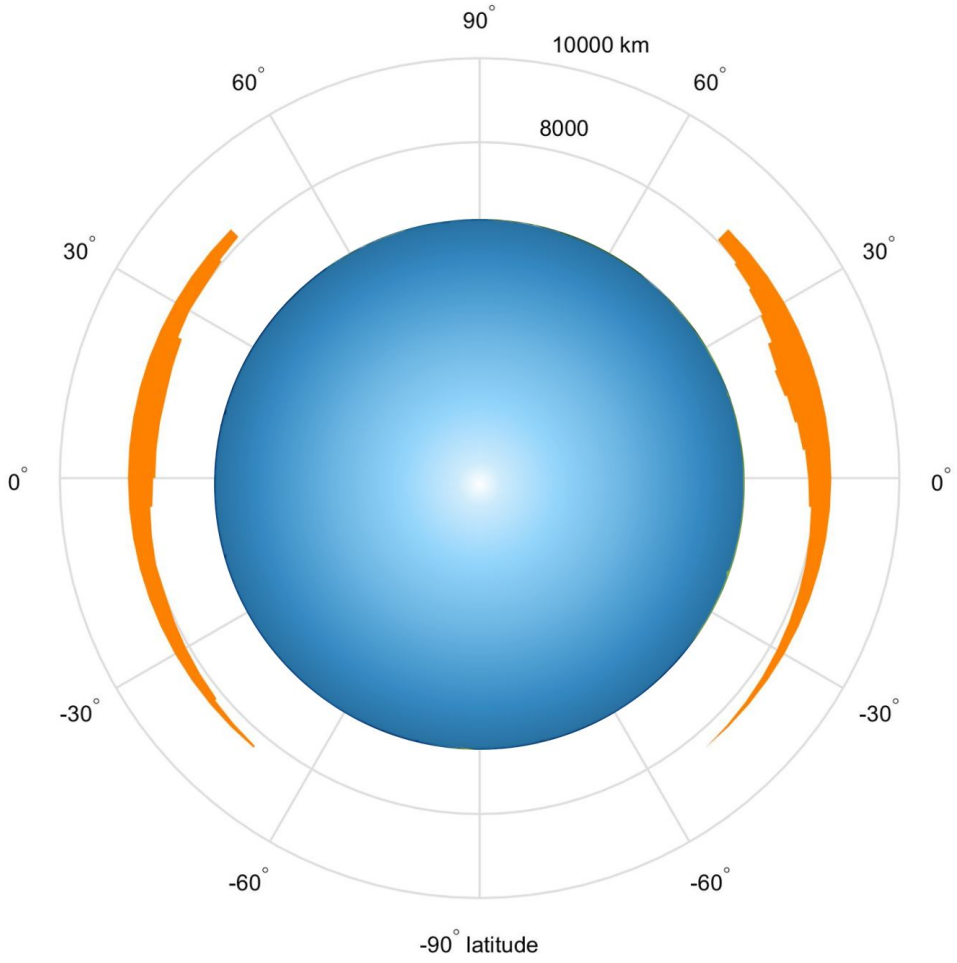

Figure 3.24: Precursor soliton generation region (orange) for 0.5 cm radius debris during Winter at 6am UTC. Distance outward includes the Earth's radius, 6378 km. The reader is located at the Sun. Left: Longitude is 180°. Right: Longitude is 0°.

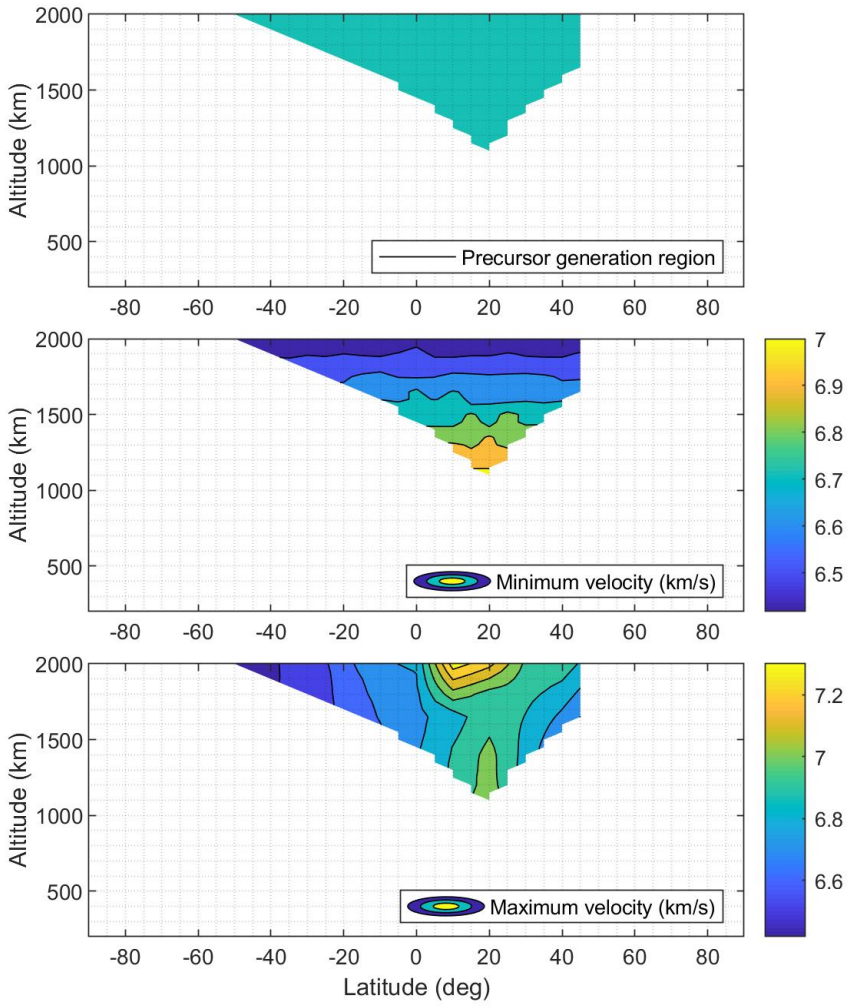

Figure 3.25: Minimum and maximum debris velocities, V_d, for valid orbits of 0.5 cm radius debris during Winter 6am UTC time at 0° longitude.

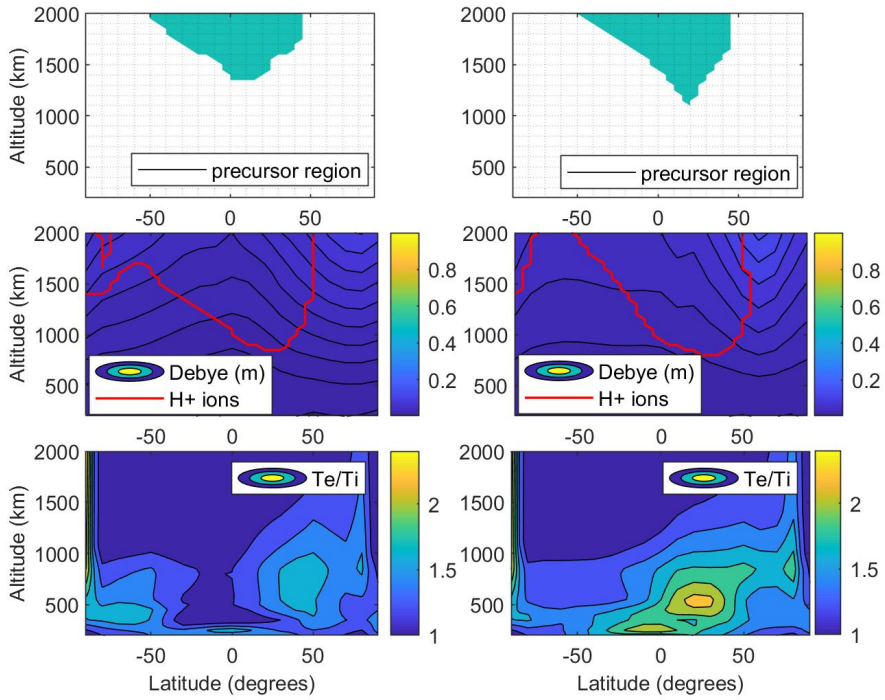

Figure 3.26: Precursor soliton generation region and plasma parameters for a 0.5 cm radius debris during Winter 6am UTC time. Left: Longitude is 180°. Right: Longitude is 0°. First row: Precursor generation region. Second row: location of the dominant hydrogen ion region and the Debye length in meters. Third row: the ratio of electron temperature to ion temperature.

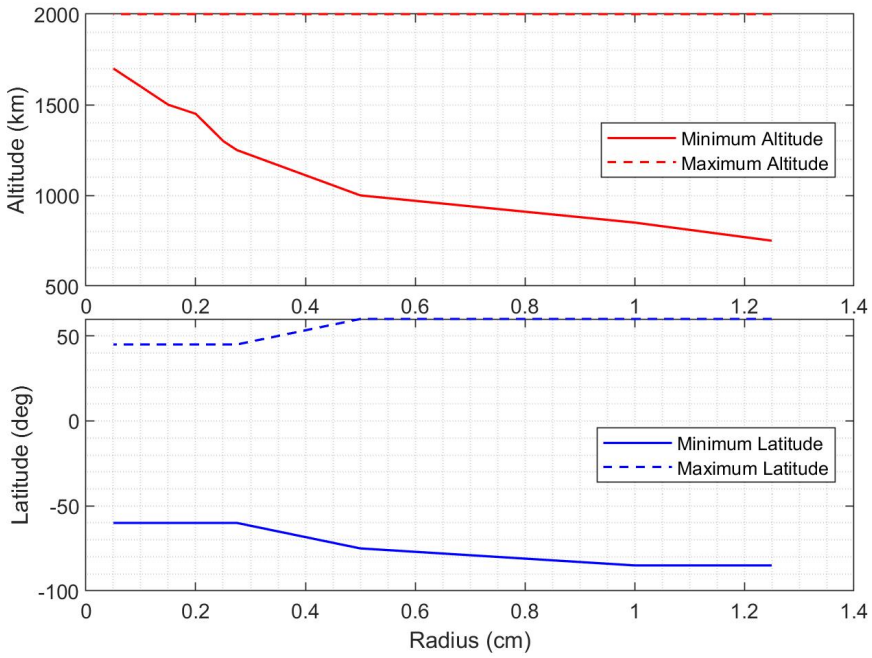

Figure 3.27: Minimum and maximum altitude and latitude in LEO where precursor solitons are generated as a function of debris size. The limiting altitude in the ionospheric model used is 2000 km.

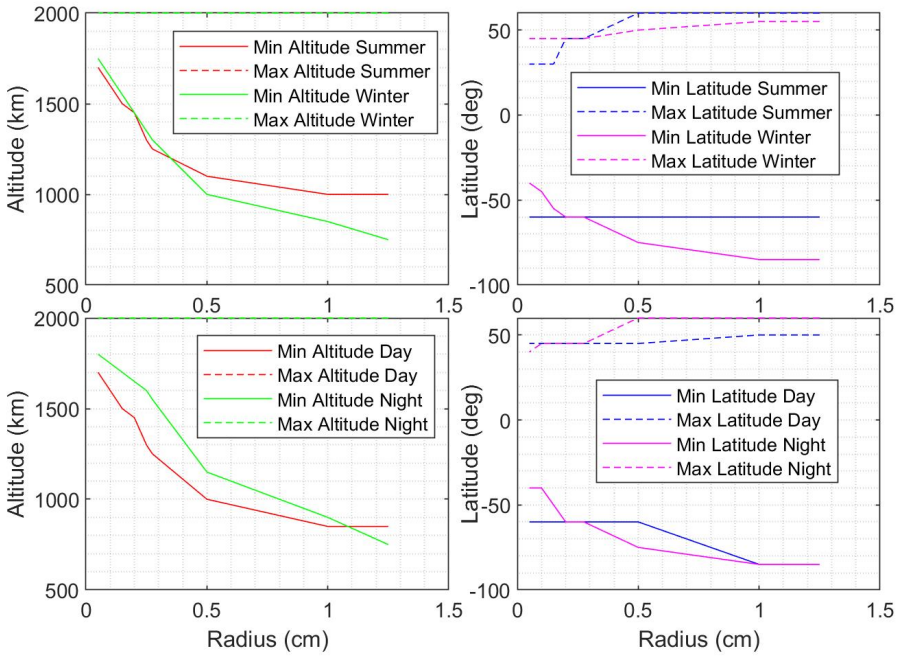

Figure 3.28: Minimum and maximum altitude and latitude in LEO where precursor solitons are generated as a function of debris size. Top subplots shows the difference in altitude between July 1 2000 (summer) and January 1 2000 (winter). The bottom subplots show the difference between day and night.

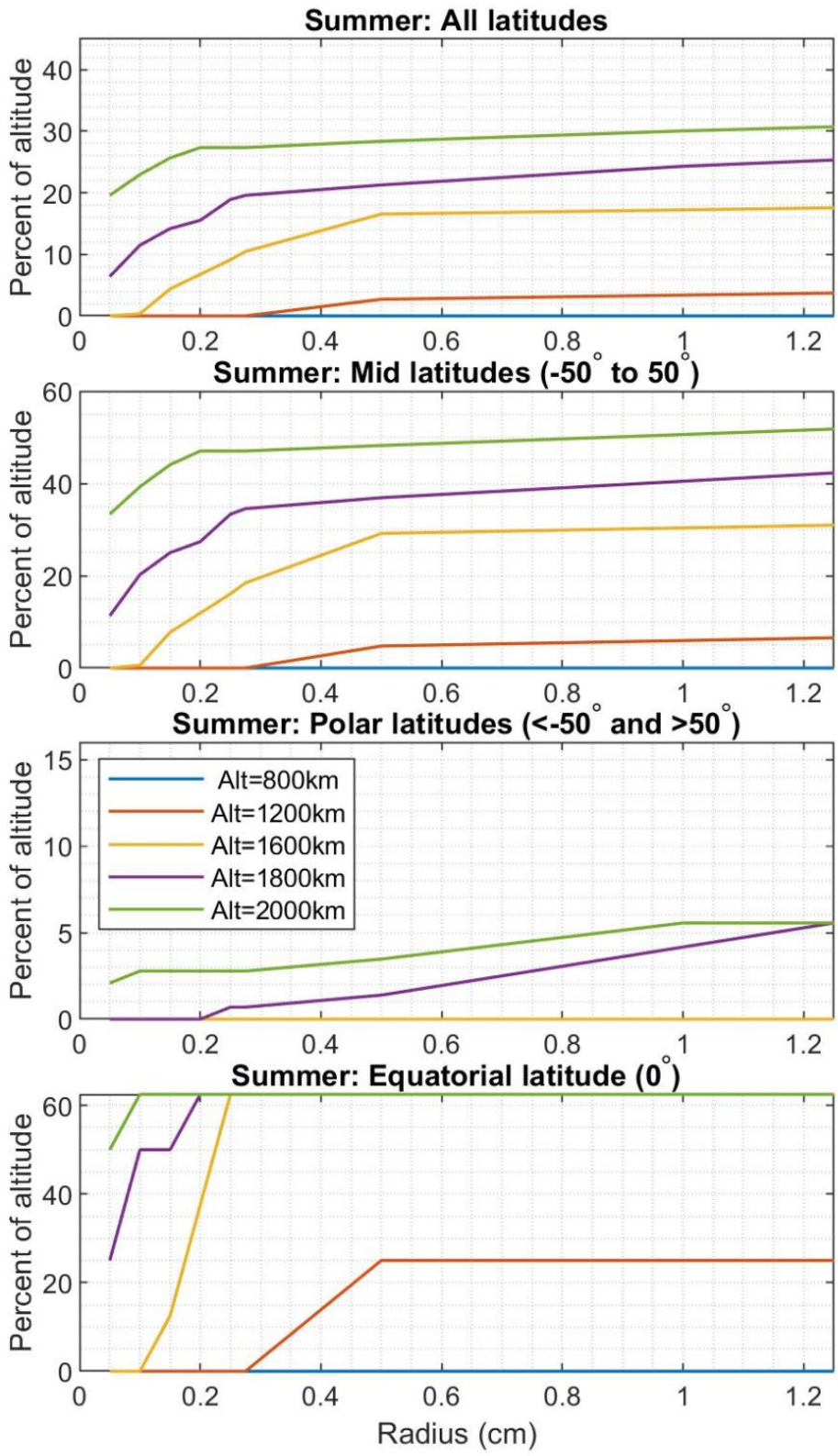

Figure 3.29: Percentage of altitude in LEO where precursor solitons are generated as a function of debris size.

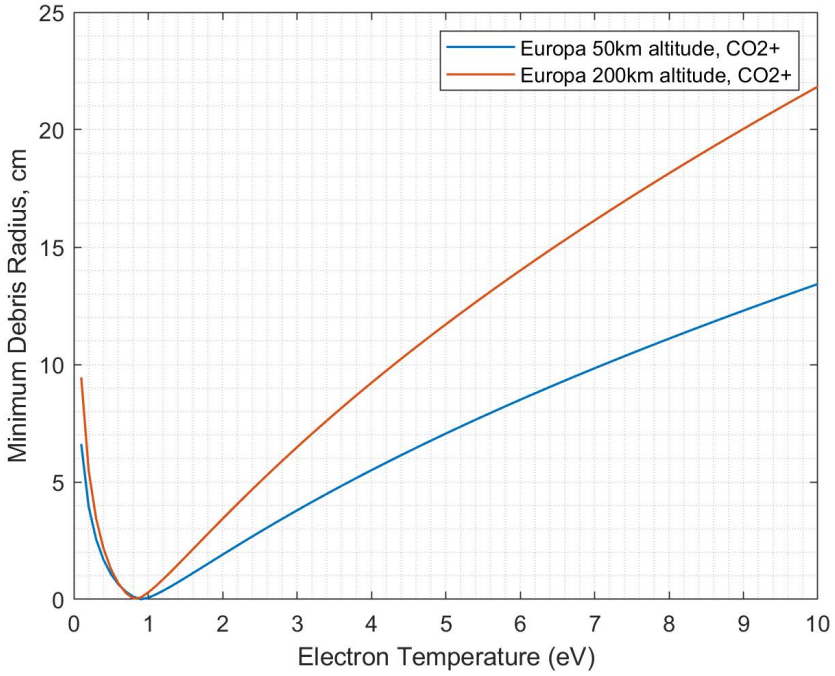

Figure 3.30: Minimum debris radius that can produce precursor solitons in the plasma environment about Europa, as a function of electron temperature.

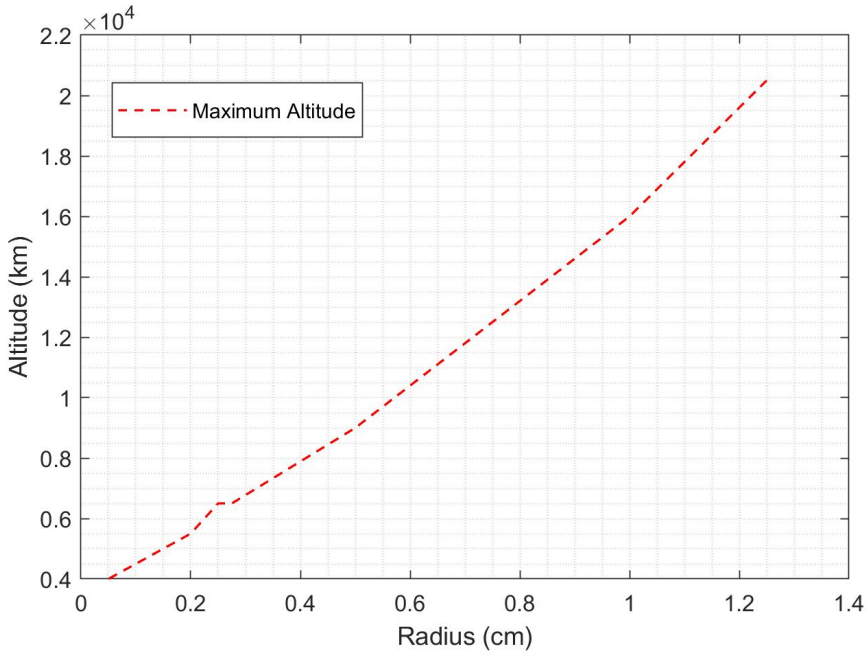

Figure 3.31: Maximum altitude in MEO where precursor solitons are generated as a function of debris size.

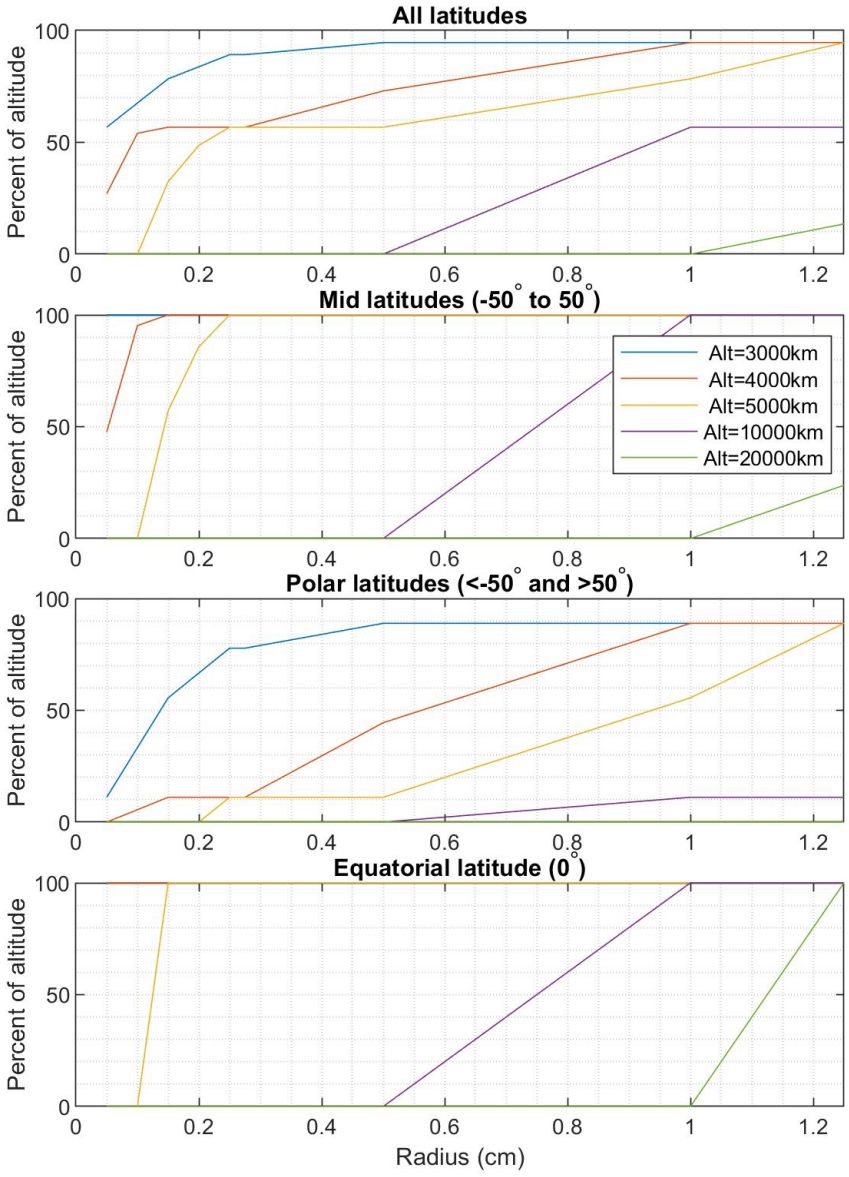

Figure 3.32: Percentage of altitude in MEO where precursor solitons are generated as a function of debris size.

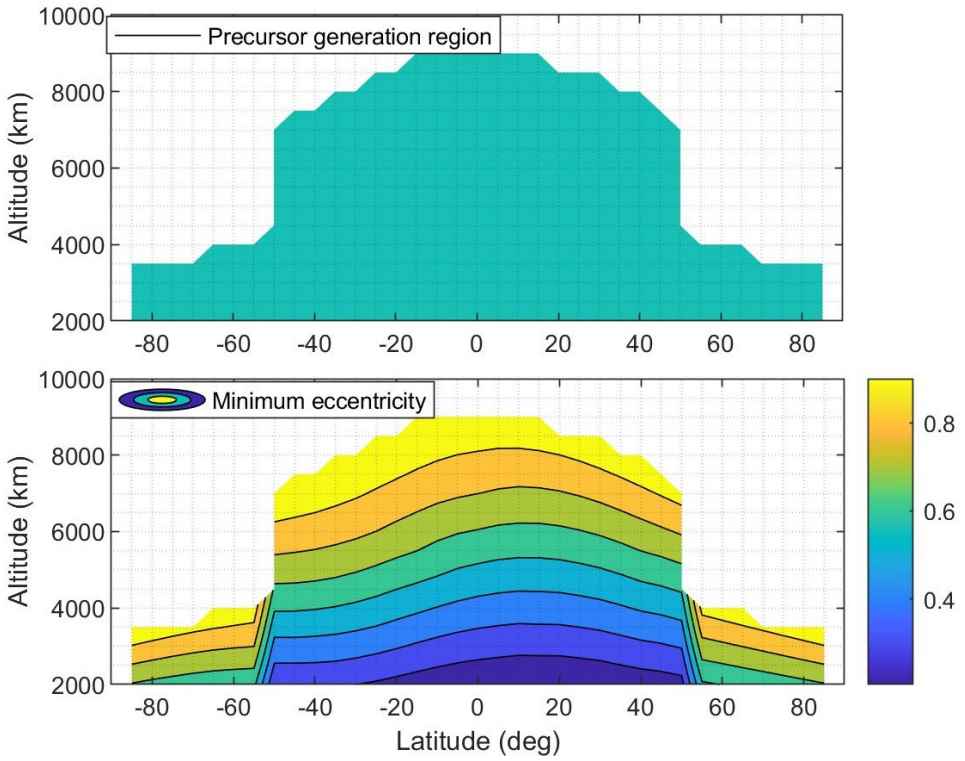

Figure 3.33: Minimum eccentricity for valid precursor-generating orbits in MEO for 0.5 cm radius debris. The maximum eccentricity is 1 for all cases.

Chapter 4: Simulating Damped Solitons from Orbital Debris in One Spatial Dimension

Assuming a uniform environment, solutions to the fKdV equation will result in solitons that propagate forever without damping. However, a nonuniform environment or kinetic collisions between solitons and ions or electrons in the plasma could cause the solitons to dampen. Damped solitons will travel a finite distance, which will define their detectability. In Chapter 4, we investigate the propagation distance of orbital debris solitons in the presence of damping processes.

The content of this chapter has been accepted for publication as Truitt and Hartzell, "Simulating Damped Ion Acoustic Solitary Waves from Orbital Debris," Journal of Spacecraft and Rockets, 2020. [80]

4.1 Damped Forced Korteweg–de Vries Equation

Since the ions in the Earth's plasma environment are colder than the electrons, we can approximate the ion motion with a plasma fluid model. The Boltzmann equation is used to derive the plasma fluid equations. In the absence of damping processes, the forced KdV (fKdV) equation has been derived from first principles from the plasma fluid equations to describe perturbations in the ion density as a

result of charged debris. Solitons are wave solutions to this equation when the steepening and dispersion forces are balanced. This derivation is covered in more detail in Chapter 3.

For IASWs, the coefficients to the KdV equation have been derived in literature for complex plasmas with strong magnetic fields, dust, and superthermal electrons with $\kappa-$distributions using a damped KdV (dKdV) equation as shown in Eqn 4.1. The spatial and temporal variables, ξ and τ, are the derived stretched coordinates of the initial boundary-value problem. The ξ domain is in units of the Debye length, and τ is in units of Debye length divided by the ion acoustic velocity. One time unit (TU) is λ_D/V_{ia}. The damped unforced KdV equation is:

$$\frac{\partial U}{\partial \tau} + \alpha U \frac{\partial U}{\partial \xi} + \beta \frac{\partial^3 U}{\partial \xi^3} + \gamma U = 0 \tag{4.1}$$

Similarly, the damped forced KdV equation is:

$$\frac{\partial U}{\partial \tau} + \alpha U \frac{\partial U}{\partial \xi} + \beta \frac{\partial^3 U}{\partial \xi^3} + \gamma U = \frac{1}{2} \frac{\partial f}{\partial \xi} \tag{4.2}$$

In our normalized system, the soliton amplitude displayed is the perturbed ion density normalized by the unperturbed ion density, $U = (n - n_0)/n_0$. For example, a soliton with an amplitude of 2 corresponds to 3x the unperturbed ion density. The increase of local ions is driven by the electrostatic potential surrounding the debris. The KdV equation is widely used in the theory of long internal waves and describes nonlinear waves, even when their amplitudes are not small, as long as the amplitude is smaller than the wavelength [81, 82, 83]. The coefficients α and β

define the weighting of the steepening and dispersion terms, and γ is the coefficient for the additional damping term [45, 46, 47, 48]. We assume a cold plasma with negligible dust density and a weak magnetic field. The velocity distributions of space plasmas typically have a suprathermal tail and are best modeled with a kappa (κ) distribution instead of a Maxwellian model [49, 50]. Applying the kappa distribution estimated from recent Earth magnetospheric models ($\kappa = 100$) [52], the coefficients are derived as $\alpha = 1.0051$, and $\beta = 0.4925$ in Chapter 3.

Orbital debris with radius, a, will become charged due to the flow of electrons and ions in the plasma environment, and create a perturbation in the electric potential and density of the surrounding plasma. The forcing term, f, in the fKdV equation is estimated as a Gaussian shape with V_d as the debris velocity. The debris surface potential, Φ_s, defines the plasma potential, Φ_p, at a distance, r, away from the debris, so that $\Phi_p = \Phi_s \exp(-r/\lambda_D)$. The normalized plasma potential is divided by the electron temperature, $\Phi_{p,n} = \Phi_p(e/k_B T_e)$, to represent the force amplitude, and a/λ_D is the full width at half maximum [57]:

$$f(\xi, \tau) = \Phi_{p,n} \exp\Big[- \Big(\frac{\xi - V_d \tau}{a/\lambda_D} \Big)^2 \Big] \tag{4.3}$$

The ability for orbital debris to produce pinned or precursor solitons depends on the relative velocity between the debris and the plasma medium. Pinned solitons travel with the debris, at the same speed as the debris, and occur above the supercritical limit where $U(0) = U(\infty)$. No solitons are produced below the subcritical limit, where $U(0) = U(\infty) = 0$. The transcritical region, where precursor solitons

are produced, resides between the subcritical and supercritical limits, and can be derived from Eqn 4.2 by solving for the relative velocity between the force and plasma medium [44]. Precursor solitons advance ahead of the force. The velocity of the force at the supercritical and subcritical limit, in units of the ion acoustic velocity, V_{ia}, is defined as [44]:

$$V_{sup} = 1 + \left(\frac{3(\alpha/2)^2 A^2}{16\beta}\right)^{1/3} \tag{4.4}$$

$$V_{sub} = 1 - \left(\frac{3(\alpha/2)^2 A^2}{4\beta}\right)^{1/3} \tag{4.5}$$

where the area of the Gaussian force is [57]:

$$A = |\Phi_{p,n}|\sqrt{\pi}a/\lambda_D \tag{4.6}$$

4.2 Numerical Methods

The Chan & Kerkhoven (CK) [27] pseudospectral scheme was used to simulate the solitons. There are few examples that describe the application of a pseudospectral method to the forced KdV equation, and we implement the Fourier transform of the forcing function as outlined by Shen [44]. The method was written in Matlab and applied to known analytic solutions to the fKdV [2, 57, 58]. Comparisons between our simulations and undamped analytic solutions are provided in Chapter 3.

In a pseudospectral scheme, the spatial domain $[-L, L]$ is discretized into N equidistant points and is normalized to $[0, 2\pi]$. Now, $\Delta\xi = \frac{2\pi}{N}$ and $\xi = s(x + L)$, where $s = \frac{\pi}{L}$ so that the solution is periodic from 0-2π.

For the Chan & Kerkhoven (CK) method, the finite difference approximation is applied to the time derivative, and a leapfrog method is used for the spatial derivatives, which reduces the number of Fourier transforms required for each time step. Thus, Chan-Kerkhoven is recognized as the fastest method to date for solving the KdV equations [28].

The numerical solution for the damped forced KdV equation becomes:

$$U^{n+1} = \mathscr{F}^{-1}\Big[\frac{1}{1 - \Delta t\beta i s^3 k^3}((1 + \Delta t\beta i s^3 k^3)\mathscr{F}(U^{n-1}) - \Delta t\alpha i s k \mathscr{F}(U^n)^2 \\ -\Delta t\gamma \mathscr{F}(U^n) + \Delta t i s k \mathscr{F}(f))\Big] \tag{4.7}$$

where $\mathscr{F}$ is the Fourier transform, $\mathscr{F}^{-1}$ is the inverse Fourier transform, and superscripts for U are in the temporal domain. Thus, $n+1 = \tau + \Delta\tau$ and $n-1 = \tau - \Delta\tau$.

To implement the scheme in Matlab, we first initialized the space by defining the input parameters α, β, N, L, V_d, f, $\Delta\tau$, τ_0, and τ_{final}. Next, we defined the mesh space, ξ, and the wave numbers, k. To reduce computation times for narrow forcing functions that required a larger N to resolve the force, we defined a smaller L and non-periodic boundary so that the wave solution does not wrap from the right to left spatial boundaries.

4.3 Damping Processes

After validating our pseudospectral scheme for the undamped KdV equation in Chapter 3, both forced and unforced, we proceeded to incorporate damping processes into the KdV equation, both forced and unforced. Typical damping processes introduced into the damped KdV equation include (a) magnetosonic waves damped by electron-ion collisions, (b) ion sound waves damped by ion-neutral collisions, (c) ion sound waves with Landau damping, and (d) shallow water waves damped by viscosity [48]. We will show in Section 4.3.1 that magnetic field effects on ion acoustic solitons created from orbital debris are negligible, so (a) does not apply. Since (d) is specific to shallow water waves, the remaining damping sources that apply to electrostatic ion acoustic solitons in plasma are ion-neutral collisions and Landau damping.

In the case of ion-neutral collisions, where ϑ is the rate of ion-neutral collisions, the damping coefficient, γ, is [46, 48]:

$$\gamma = \frac{\vartheta}{2} \tag{4.8}$$

In the case of Landau damping, the energy of particles in the plasma may resonate with the energy of the ion acoustic wave, if the velocity of the particle is comparable to the velocity of the wave, causing the particle to dampen the wave [84]. For Landau damping, γ is defined by the principal component of the perturbed distribution function [48]:

$$\gamma = \frac{P}{2} \int_{-\infty}^{\infty} \frac{\partial n}{\partial \xi'} \frac{d\xi'}{\xi - \xi'} \tag{4.9}$$

4.3.1 Collisional Damping

It is necessary to compare the magnitude of the ion plasma frequency, ω_{pi}, to the ion cyclotron frequency, ω_{Bi} to see if kinetic collisions or magnetic field effects will have an influence on the coefficients or velocity of the normalized forcing function, [45, 46].

$$\omega_{pi} = \sqrt{\frac{e^2 n_i}{\epsilon_o m_i}} \tag{4.10}$$

$$\omega_{Bi} = \frac{eB}{m_i} \tag{4.11}$$

where the Earth's magnetic field strength, B, is 3x10^{-5} Tesla at the equator. In Low LEO, the dominant ion is oxygen, with a mass of 2.67x10^{-26} kg, and a nominal density of 2x10^5 cm^{-3} at 700 km altitude [34]. In High LEO, the dominant ion is hydrogen, with a mass of 1.67x10^{-27} kg, and a nominal density of 10^5 cm^{-3} at 1200 km altitude [34]. Since $\omega_{Bi} \ll \omega_{pi}$, the effect of the magnetic field is negligible and 1D ion acoustic wave solutions are sufficient. Similarly, for the electron cyclotron frequency, $\omega_{Be} = eB/m_e$, and the electron plasma frequency, $\omega_{pe} = \sqrt{(e^2 n_e)/(\epsilon_o m_e)}$, $\omega_{Be} \ll \omega_{pe}$. Thus, we can ignore magnetic field effects [53]. Future efforts should incorporate the magnetization of electrons in the electron distribution function for regions where the electrons are magnetized.

To consider the influence of ion-neutral collisions on soliton production, we consider the ion-neutral collision frequency in Eqn 4.12, taking into account the number of neutrals, n_n, the ion acoustic velocity, V_{ia}, and the velocity-dependent cross section, $\sigma(V)$. The ion-neutral collision frequency, ν_{in}, is normalized by the ion plasma frequency in our dimensionless system, so that $\vartheta = \nu_{in}/\omega_{pi}$ in Eqn 4.1 and Eqn 4.8.

$$\nu_{in} = n_n V_{ia} \sigma(V) \tag{4.12}$$

To calculate the damping coefficient for ion-neutral collisions in Eqn 4.8, the ion-neutral collision frequency in Eqn 4.12 is divided by twice the plasma frequency. At altitudes below 400km, the neutral density exceeds the electron density [35, 54], causing ion-neutral collisions [53], so $\gamma > 0$. However, above 400km, n_n/n_e decreases [35], ion-neutral collisions are negligible and $\gamma = 0$. Since the plasmasphere is fully ionized [54], $n_n/n_e << 1$ and $\gamma = 0$. Since the dissipation coefficient $\gamma = 0$, we assume that solitons will propagate without collisional damping in a uniform environment.

4.3.2 Landau Damping

Earth's ionospheric plasma is a multi-component plasma containing positive oxygen, hydrogen, and helium ion species, and negative electrons. To understand the effects of Landau damping in the Earth's plasma environment, we adopt Arshad *et al.*'s model for Landau damping of ion acoustic waves due to electrons and ions

in a kappa-distributed multi-ion plasma [85]. In the long wavelength limit and assuming the same ion temperature, $T_{\alpha_1} = T_{\alpha_2} = T_i$, the damping rate normalized by the wave frequency, ω_r, is given as [85]:

$$\begin{aligned}\frac{\gamma}{\omega_r} = -\sqrt{\frac{\pi}{8}}\frac{\Gamma(\kappa+1)}{\Gamma(\kappa-1/2)}\frac{\sqrt{N_0^{12}}}{2^{3/2}(\kappa-1/2)^{3/2}}\Bigg[\sqrt{\frac{m_e}{m_{i1}}} \\ +\Big(\frac{n_{0i1}}{n_{0e}}\Big)\beta^{3/2}\Big[1+\frac{\beta N_0^{12}}{2(2\kappa-1)}+\frac{3\delta}{(2\kappa-3)N_0^{12}}\Big]^{-\kappa-1} \\ +\Big(\frac{n_{0i2}}{n_{0e}}\Big)\beta^{3/2}\sqrt{\frac{m_{i2}}{m_{i1}}}\Big[1+\frac{\beta N_0^{12}}{2(2\kappa-1)}+\frac{3\delta}{(2\kappa-3)N_0^{12}}\frac{m_{i2}}{m_{i1}}\Big]^{-\kappa-1}\Bigg]\end{aligned} \tag{4.13}$$

where $\beta = T_e/T_i$ is the ratio of electron to ion temperature, $N_0^{12} = \left[\frac{n_{0i1}}{n_{0e}} + \frac{n_{0i2}}{n_{0e}}\frac{m_{i1}}{m_{i2}}\right]$ and $\delta = \left[\frac{n_{0i1}}{n_{0e}} + \frac{n_{0i2}}{n_{0e}}(\frac{m_{i1}}{m_{i2}})^2\right]$ are relationships between the dominant ion density, n_{0i1}, secondary ion density, n_{0i2}, electron density, n_{0e}, dominant ion mass, m_{i1}, and secondary ion mass, m_{i2}. Normalized damping rates $\left|\frac{\gamma}{\omega_r}\right|$ as a function of $\beta = T_e/T_i$ electrostatic ion acoustic waves are shown in Fig 4.1 for a plasma with dominant/secondary ions O+/H+, representing Low LEO. A plasma with H+/He+, representing High LEO, is shown in Fig 4.2. Results are provided for different ratios of secondary ion density to total electron density. While not included here, Landau damping estimates can be further refined by considering the time evolution effects of localized electric fields on the velocity distribution function [86].

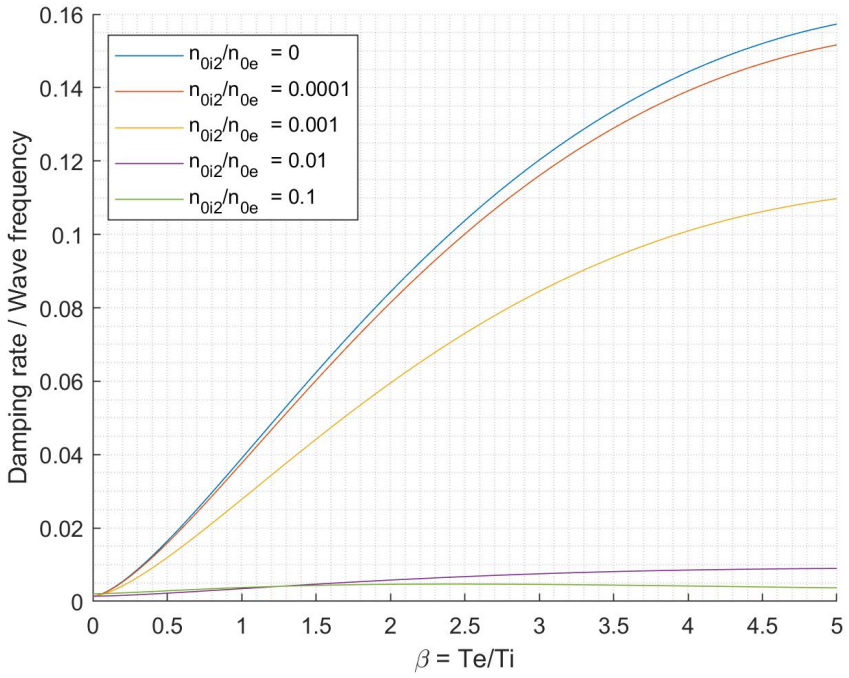

Figure 4.1: Normalized damping rates $\left|\frac{\gamma}{\omega_r}\right|$ vs $\beta = T_e/T_i$ for different ratios of secondary ion density to total electron density. The dominant ion species is O+ and the secondary ion species is H+.

4.4 Decay Time for Solitons

To calculate the propagation distance for damped solitons, which propagate along the debris velocity vector, we apply the known analytic expressions for the damping of soliton features. It can be shown analytically that in the presence of damping, soliton amplitude decays as $A(t) = A_0 e^{-2\gamma t/3}$, soliton speed decays as $V(t) = V_0 e^{-2\gamma t/3}$, and soliton width grows as $W(t) = W_0 e^{\gamma t/3}$ [2, 46]. To estimate the amount of time it would take for a soliton to decrease to half of its initial amplitude, we set $A(t) = A_0/2$:

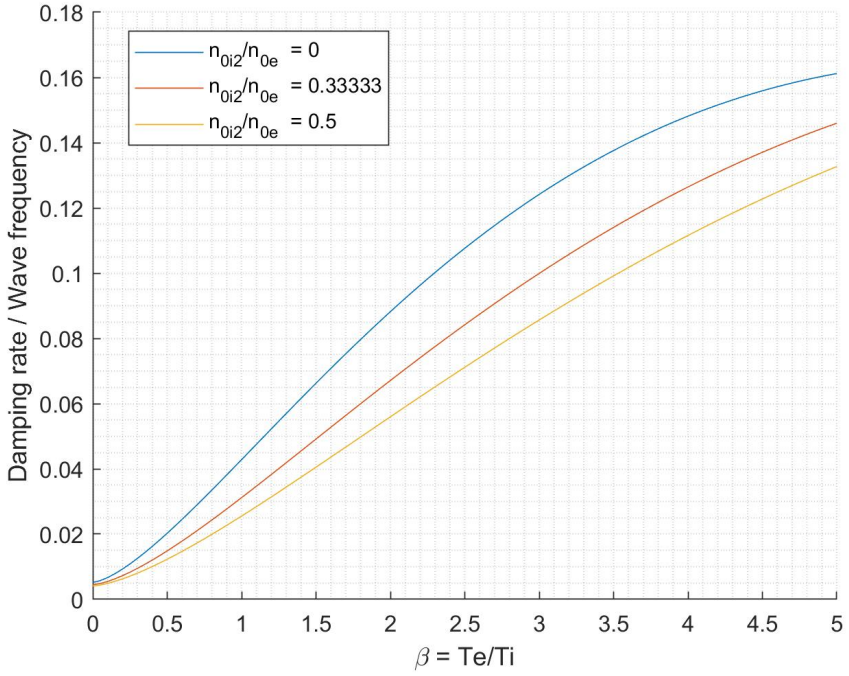

Figure 4.2: Normalized damping rates $\left|\frac{\gamma}{\omega_r}\right|$ vs $\beta = T_e/T_i$ for different ratios of secondary ion density to total electron density. The dominant ion species is H+ and the secondary ion species is He+.

$$A(t) = A_0/2 = A_0 e^{-2\gamma t/3} \tag{4.14}$$

$$t_{50\%} = \frac{3}{2}\frac{\ln(2)}{\gamma} \tag{4.15}$$

Similarly, the time for a soliton amplitude to decrease to 1% of its initial amplitude is:

$$t_{1\%} = \frac{3}{2}\frac{\ln(100)}{\gamma} \tag{4.16}$$

where $t_{50\%}$ and $t_{1\%}$ are in units of $1/\omega_{pi}$ in our normalized coordinate system.

To derive the propagation distance of a damped precursor soliton, we integrate the damped soliton speed over $t_{1\%}$:

$$x(t) = \int_0^{t_{\%1}} V_0 e^{-2\gamma t/3} dt \tag{4.17}$$

$$x_{t_{1\%}} = -\frac{3}{2}\frac{V_0}{\gamma}\left(e^{-2\gamma t_{1\%}/3} - 1\right) \tag{4.18}$$

where V_0 is the undamped soliton speed.

These decay times and propagation distances assume that solitons are propagating in an unforced system. We will numerically calculate the decay times for pinned and precursor solitons in the presence of a persistent force.

4.5 Application of Damping to Analytic Solutions

After validating our undamped fKdV equation in Chapter 3, and calculating the damping coefficients in Section 4.3, we applied the damping coefficient to the analytic solutions for forced and unforced solitons tested previously in Chapter 3, and evaluated their damping against the analytic expressions for soliton damping in Section 4.4. We observe that the analytic expressions for soliton damping apply to unforced solitons and precursor forced solitons, however, pinned solitons damp at a slower rate due to the presence of a persistent force.

Damping is applied to an unforced analytic solution from [1], which is a three

soliton system of the form in Eqn 4.19 [59], with $N = 3$.

$$U(x,0) = N(N+1)\text{sech}^2(x) \tag{4.19}$$

A forcing term is not introduced to create the solitons, but an initial wave creates the system, $U_0 = 12\text{sech}^2(x)$, with $\alpha = 6$ and $\beta = 1$. The three solitons advance ahead of the initial solution, and can be considered precursor solitons. As shown in Fig 4.3, the three solitons decay according to the analytical damping solutions. For $\gamma = -0.5$ and $t = 2.1$ TU, the analytical solution for damped soliton amplitude, A, when compared to its initial amplitude, A_0, is $A/A_0 = 0.4966$, from Eqn 4.14. For $\gamma = -0.25$, $A/A_0 = 0.7047$. The analytical solution for the damped soliton location is calculated from Eqn 4.18. Results for the analytical soliton amplitude and location are plotted along with the damped simulations.

Next, a pinned soliton solution was modeled from Wu [2], and the results are shown in Fig 4.4. The force is $f(x) = 2b_1\text{sech}(Kx)^2$, where $b_1 = -0.1250$ and $K = 0.6124$. The pinned soliton is initialized at U_0 with its solution of $U(x) = a\text{sech}(Kx)^2$, where $a = 0.5$. The estimated time to decay the soliton amplitude to 1% for a given $\gamma = -0.5$ is 13.8 TU, from Eqn 4.14. Fig 4.4 shows the pinned soliton after 13.8 TU in the presence of the persistent force, with and without the damping coefficient applied. Results show that the pinned forced soliton does not decay according to Eqn 4.16.

Thus, it has been shown that pinned forced solitons retain their amplitude longer than what is estimated from Eqn 4.14, due to the presence of a persistent

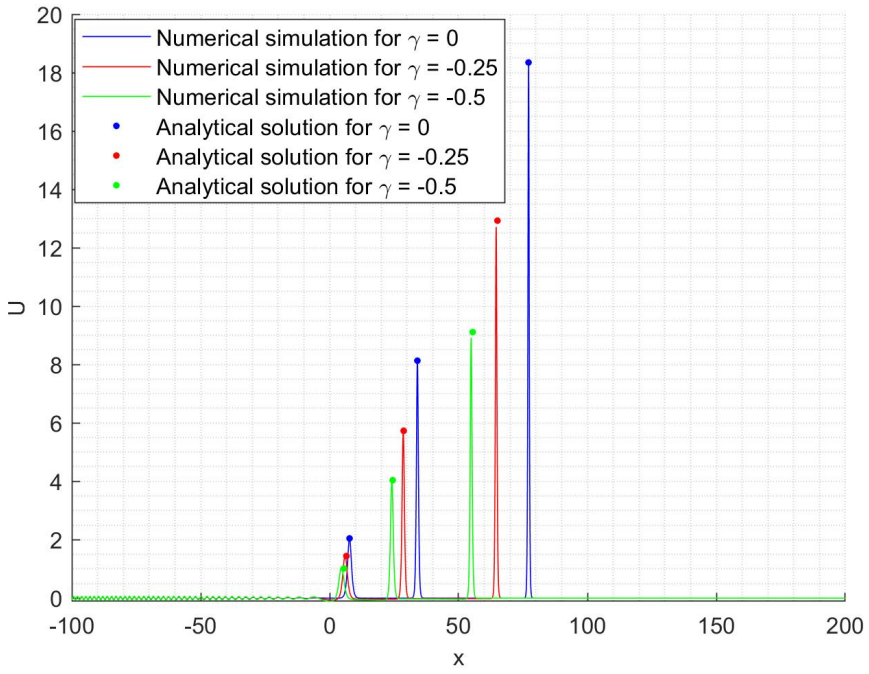

Figure 4.3: Reproduction of three soliton solution from [1]. Solitons are in the presence of a persistent force at 2.1 TU, with and without the damping coefficients applied and compared to analytical solutions.

force. However, the decay time for unforced solitons and precursor forced solitons can be accurately predicted from Eqn 4.14. In the case of precursor forced solitons, it is expected that a series of precursor solitons can be generated, and each soliton will decay according to its own lifetime. Additionally, it may be possible to generate precursor solitons from pinned solitons in a damped and forced system, as demonstrated in literature for other damped and forced systems [87]. Ghai *et al.* investigated shock structures evolving from an initial IASW in the presence of Landau damping, motivated by observations in the Earth's magnetosphere by the Geotail spacecraft [87]. We will assess whether pinned solitons from orbital debris

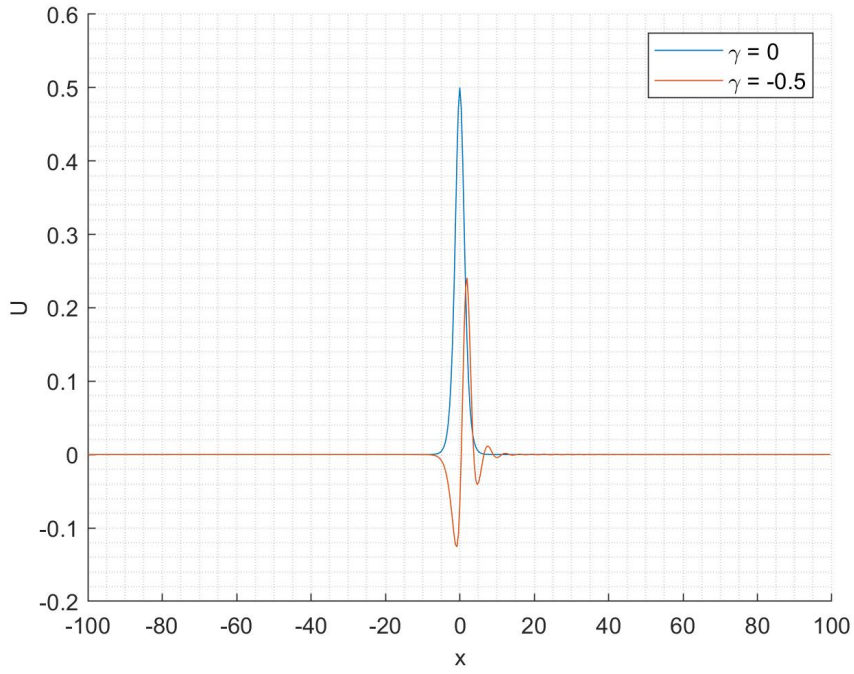

Figure 4.4: Reproduction of Wu [2] pinned soliton solution. The pinned soliton is in the presence of a persistent force is displayed at 13.8 TU, with and without the damping coefficient $\gamma = -0.5$ applied.

in Low LEO can create precursor solitons in the presence of Landau damping in 4.6.

4.6 Damped Solitons in Nominal Plasma Conditions

After evaluating our pseudospectral method for damped precursor solitons using Eqn 4.2, we downloaded a global ionospheric model in order to estimate the propagation distances for damped precursor solitons in LEO. In Chapter 3, plasma properties in LEO were downloaded from the International Reference Ionosphere (IRI) data [17] to predict the altitudes, latitudes, and local times where precursor solitons are generated for a variety of debris sizes. From the IRI data, the normalized

damping rate $\frac{\gamma}{\omega_r}$ in Eqn 4.13 can be estimated. The primary and secondary ion masses and temperature, as well as the electron density and temperature, are used to calculate β, N_0^{12}, δ, and ω_{pi}. For all figures in this section, the x domain is in units of the Debye length, and time is units of Debye length divided by the ion acoustic velocity. One time unit (TU) is λ_D/V_{ia}.

To apply the damping rate in our normalized system, we multiply the Eqn 4.13 by the wave frequency, ω_r, and divide by the ion plasma frequency, ω_{pi}, so that the damping coefficient applied to the system is γ/ω_{pi}. For the case of precursor solitons, the wavelength is the distance between subsequent solitons. The wave frequency is the inverse of the time between subsequent solitons, t_{12}, which depends on the force amplitude and speed. In our normalized system, where $\omega_{pi} = V_{ia}/\lambda_D$, the normalized wave frequency for precursor solitons is:

$$\omega_{r,n} = \frac{\omega_{pi}}{t_{12}} \tag{4.20}$$

4.6.1 Pinned Solitons

Damped pinned solitons were simulated using the IRI data for January 1, 2000, at 6pm UTC, 500 km altitude, 0° latitude. In this region, oxygen is the dominant ion and the orbital debris travels much faster than the velocity threshold where precursor solitons are generated. Debris sizes ranging from 1mm-1cm were tested for a circular orbit. Additional damping coefficients were tested for each simulation, including the estimated $\gamma/2$, γ, and 2γ. For all simulations of the damped, pinned

soliton, the damping did not lead to precursor solitons.

Intuitively, one can predict that precursor solitons due to orbital debris will not be produced from pinned solitons with the additional presence of Landau damping. Pinned solitons are created when the steepening and dissipation forces were balanced. In order to generate precursor solitons from a pinned soliton, the steepening forces will need be greater than the dispersion and dissipation forces. However, with the addition of Landau damping, the dissipation and dispersion forces are now greater than the steepening force.

Through all of the damped pinned solitons simulations, the pinned solitons do not experience significant damping due to the presence of the persistent debris force at the soliton location, with an average difference in amplitude between the undamped and damped pinned soliton of 0.7%. Thus, it is expected that pinned solitons will continue to propagate until the debris enters a region where pinned solitons cannot be created.

Small scale plasma irregularities are frequently studied with ground based radar [60], ionosondes [61], and space-based sensors [62, 63]. The amplitude of the density waves that can be detected is as small as 0.001% of the unperturbed density [63]. Damped pinned solitons from sub-centimeter orbital debris are above the detection threshold, with amplitudes between $1.04 - 1.14$ times the unperturbed background density for debris sizes between 1mm-1cm radius. The spatial resolution of these sensors will need to also be considered in the future design of soliton detection methods.

4.6.2 Precursor Solitons

Fig 4.5 shows an example of a precursor soliton due to 1 cm radius orbital debris in LEO, in a circular orbit at 2000 km altitude. Plasma parameters are from IRI data [17] at 0° longitude, 6pm UTC on July 1, 2000. The Debye length is $\lambda_D = 3.63$ cm, and the ion plasma frequency is $\omega_{pi} = 1.46\text{x}10^5\ s^{-1}$. The soliton speed is $V_0 = 1.38V_{ia}$, and the time between solitons is $t_{12} = 45.7$ TU. The wave frequency is $\omega_r = 3.7\text{x}10^3\ s^{-1}$. The estimated normalized damping coefficient is $\gamma/\omega_r = -0.039$, with $\gamma/\omega_{pi} = -9.9\text{x}10^{-4}$, and $t_{1\%} = 6.9\text{x}10^3$ TU, for a propagation distance $x_{t_{1\%}} = 405$ m. Results are shown at 500 TU for zero damping in blue and $\gamma \neq 0$ in red. As displayed, for precursor solitons advancing ahead of the force, soliton amplitude decays as $A(t) = A_0 e^{-2\gamma t/3}$ and soliton width grows as $W(t) = W_0 e^{\gamma t/3}$ [2, 46]. The difference between each of the seven precursor solitons and the damped analytical solution was calculated. The average difference between the analytical and the numerical predictions of for the damped soliton amplitude is 0.025, which is 2% of the undamped soliton amplitude. The hydrogen ion density from the IRI dataset is $1.23\text{x}10^4$ cm^{-3}, so the density uncertainty corresponds to 531 cm^{-3}. The average difference between the analytical soliton and the numerical simulation for the damped soliton location is 0.013. In this example, the location uncertainty corresponds to 0.05 cm.

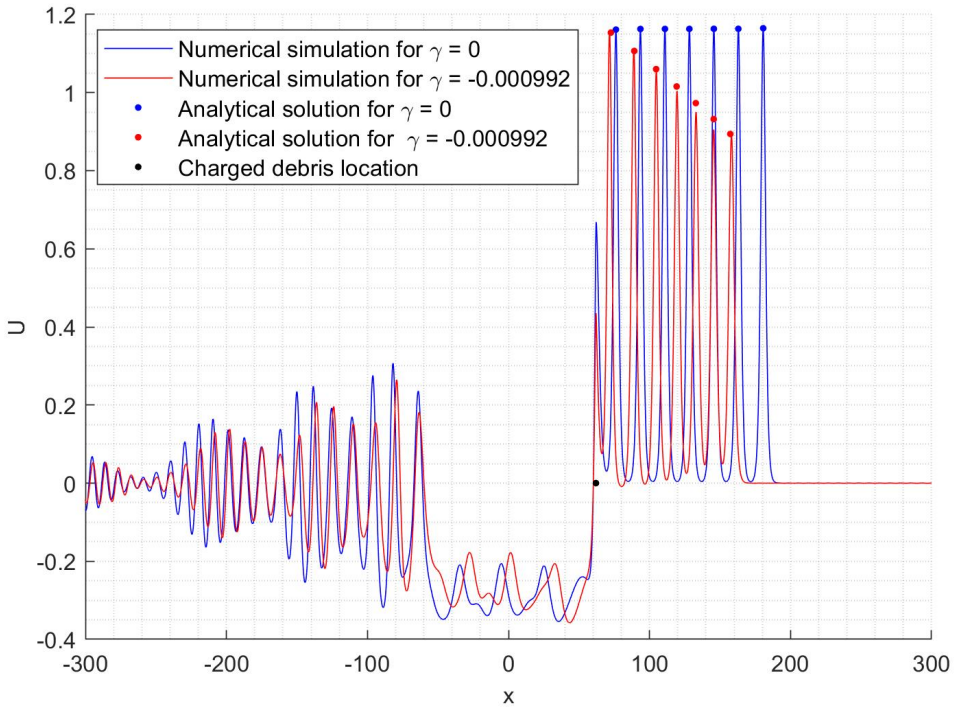

Figure 4.5: Precursor soliton due to 1 cm radius orbital debris in LEO, in a circular orbit at 2000 km altitude. Results are shown at 500 TU for zero damping in blue and γ in red.

4.7 Global Model of Damped Precursor Solitons

In order to calculate typical propagation distances for orbital debris precursor solitons in LEO, we applied the calculated damping coefficients from the global ionospheric model in 4.6 to a variety of debris sizes and velocities. Precursor generation regions were identified using the IRI ionospheric data, as well as the supercritical and subcritical velocity limits from Section 4.1. The resulting orbital debris velocities were then filtered to identify the velocities for which real orbits could exist, with an eccentricity less than 1 and periapsis greater than the radius of the Earth [34]. Next, we calculated the minimum, median, and maximum propagation distance for

the damped precursor solitons in order to evaluate the detectability of the solitons with existing sensor technology. Since the amplitude of the density waves that can be detected is as small as 0.001% of the unperturbed density [63], we propagate the plasma waves to $x_{t_{1\%}}$ using Eqn 4.18, the distance where the amplitude decays to 1% of the initial amplitude.

As shown in Eqn 4.18, damped soliton propagation distance depends on the soliton speed and amplitude. The normalized damping coefficient, as shown in Eqn 4.13, depends on the soliton generation interval or wave frequency, as well as the mass, temperature, and density of the ion species in the plasma. It has been shown that as the debris size decreases, the time required to generate a precursor soliton becomes exponentially longer and the transcritical velocity range is smaller. Also, as the debris size decreases, the soliton speed and amplitude decrease, while the width increases [34]. Calculating the damped soliton propagation distance requires prior knowledge of the undamped soliton. Thus, the damped soliton propagation distance in Eqn 4.18 requires the undamped soliton speed and amplitude, and the damping coefficient Eqn 4.13 requires the soliton wave frequency.

To efficiently estimate soliton propagation distances in the global model, we created dimensionless 3D models for undamped soliton speed, amplitude, width, and frequency as a function of debris size and velocity. Simulations were conducted for 21 dimensionless debris sizes ranging from a/λ_D = 3.623 - 0.072 and 16 orbital debris velocities, expressed in terms of the supercritical velocity of that debris size, ranging from $V = 0.48V_{sup}$ to $1V_{sup}$. Note that each dimensionless debris size has its own supercritical velocity. The soliton properties were modeled with biharmonic

interpolation [34].

Plasma conditions were downloaded from the International Reference Ionosphere (IRI) model [17] in order to identify regions where precursor solitons could be generated in Chapter 3. IRI data is limited to 2000 km altitude. We downloaded data collected from 200 km - 2000 km altitude at 100 km increments, and $-90°$ to $90°$ latitude at $10°$ increments, on two dates to represent plasma conditions during summer and winter: July 1, 2000, and January 1, 2000. For each date, we downloaded data at $0°$ longitude at eight difference local times: 12am/pm, 3am/pm, 6am/pm, and 9am/pm. We created a grid of plasma parameters in altitude, latitude, and time. There are 10,952 grid points for each date, and 296 grid points per altitude per date.

Using the dimensionless 3D models for soliton generation interval and soliton speed, we calculated the normalized soliton wave frequency, which is required for Eqn 4.13. Along with the plasma conditions provided by the IRI model at each grid point, we calculated the damping coefficient from Eqn 4.13. Finally, with the dimensionless 3D model for soliton speed as a function of debris size and debris velocity, we calculated the propagation distance for each soliton using Eqn 4.18.

The resulting propagation distances shown in Fig 4.6 for a 0.5 cm radius debris. In general, the location of the precursor generation region is found in the region of dominant H+ ions, since the ion acoustic velocity will be comparable to the orbital velocity. Since the transcritical velocity threshold is defined by the dimensionless debris size, the precursor generation region will be defined by ratio of debris size to the Debye length. Finally, the ratio of the electron temperature to

the ion temperature will inform the damping coefficient according to Eqn 4.13.

For all of the IRI simulation data, the minimum, median, and maximum precursor soliton propagation distances in the presence of Landau damping, $x_{(t1\%)}$, were identified as a function of debris size, as shown in Fig 4.7. For debris radius 0.5 mm, the minimum precursor propagation distance is 6 km, the median is 10 km, and the maximum is 49 km. The maximum propagation distances for each radii occurred in small regions of the IRI datasets where the plasma density was much lower than the surrounding regions.

In order to assess feasibility of detecting damped precursor solitons, the likelihood of precursor solitons to be created and propagate over 1 km, 5 km, and 10 km was also calculated as a function of altitude. Each altitude, latitude, date and local time represents one grid point that was queried as a function of debris size. For each grid point and debris size, a range of velocities between the transcritical limits were considered, and the number of grid points for which valid orbits are produced were counted. If a grid point produced a precursor soliton for one or more velocities, it was counted once in the total number of grid points for which precursor solitons are produced. For all of the IRI simulation data results, Fig 4.8 shows the percentage of grid points for a given altitude where precursor solitons are created and propagate over 1 km, 5 km, and 10 km as a function of debris size according to Eqn 4.18, for July 1, 2000. For 0.5 mm radius debris, 20% of the grid points with 2000 km altitude and all latitudes produce precursor solitons that propagate over 5 km. When considering the equator only, results show that 50% of grid points along the equator at 2000 km altitude produce precursors for 0.5 mm radius debris that

propagate over 5 km.

4.8 Global Variations in Landau Damping

Landau damping, as calculated in Section 4.3, depends on the relative temperature between the electrons and ions. It has been shown that the temperature difference between electrons and ions in the ionosphere depends on the season and time of day, with $T_e - T_i \approx 1300K, 900K$ at 500km altitude in the summer during day and night, respectively, and $T_e - T_i \approx 1000K, 400K$ at 500km altitude in the winter during day and night, respectively [88].

For the IRI data [17] used in this study, variations in β and $|\gamma/\omega_r|$ are displayed in Fig 4.9 - Fig 4.11. For the mid-latitude and high altitude regions where precursor solitons can be generated, on average β is lower during the summer when compared to winter, and lower during the day when compared to night. Therefore, $|\gamma/\omega_r|$ is also lower during the summer when compared to winter, and lower during the day when compared to night, resulting in a lower damping coefficient and larger propagation distances. Typically, over all sub-centimeter debris sizes, solitons propagate 1-2km farther in the summer when compared to winter, and day when compared to night.

4.9 Influence of Plasma Variations on Propagation Distance

The steepening and dispersion coefficients of the KdV equation, α and β, are defined by the kappa-distribution of the Earth's plasmasphere, and will remain

constant within the plasmasphere. With the addition of the damping coefficient, γ, we will assess whether the damping coefficient and/or forcing term will change over a precursor soliton's propagation distance. If so, it will be necessary to use the variable KdV equation [89], which accounts for changing coefficients.

Using the propagation distance calculated using Eqn 4.18 for each queried altitude/latitude and radius in the global simulation results displayed in Section 4.7, we calculated the variation in plasma properties, in increments of one Debye length, over the maximum propagation distance. Since the forcing term is normalized by the Debye length, a change in the Debye length would change the width of the normalized force. Additionally, since $\beta = T_e/T_i$, n_e, and n_i drive the damping coefficient (γ), a change in these plasma properties would change the damping coefficient. With the data downloaded from IRI, we are able to model variations in plasma parameters in radial and latitudinal propagation directions. However, longitudinal variation cannot be modeled since we have downloaded data at only eight local times. Future efforts could conduct the longitudinal variation measurements with a similar methodology.

For each queried altitude/latitude and maximum propagation distance, $x_{t_{1\%}}$ from Eqn 4.18, incremental changes in the plasma properties were calculated in the radial and latitudinal directions, both inward/outward for radial propagation, and northward/southward for latitudinal propagation. For radial propagation, the latitude remains constant, $\theta_{lat,1} = \theta_{lat,0}$, and the altitude changes according to Eqn 4.21-4.22. For latitudinal propagation, the altitude remains constant, and the latitude changes according to Eqn 4.23-4.24. The geometry for latitudinal propagation is an

isosceles triangle with base $x_{t_{1\%}}$ and leg r. Due to limitations in altitude/latitude from the IRI data, propagation was bounded by altitude $r = [200, 2000]$ km.

$$r_{1+} = r_0 + x_{t_{1\%}} \tag{4.21}$$

$$r_{1-} = r_0 - x_{t_{1\%}} \tag{4.22}$$

$$\theta_{lat,1+} = \theta_{lat,0} + 2\text{arcsin}\left(\frac{x_{t_{1\%}}}{2r_0}\right) \tag{4.23}$$

$$\theta_{lat,1-} = \theta_{lat,0} - 2\text{arcsin}\left(\frac{x_{t_{1\%}}}{2r_0}\right) \tag{4.24}$$

We calculate the percentage of propagating solitons that experience more than a 1% variation in plasma parameters. For each radius, altitude, latitude, and local time queried, a maximum soliton propagation distance has been calculated for each grid point. The variation in plasma parameters across that distance was observed for all grid points where precursors are produced. The percentage of grid points where precursors are produced, and propagate radially across a distance where the Debye length changes by more than 1%, is displayed as a function of debris radius in Fig 4.12. For latitudinal propagation, no cases were found where the Debye length changed more than 1%. As shown, fewer than 1% of the predicted solitons experience significant variations in the plasma environment. Thus, the variable KdV is not required to accurately model the precursor soliton propagation.

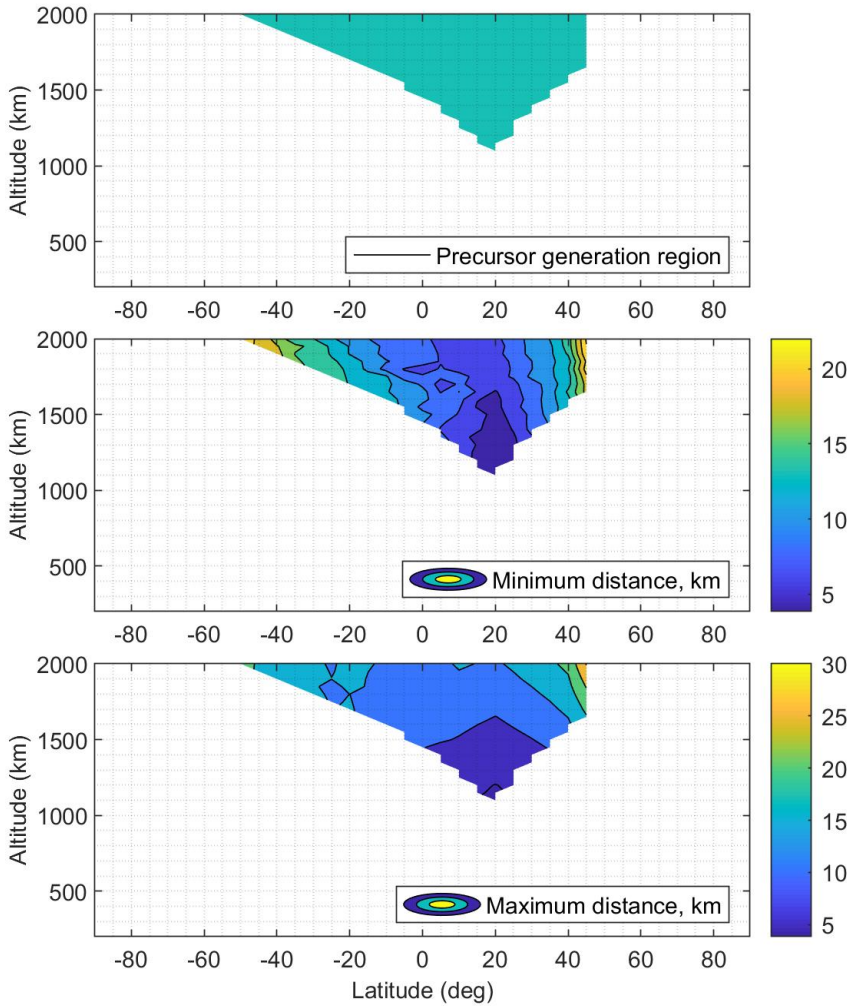

Figure 4.6: Precursor soliton generation region and propagation distance, $x_{t_{1\%}}$, for a 0.5 cm radius debris on January 1, 2000, at 6am UTC and 0° longitude.

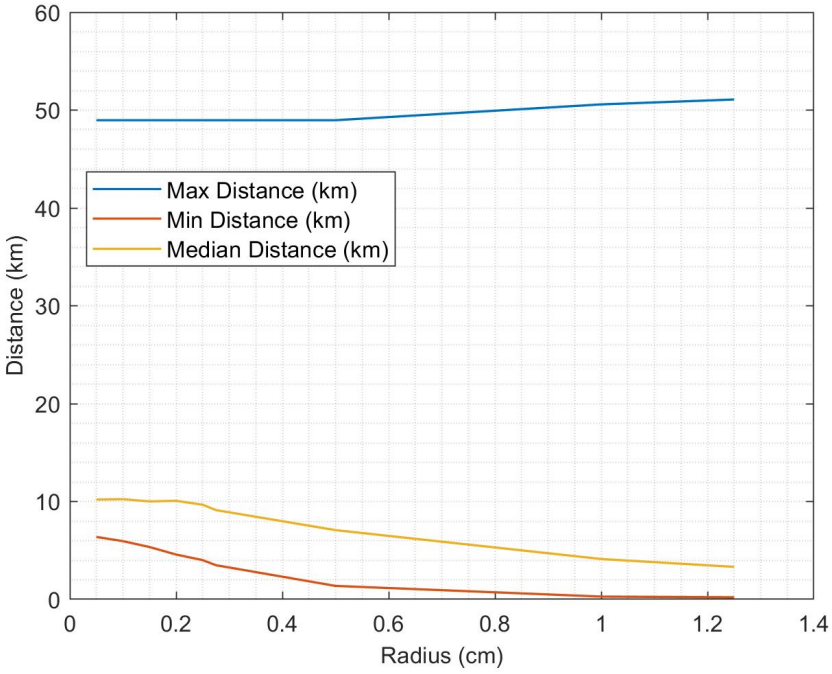

Figure 4.7: Minimum, median, and maximum soliton propagation distance by orbital debris size generated across all plasma environments in the IRI model data detailed in Section 4.7.

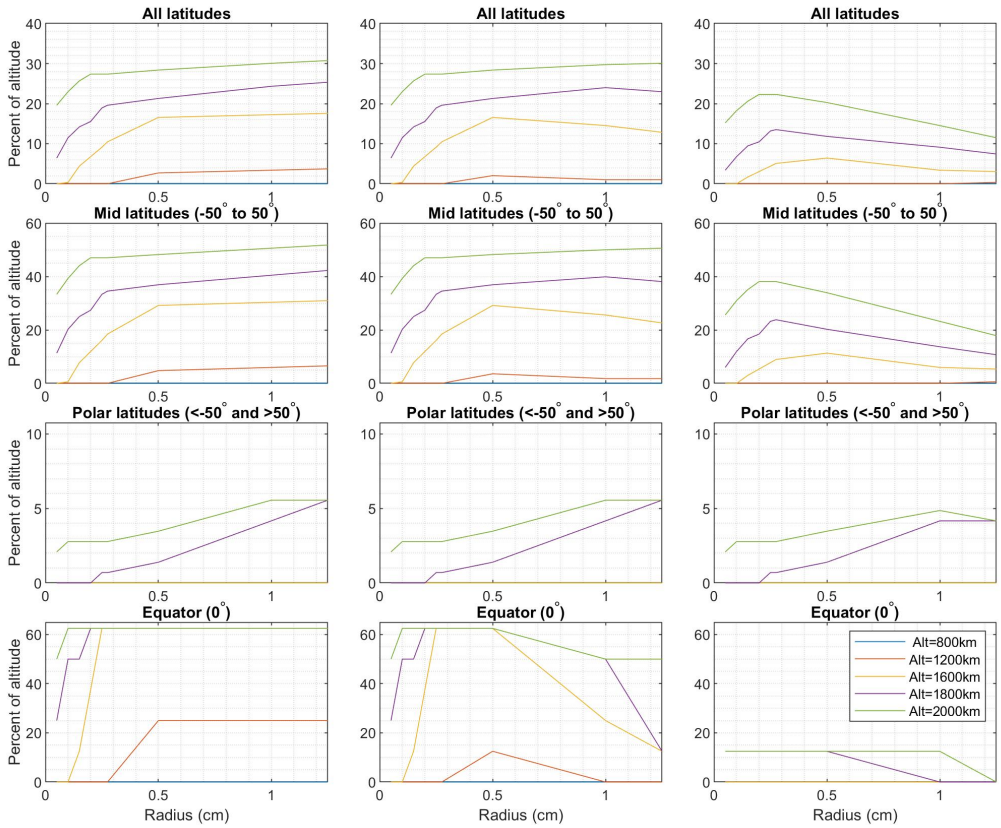

Figure 4.8: For July 1, 2000, the percentage of grid points for a given altitude in LEO where the precursor solitons propagation distance is greater than 1 km (left), 5 km (center), and 10 km (right), as a function of debris size.

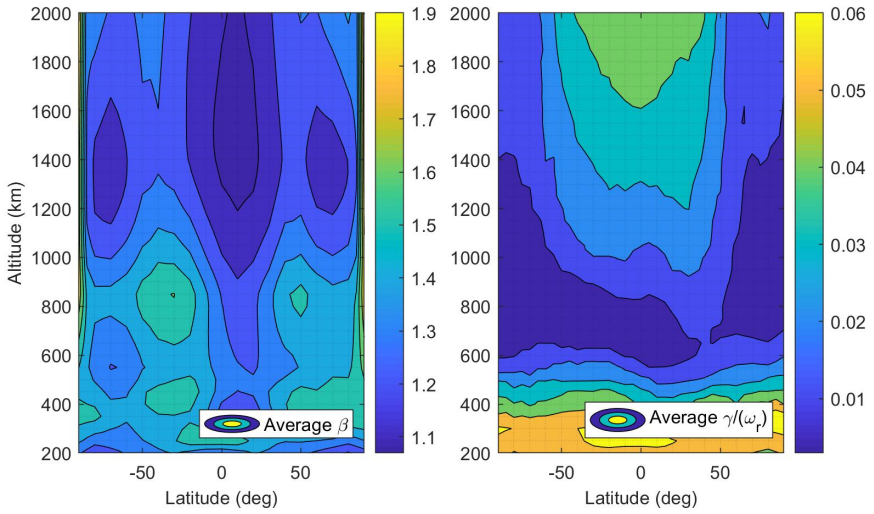

Figure 4.9: Average β and $|\gamma/\omega_r|$ for all IRI data across different local times, as a function of altitude and latitude.

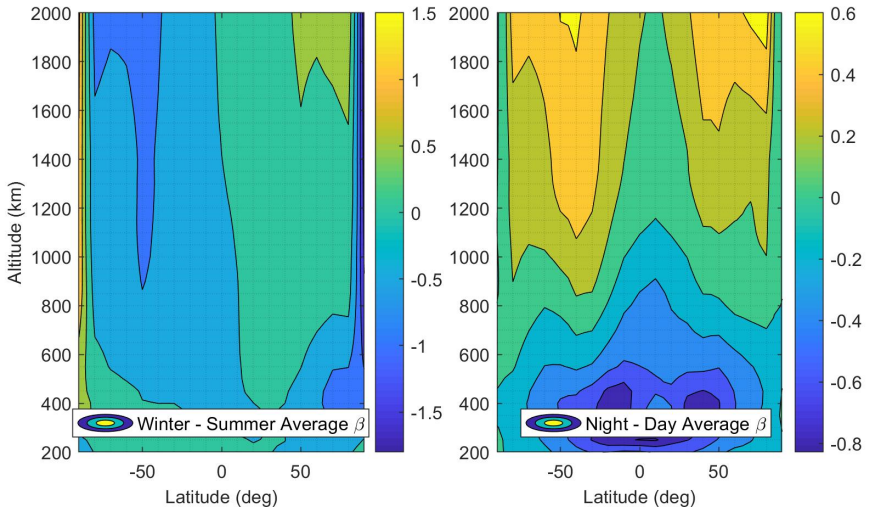

Figure 4.10: Difference in β at each grid point for Average Winter - Average Summer (left) and Average Night - Average Day (right).

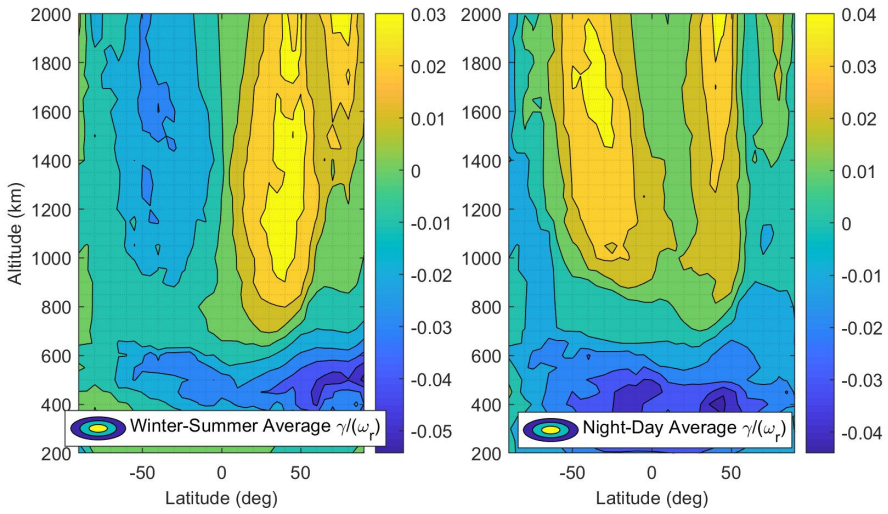

Figure 4.11: Difference in $|\gamma/\omega_r|$ at each grid point for Average Winter - Average Summer (left) and Average Night - Average Day (right).

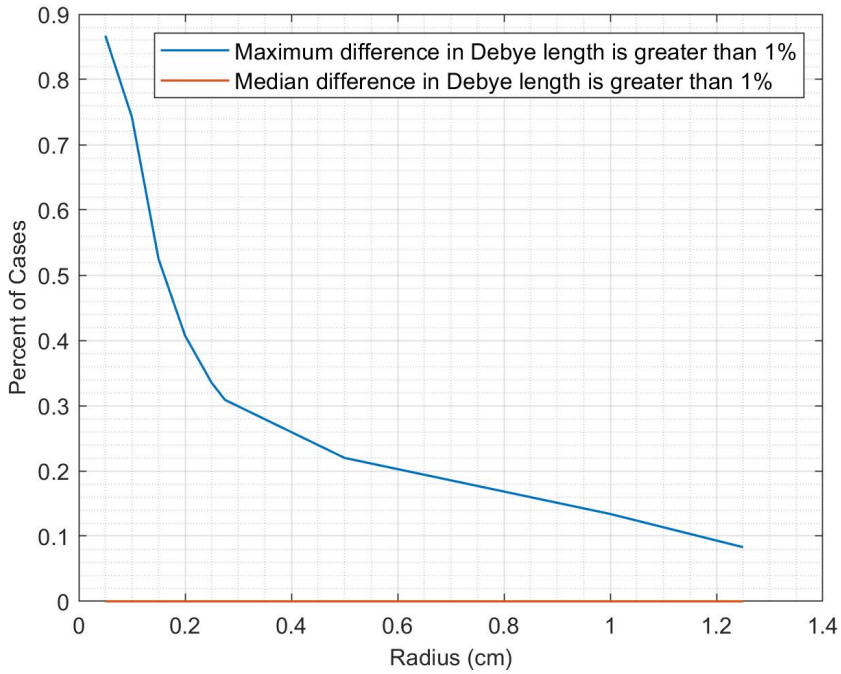

Figure 4.12: As a function of debris size, the percent of grid points where the median and maximum change in Debye length is greater than 1%, assuming radial propagation.

4.10 Conclusions and Future Work

We derived the propagation distance of orbital debris precursor solitons in the presence of Landau damping. The median propagation distance for these solitons is 10 km for 0.5 mm radius debris, and 6 km for 0.5 cm radius debris. Propagation distances are influenced by seasonal and diurnal effects, with longer propagation distances during the summer when compared to winter, and day when compared to night. We have shown that the plasma properties do not change more than 1% over the maximum propagation distances, thus the KdV coefficients will remain constant and the variable KdV equation is not needed for accurate modeling of these solitons. These propagation distances are necessary to assess the detectability of precursor solitons via satellite or ground observations, the time required to map detectable debris, and the number of sensors needed for mapping in a given mission window.

Chapter 5: Simulating Damped Solitons from Orbital Debris in Three Spatial Dimensions

Chapter 3 demonstrates that one dimensional simulations are sufficient to model the orbital debris solitons, which propagate along the debris velocity vector. However, in order to fully understand the soliton signatures in a 3D spatial environment, it is necessary to extend the dfKdV model to three spatial dimensions. In Chapter 5, as submitted for publication, we will apply the Damped Forced Kadomtsev-Petviashvili Equation (dfKP), which is a natural extension for waves described by the dfKdV equation.

The content of this chapter has been submitted for publication as Truitt and Hartzell, "3D Kadomtsev-Petviashvili Damped Forced Ion Acoustic Solitary Waves from Orbital Debris," Journal of Spacecraft and Rockets, 2020.

5.1 Damped Forced Kadomtsev-Petviashvili Equation

The Kadomtsev-Petviashvili (KP) equation was first written in 1970 Boris Kadomtsev and Vladimir Petviashvili as a natural two-dimensional generalization of the one-dimensional KdV equation, which was derived by Korteweg and De Vries in 1895 [21]. The KP equation intuitively describes the stability of 1D solitons against

transverse perturbations [90], and requires that the wave propagation direction is in the X direction, with only minimal variations of solutions in the Y direction. As a result, oscillations in the Y direction tend to be of small deviation [91]. The KP equation has been used to describe the behavior of ion acoustic waves in space plasma [78, 92], with analytic solutions studied in [76, 90]. To understand the application of the Damped Forced KP equation to orbital debris, we start with the one dimensional Damped Forced KdV equation.

The Damped Forced KdV equation in 5.1 was derived from the plasma fluid equations for ion acoustic solitary waves, U, created by the presence of a charged orbital debris force, f, [34]:

$$\frac{\partial U}{\partial \tau} + \alpha U \frac{\partial U}{\partial \xi} + \beta \frac{\partial^3 U}{\partial \xi^3} + \gamma U = \frac{1}{2} \frac{\partial f}{\partial \xi} \tag{5.1}$$

where α, β, and γ are the steepening, dispersion, and damping coefficients, respectively.

The system is normalized so that the soliton wave is the perturbed ion density normalized by the unperturbed ion density, $U = (n - n_0)/n_0$. The spatial and temporal variables, ξ and τ, are the stretched coordinates of the initial boundary-value problem [34]. The ξ domain is in units of the Debye length, and the time domain τ is in units of plasma frequency, ω_{pi} (Debye length, λ_D, divided by the ion acoustic velocity, V_{ia}). Solitons are wave solutions to this equation when the steepening and dispersion forces are balanced.

The one dimensional Damped Forced KdV equation with Landau damping

extends to 3D as the Damped Forced Kadomtsev-Petviashvili equation [93]:

$$\frac{\partial}{\partial \xi}\left(\frac{\partial U}{\partial \tau}+\alpha U\frac{\partial U}{\partial \xi}+\beta\frac{\partial^3 U}{\partial \xi^3}+\gamma U\right)+\mu\left(\frac{\partial^2 U}{\partial \eta^2}+\frac{\partial^2 U}{\partial \zeta^2}\right)=\frac{1}{2}\frac{\partial^2 f}{\partial \xi^2} \tag{5.2}$$

where μ is the dispersion coefficient for all transverse directions, and η and ζ are the stretched coordinates in the Y and Z directions, respectively.

The steepening and dispersion coefficients are dependent on the plasma velocity distribution. Earth's space plasma is best modeled as a kappa ($\kappa = 100$) distribution instead of a Maxwellian model due to a suprathermal tail of high energy electrons [49, 50]. The coefficients are derived as $\alpha = 1.0051$, and $\beta = 0.4925$, according to Eqn 5.3-5.5 [34, 45, 46], where n_{0i} and n_{0e} are the unperturbed ion and electron densities, and z_i is the ion charge state.

$$\alpha = \frac{3a_\kappa(1/\rho^{1/2}) - 2b_\kappa(\rho^{1/2}/z_i)}{2a_\kappa^{3/2}} \tag{5.3}$$

$$\beta = \frac{\rho^{1/2}}{2a_\kappa^{3/2}} \tag{5.4}$$

where

$$a_\kappa = \frac{2\kappa-1}{2\kappa-3} \qquad b_\kappa = \frac{4\kappa^2-1}{2(2\kappa-3)^2} \qquad \rho = \frac{z_i^2 n_{0i}}{n_{0e}} \tag{5.5}$$

In Chapter 4, we identified that Landau damping was the dominant damping

process, and applied Arshad *et al.*'s model for Landau damping of ion acoustic waves due to electrons and ions in a kappa-distributed multi-ion plasma. In the long wavelength limit and assuming the same ion temperature, $T_{\alpha_1} = T_{\alpha_2} = T_i$, the damping rate normalized by the soliton wave frequency, ω_r, is given as [85]:

$$\begin{aligned}\frac{\gamma}{\omega_r} = -\sqrt{\frac{\pi}{8}}\frac{\Gamma(\kappa+1)}{\Gamma(\kappa-1/2)}\frac{\sqrt{N_0^{12}}}{2^{3/2}(\kappa-1/2)^{3/2}}\Bigg[\sqrt{\frac{m_e}{m_{i1}}} \\ +\Big(\frac{n_{0i1}}{n_{0e}}\Big)\beta^{3/2}\Big[1+\frac{\beta N_0^{12}}{2(2\kappa-1)}+\frac{3\delta}{(2\kappa-3)N_0^{12}}\Big]^{-\kappa-1} \\ +\Big(\frac{n_{0i2}}{n_{0e}}\Big)\beta^{3/2}\sqrt{\frac{m_{i2}}{m_{i1}}}\Big[1+\frac{\beta N_0^{12}}{2(2\kappa-1)}+\frac{3\delta}{(2\kappa-3)N_0^{12}}\frac{m_{i2}}{m_{i1}}\Big]^{-\kappa-1}\Bigg]\end{aligned} \tag{5.6}$$

where $\beta = T_e/T_i$ is the ratio of electron to ion temperature, $N_0^{12} = \left[\frac{n_{0i1}}{n_{0e}} + \frac{n_{0i2}}{n_{0e}}\frac{m_{i1}}{m_{i2}}\right]$ and $\delta = \left[\frac{n_{0i1}}{n_{0e}} + \frac{n_{0i2}}{n_{0e}}(\frac{m_{i1}}{m_{i2}})^2\right]$ are relationships between the dominant ion density, n_{0i1}, secondary ion density, n_{0i2}, electron density, n_{0e}, dominant ion mass, m_{i1}, and secondary ion mass, m_{i2}. To apply the damping coefficient to the normalized system, we multiply Eqn 5.6 by the soliton wave frequency, ω_r, and divide by the plasma frequency, ω_{pi}. While not included here, Landau damping estimates can be further refined by considering the time evolution effects of localized electric fields on the velocity distribution function [86].

The surface potential, Φ_s, of orbital debris with radius, a, will create a perturbation in the surrounding plasma density. The plasma potential, Φ_p, at a distance r away from the debris is calculated as $\Phi_p = \Phi_s \exp(-r/\lambda_D)$. The debris force defined by the surface potential of the debris, a negative charge which will attract

an increased number of ions. The debris surface potential force is described as a Gaussian [57] in Eqn 5.7 with an amplitude equal to plasma potential normalized by the by the electron temperature, $\Phi_{p,n} = \Phi_p(e/k_B T_e)$ [34]:

$$f(\xi, \tau) = \Phi_{p,n} \exp\Big[- \Big(\frac{\xi - V_d \tau}{G} \Big)^2 \Big] \tag{5.7}$$

where V_d is the debris speed in units of V_{ia}, λ_D is the Debye length, and $G = a/\lambda_D$.

The creation of solitons produced in a system described by Eqn 5.1 depends on the relative speed of the force with respect to the fluid medium. In our case, it depends on the relative speed of the debris with respect to the plasma ions. When the relative speed falls above the supercritical limit, pinned solitons will be produced, which travel with the debris at the debris speed. When the relative speed falls below the subcritical limit, no solitons will be produced. When the relative speed is between the subcritical and supercritical limits, precursor solitons are produced, which advance ahead of the debris along the debris velocity vector. The velocity of the debris at the supercritical and subcritical limit, in units of the ion acoustic velocity, V_{ia}, is defined as [44]:

$$V_{sup} = 1 + \Big(\frac{3(\alpha/2)^2 A^2}{16\beta} \Big)^{1/3} \tag{5.8}$$

$$V_{sub} = 1 - \Big(\frac{3(\alpha/2)^2 A^2}{4\beta} \Big)^{1/3} \tag{5.9}$$

where the area of the Gaussian force is [57]:

$$A = |\Phi_{p,n}|\sqrt{\pi}G \tag{5.10}$$

The coefficient for dispersion in the transverse directions, μ, is dependent on the wave phase speed, V_p, due to the kappa distributed electrons [46, 78, 79]:

$$\mu = \frac{V_p}{2} = \frac{1}{2\sqrt{K}} = 0.4975 \tag{5.11}$$

where $K = \frac{2\kappa-1}{2\kappa-3} = 1.01$.

In the orbital debris system, the debris will propagate along ξ, with no velocity along η or ζ. Understanding that the soliton signatures with be identical in all transverse directions, and in an effort to reduce numerical computation times, we simplify Eqn 5.2 to two dimensions:

$$\frac{\partial}{\partial\xi}\left(\frac{\partial U}{\partial\tau} + \alpha U\frac{\partial U}{\partial\xi} + \beta\frac{\partial^3 U}{\partial\xi^3} + \gamma U\right) + \mu\left(\frac{\partial^2 U}{\partial\eta^2}\right) = \frac{1}{2}\frac{\partial^2 f}{\partial\xi^2} \tag{5.12}$$

The 2D forcing function then becomes:

$$f(\xi,\eta,\tau) = \Phi_{p,n}\exp\Big[-\Big(\frac{\xi - V_{d_x}\tau}{a_x/\lambda_D}\Big)^2 - \Big(\frac{\eta - V_{d_y}\tau}{a_y/\lambda_D}\Big)^2\Big] \tag{5.13}$$

where a_x and V_{d_x} are the debris radius and speed in the ξ direction, a_y and $V_{d_y} = 0$ are the debris radius and speed in the η direction. We will apply 5.12 to orbital debris solitons in order to characterize transverse perturbations.

5.2 Numerical Methods

Throughout literature, it is recognized that numerical challenges exist for solving the KP equation. The time step size for explicit schemes have a strict stability limit, and implicit schemes often do not converge due to the third spatial derivative. A common solution is to integrate the KP equation with respect to ξ and employ the Fourier multiplier, $\partial_x^{-1} = -\frac{i}{k}$ [94]:

$$\left(\frac{\partial U}{\partial \tau} + \alpha U \frac{\partial U}{\partial \xi} + \beta \frac{\partial^3 U}{\partial \xi^3} + \gamma U\right) + \mu \partial_x^{-1}\left(\frac{\partial^2 U}{\partial \eta^2}\right) = \frac{1}{2}\frac{\partial f}{\partial \xi} \tag{5.14}$$

With this approach, we are able to use the numerical scheme applied to the KdV in [34, 80], and modify it to introduce the second derivative in the η direction. For the KdV equation, the Chan & Kerkhoven (CK) [27] pseudospectral scheme was used to simulate the solitons, where the finite difference approximation is applied to the time derivative and a leapfrog method is used for the spatial derivatives. The method was written in Matlab and applied to known analytic solutions to the fKdV in Chapter 3, and analytic solutions to soliton damping in Chapter 4.

The ξ spatial domain $[-L, L]$ is discretized into N equidistant points and is normalized to $[0, 2\pi]$. Now, $\Delta\xi = \frac{2\pi}{N}$ and $\xi = s(x + L)$, where $s = \frac{\pi}{L}$ so that the solution is periodic from 0-2π.

Since the soliton waves are propagating along the ξ direction, we assume that they are non-periodic along η and apply the finite difference method for the spatial derivative in this direction [95]. In Eqn 5.15, i is in the index in the ξ direction and

j is the index in the η direction. Superscripts for U are in the temporal domain. Thus, $n+1 = \tau + \Delta\tau$ and $n-1 = \tau - \Delta\tau$.

$$\frac{\partial^2 U_{i,j}^n}{\partial \eta^2} = \frac{U_{i,j+1}^n - 2U_{i,j}^n + U_{i,j-1}^n}{\Delta\eta^2} \tag{5.15}$$

The numerical solution for the Damped Forced KP equation becomes:

$$\begin{aligned} U^{n+1} = \mathscr{F}^{-1}\Bigg[\frac{1}{1-\Delta t\beta i s^3 k^3}((1+\Delta t\beta i s^3 k^3)\mathscr{F}(U^{n-1}) - \Delta t\alpha i s k \mathscr{F}(U^n)^2 \\ -\Delta t\gamma \mathscr{F}(U^n) + 2\Delta t\mu\left(\frac{i}{k}\right)\mathscr{F}\left(\frac{\partial^2 U^n}{\partial\eta^2}\right) + \Delta t i s k \mathscr{F}(f))\Bigg] \end{aligned} \tag{5.16}$$

where $\mathscr{F}$ is the Fourier transform, $\mathscr{F}^{-1}$ is the inverse Fourier transform.

5.3 Validation

After deriving the expression for the wave, U, in the pseudospectral scheme of Eqn 5.16, it was tested against known anayltic solutions of the KP equation. The 2D analytic line soliton solution in Eqn 5.17 [76] was tested, with $\alpha = 6$, $\beta = 1$, $\gamma = 0$, $\mu = 3$. The analytic solution for the wave, U, is:

$$U_{t_0} = 0.5a^2 \text{sech}(0.5a(X - bY - wt/a))^2 \tag{5.17}$$

where $a = 0.5$, $b = -0.02$, $k_x = a$, $k_y = -ab$, and $w = (\mu k_y^2 + \beta k_x^4)/k_x$.

The comparison between the numerical results and analytical solution are shown in Fig 5.1 at t = 10 TU. The difference between the numerical and analytical

results is on the order of $dt/10 = 10^{-4}$, in agreement with the accuracy of the 1D KdV numerical simulations in Chapter 3. The simulation parameters are $\Delta t = 0.001$, $N_x = 1024$, $N_y = 256$, $L_x = 50$, $L_y = 12.5$.

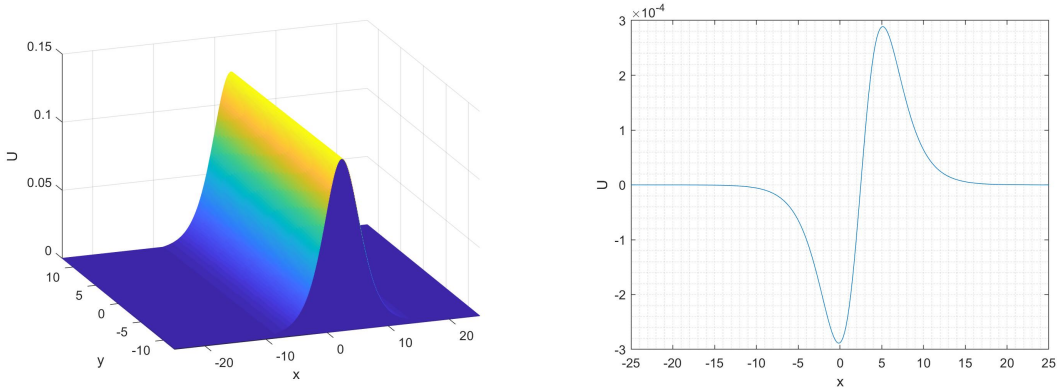

(a) Numerical Simulation of 2D Line Soliton

(b) Difference between Numerical and Analytical Solution

Figure 5.1: Numerical simulation of analytical solution at t = 10 TU. The simulation parameters are $\Delta t = 0.001$, $N_x = 1024$, $N_y = 256$, $L_x = 50$, $L_y = 12.5$.

5.4 2D Debris Results

After deriving the KP equation and testing it against a known analytic solution in Section 5.3, it was applied to the generation of pinned and precursor solitons in Earth's plasma environment due to orbital debris. Plasma parameters were used from the International Reference Ionosphere (IRI) model data [17]. The subcritical and supercritical debris velocity thresholds, which define the generation locations for pinned and precursor solitons, were previously identified in Eqn 3.55-3.56.

5.4.1 Pinned Solitons

To simulate 2D pinned solitons, a region in the IRI data was chosen where pinned solitons can be created for debris sizes ranging between $G = 0.25 - 1$. Data was downloaded for January 1, 2000 at 6pm UTC, 500 km altitude, 0° longitude, and 0° latitude. The dominant ion is oxygen, the Debye length is 0.23 cm, and the ion acoustic velocity is 1.36 km/s. In Fig 5.2 - 5.3, the debris size is 0.17 cm, $G = 0.75$, $V_{sup} = 1.70V_{ia}$, $V_d = 5.2V_{ia}$, at $t = 20$ TU. The domain parameters are $N_x = 1360$, $N_y = 86$, $L_x = 112$, and $L_y = 8$. In our normalized numerical simulation, where $V_{ia} = 0$, the relative velocity between the debris and the ions is $V_{rel} = (V_d - 1)/(V_{sup} - 1) \approx 6$. As shown in Fig 5.2 - 5.3, no additional solitons are produced in the transverse directions. As the wave dampens along the debris propagation direction, a depression zone of decreased density is created in its wake region.

Results are shown in Fig 5.2 - 5.3 for two different debris sizes and speeds. Fig 5.2 shows the pinned soliton produced by a 0.23 cm size debris, $G = 1$, with a supercritical velocity of $V_{sup} = 1.87V_{ia}$, debris velocity $V_d = 2.73V_{ia}$, at $t = 20$ TU. The domain parameters are $N_x = 784$, $N_y = 50$, $L_x = 64$, and $Ly = 4$. In our normalized numerical simulation, where $V_{ia} = 0$, the relative velocity between the debris and the ions is $V_{rel} = (V_d - 1)/(V_{sup} - 1) \approx 2$. As shown in Fig 5.2, no additional solitons are produced in the transverse directions.

Since the damping coefficient, γ, is applied to the X domain, the wave propagation direction, and not the transverse directions, the wave widens along X as

it decays, and does not widen in the transverse directions. Consequently, the ratio of the width of the pinned soliton along X to Y increases with increasing γ, as shown in Fig 5.4. However, pinned solitons do not experience significant damping due to the presence of the persistent debris force at the soliton location, with an average difference in amplitude between the undamped and damped pinned soliton of 0.7% Chapter 4. Therefore, pinned solitons will continue to propagate until the debris enters a region where the plasma characteristics prevent the creation of pinned solitons.

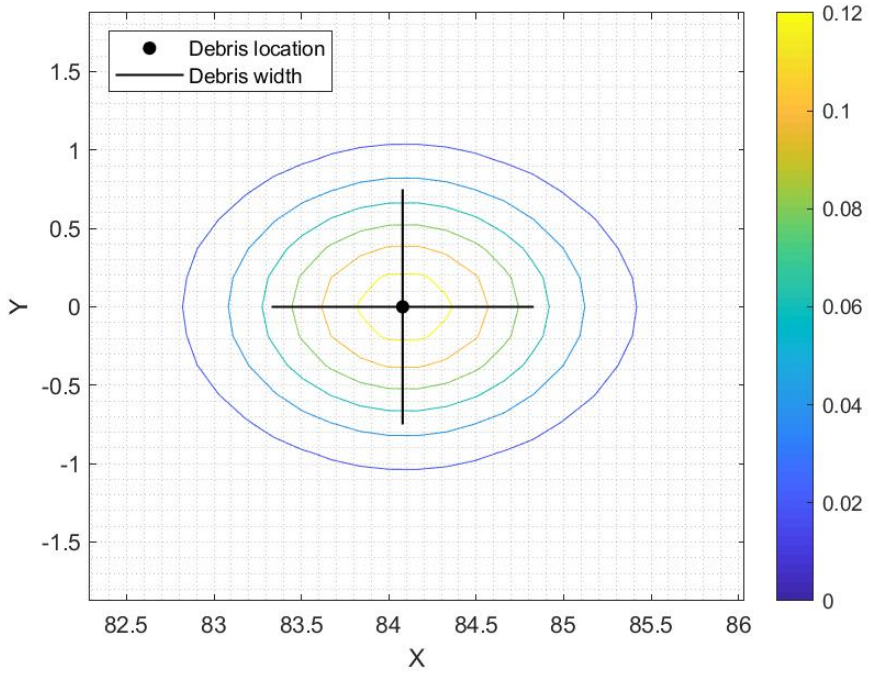

Figure 5.2: Contour plot of pinned soliton created by debris size $G = 0.75$, debris speed $V_{rel} = 6$, at t = 20 TU.

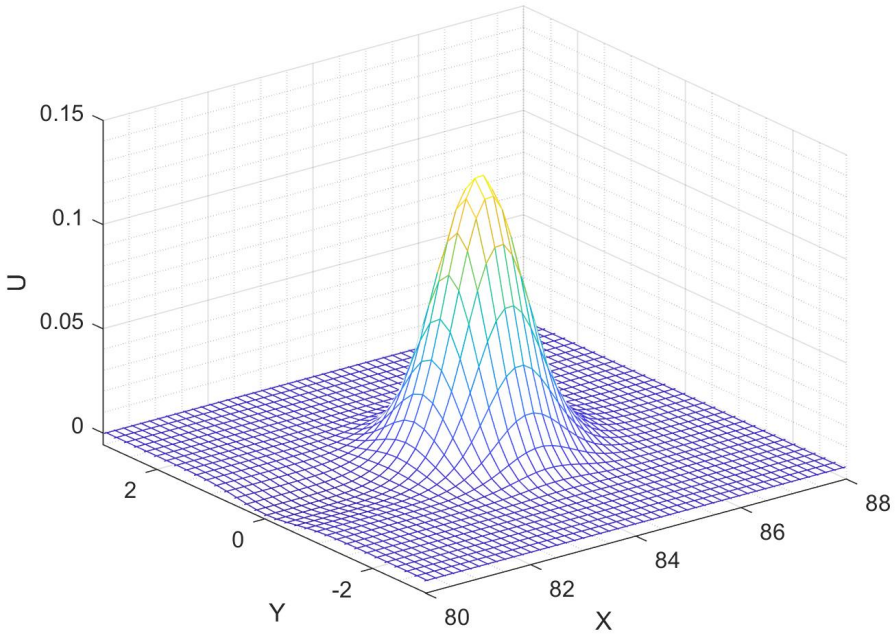

Figure 5.3: Pinned soliton created by debris size $G = 0.75$, debris speed $V_{rel} = 6$, at t = 20 TU.

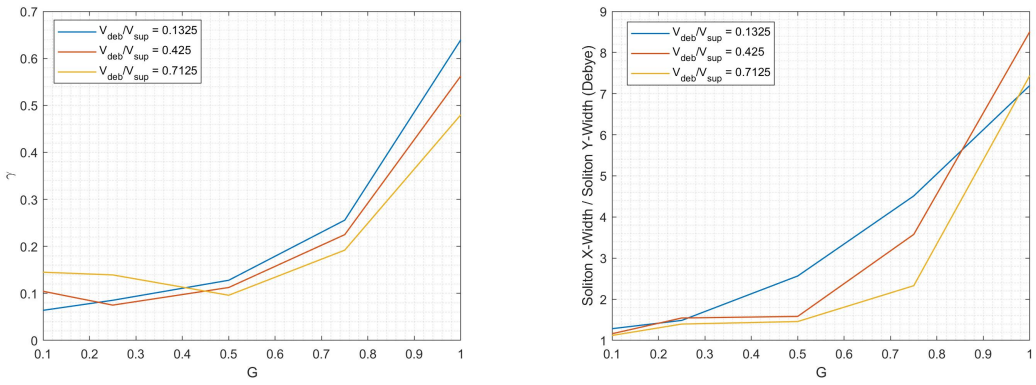

(a) Damping Coefficient

(b) Ratio of width in X and Y

Figure 5.4: (a) Damping coefficient, γ, as a function of debris size and speed, as calculated in Chapter 4. (b) Ratio of pinned soliton width in the X domain to soliton width in the Y domain.

5.4.2 Precursor Solitons

To simulate 2D precursor solitons, a region in the IRI data was chosen where precursor solitons can be created for debris sizes ranging between $G = 0.25 - 1$. Data was downloaded for July 1, 2000 at 6pm UTC, 1600 km altitude, 0° longitude, and 0° latitude. The dominant ion is hydrogen, the Debye length is 2.81 cm, and the ion acoustic velocity is 6 km/s. Results are shown in Fig 5.5 two different debris sizes and speeds. On the top is the results for debris size 1.4cm, $G = 0.5$, with a supercritical velocity of $V_{sup} = 1.4V_{ia}$, debris velocity $V_d = 1.17V_{ia}$ $V_{rel} = 0.425$, at $t = 67.64$ TU. The domain parameters are $N_x = 1360$, $N_y = 86$, $L_x = 112$, and $L_y = 8$. On the bottom of Fig 5.5, the debris size is 2.11 cm, $G = 0.75$, $V_{sup} = 1.5457V_{ia}$, $V_d = 1.08V_{ia}$, $V_{rel} = 0.1375$, at $t = 79.8$ TU. The domain parameters are $N_x = 1168$, $N_y = 74$, $L_x = 96$, and $L_y = 6$. As shown in Fig 5.5, in addition to the precursor solitons that propagate from the center of the debris and advance ahead along the debris velocity vector on the X axis, precursor solitons are created across the width of the debris, and also advance ahead of the debris. The relationship between the frequency and distribution of the transverse solitons extended across the width of the debris is predictable. Transverse solitons have been observed in other 2D Kadomtsev-Petviashvili systems with negative bottom topography, where the production of the transverse solitons is dependent on the bottom topography size and speed [96, 97].

The profile of precursor solitons in the presence of positive bottom topography will aid in understanding the formation of precursor solitons in the presence of

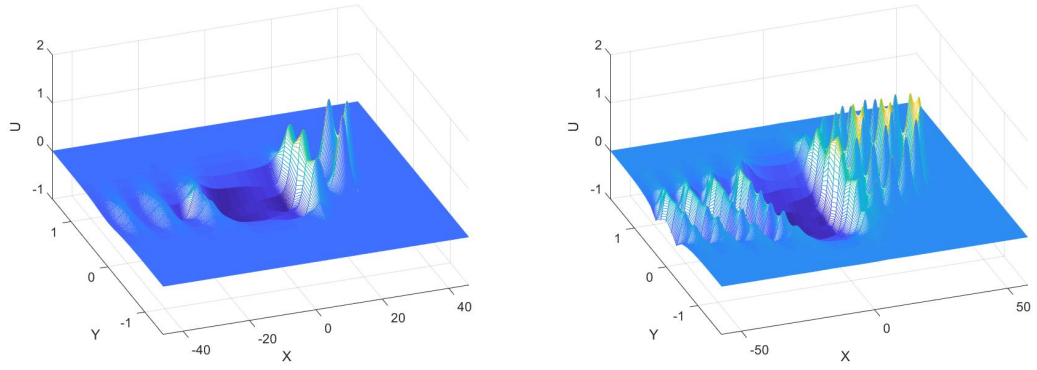

(a) G = 0.5 (b) G = 0.75

Figure 5.5: 2D simulation results for precursor solitons for two different debris sizes and speeds. (a) $G = 0.5$, $V_{rel} = 0.425$, at $t = 67.64$ TU. (b) $G = 0.75$, $V_{rel} = 0.1375$, at $t = 79.8$ TU.

negative bottom topography. A positive forcing function will produce stable soliton density curves that advance ahead across the width of the debris. An example is shown in Fig 5.6, at $t = 20$ TU. The force is a Gaussian as described in Eqn 5.13, with $\Phi_{p,n} = 1$, $V_{d_x} = V_{d_y} = 0$, $a_x/\lambda_D = 3$, and $a_y/\lambda_D = 6$. Stable curves are produced for both positive and negative KP coefficients. For Fig 5.6, $\alpha = -6$, $\beta = -1$, and $\mu = -3$. In contrast, a system containing a negative forcing function can be thought of as unstable, and will not product stable soliton density curves, however the transverse solitons produced will have the same amplitude and speed of a soliton density curve at the same location when compared to solitons created by a positive forcing function.

In the 2D KP orbital debris system, the amplitude, width, and speed of the transverse precursor solitons can be predicted by applying the 1D KdV solution at the given transverse distance away from the debris center. Fig 5.7 shows the results

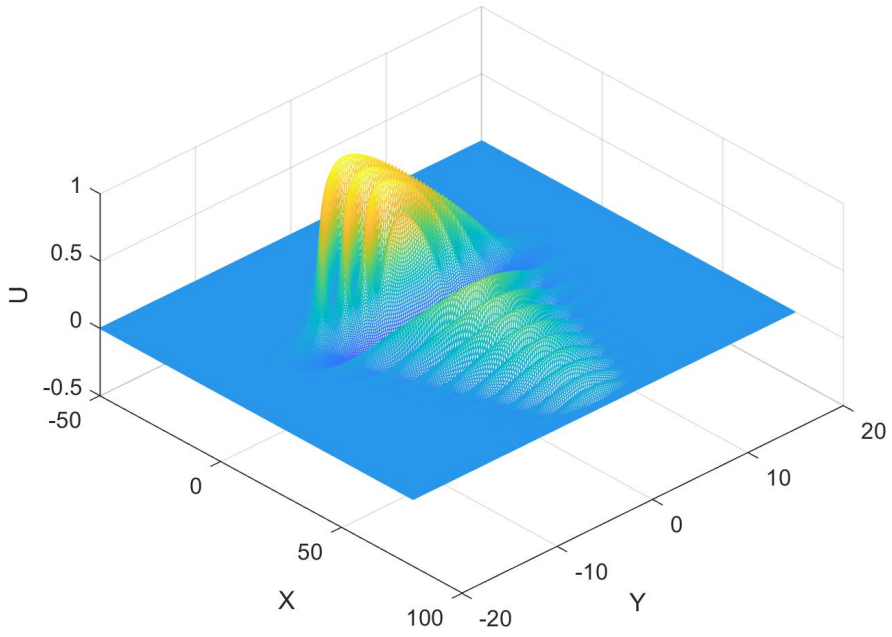

Figure 5.6: Precursor soliton density curves created by a positive Gaussian force as described in Eqn 5.13, with $A = 1$, $V_d = 0$, $G_x = 3$, and $G_y = 6$, at t = 20 TU.

of simulating a 1D system along the width of the debris for one example debris size, for $G = 0.75$, $V_{rel} = 0.1375$, at $t = 79.8$ TU, as shown in Fig 5.5. The 2D results are displayed as contour plot, and the peaks of sample offset 1D simulations are overplotted. The difference between the 1D and 2D simulations at the transverse soliton locations is on the order of $dt = 10^{-3}$, with an example shown in Fig 5.7.

Figure Fig 5.8 shows the relationship between the normalized damping coefficient, γ, as calculated in Chapter 4, the debris size, and debris speed. In order to improve on computation efficiency, the number of samples along X and Y in each simulation displayed, N_x and N_y, were calculated based on the debris speed, size,

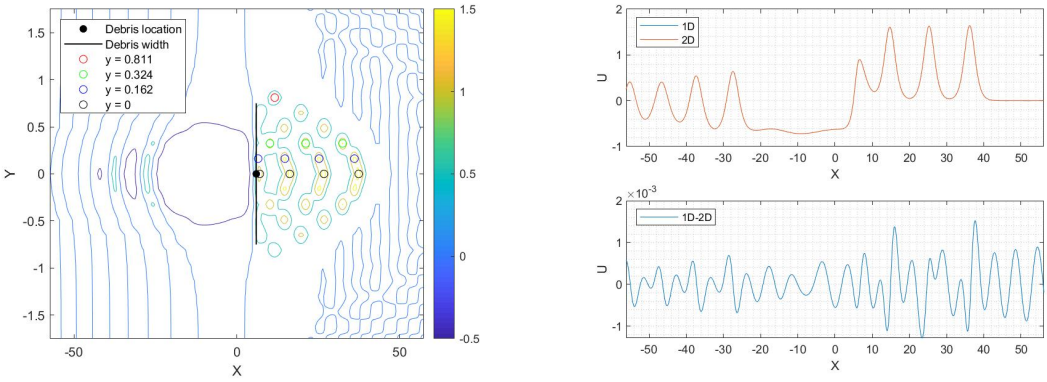

(a) G = 0.75 contour

(b) G = 0.75 y = 0.162

Figure 5.7: (a) Contour plot of 2D results for G = 0.75, with 1D simulations overplotted at sample Y offsets. (b) Difference between 1D and 2D results at $y = 0.162$.

and estimated time to generate two precursor solitons. As an example, for debris size $G = 0.5$ and debris speed $V_{rel} = 0.425$, $N_x = 1360$ and $N_y = 86$, $L_x = 112$, and $L_y = 8$. For debris size $G = 0.75$ and debris speed $V_{rel} = 0.1375$, $N_x = 1168$, $N_y = 74$, $L_x = 96$, and $L_y = 6$.

The distance between transverse solitons appears to be independent of debris speed, and does not follow the trend of the normalized damping coefficient. In order to rule out the influence of different sample sizes on transverse soliton distance, additional simulations were run where N_x and N_y remained the same for all the debris sizes and speeds tested in Fig 5.8. To expedite these tests, the time increment was increased to $dt = 0.01$. For the first test, $N_x = 3712$, $N_y = 232$, $L_x = 176$, and $L_y = 12$. For all debris sizes and speeds, the transverse soliton distance was $\Delta y = 0.103$. For the second test, $N_x = 2032$, $N_y = 2032$, $L_x = 96$, and $L_y = 96$. For all debris sizes and speeds, the transverse soliton distance was $\Delta y = 0.09449$. For

the final test $N_x = 2032$, $N_y = 2540$, $L_x = 96$, and $L_y = 120$. For all debris sizes and speeds, the transverse soliton distance was again $\Delta y = 0.09449$. It is possible that the true transverse soliton distance for each debris size and speed may require higher computing capacity. Further investigation is required to predict the distance between transverse solitons.

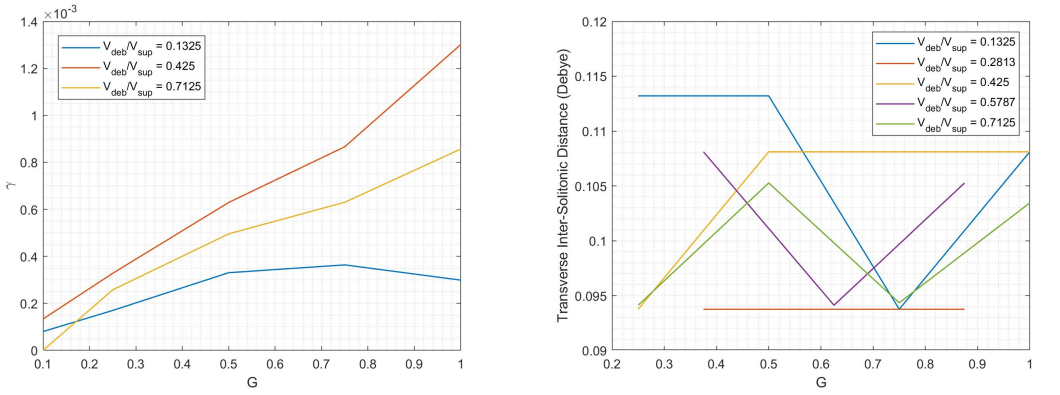

(a) Damping Coefficient

(b) Y distance between transverse solitons

Figure 5.8: Damping coefficient, γ, as a function of debris size and speed, as calculated in Chapter 4. Distance between transverse solitons in the Y domain.

5.5 3D Debris Results

After simulating orbital debris solitons in two spatial dimensions, we extended the visualization to three dimensions in order to understand the full signature of orbital debris solitons in an Earth orbiting reference frame. It is critical to understand the fully 3D soliton signature in order to design detection technology.

According to Eqn 5.2, the dispersion coefficient, μ, is applied uniformly in all transverse directions [91, 94]. Thus, we can assume that the transverse perturbations

in the Y domain will be identical to the perturbation in the Z domain, and all angles in the Y-Z plane about the X axis. To create a visualization with three spatial dimensions and one amplitude dimension, we rotated the 2D results about the X axis at one degree increments and replicated the transverse perturbations in the Y-Z plane. Results are shown in Fig 5.9 for the soliton shown in Fig 5.5 for two different debris sizes and speeds. For $G = 0.75$ and $V_{rel} = 0.1375$, a visualization is created to the scale of the debris size in Fig 5.10. The precursor solitons created at the center of the debris remain the highest amplitude and frequency solitons. The transverse solitons along the width of the debris create soliton rings in the Y-Z plane that advance ahead of the debris along the debris velocity vector in the X domain. Three dimensional soliton rings have been observed in other fluid media, to include Fermi gas [98], laser media [99], shallow water vortex rings created by dolphins [100], and Bose-Einstein condensates and nonlinear optics [101].

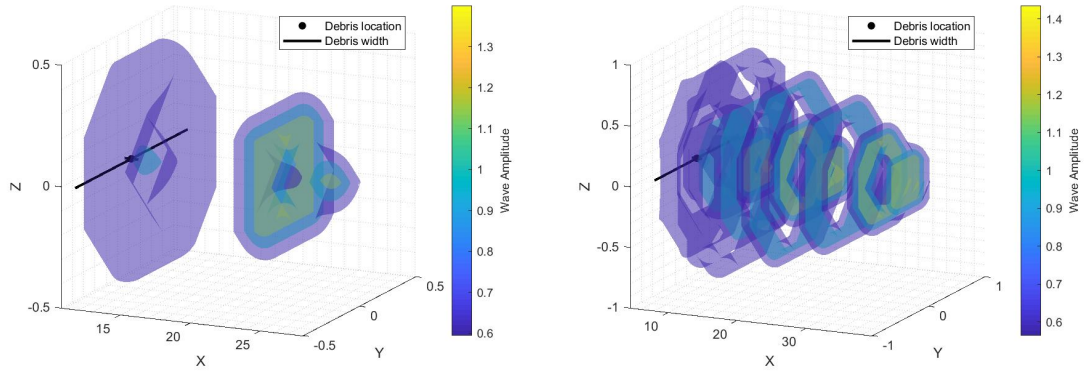

(a) G = 0.5 (b) G = 0.75

Figure 5.9: 3D simulation results for precursor solitons for two different debris sizes and speeds. Top: $G = 0.5$, $V_{rel} = 0.425$, at $t = 67.64$ TU. Bottom: $G = 0.75$, $V_{rel} = 0.1375$, at $t = 79.8$ TU.

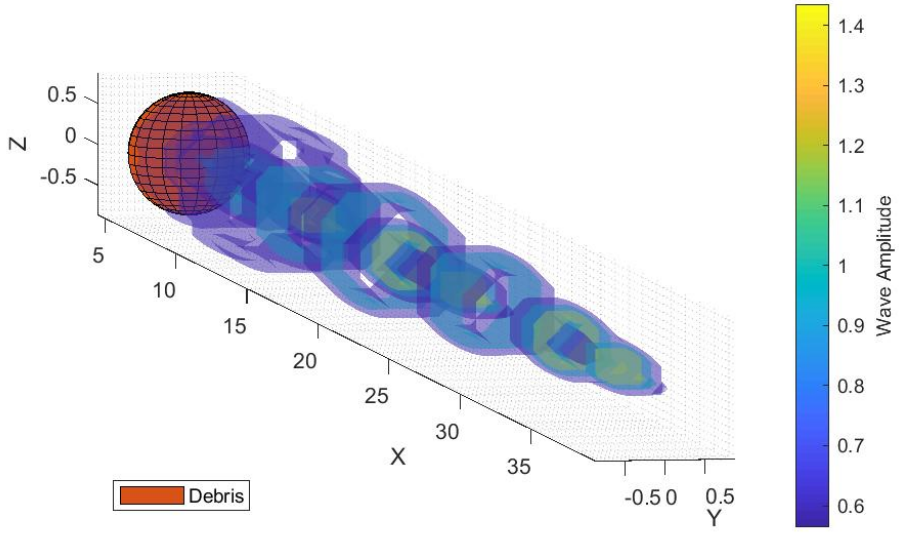

Figure 5.10: 3D simulation results in the equal axis scale for precursor solitons $G = 0.75$, $V_{rel} = 0.1375$, at $t = 79.8$ TU.

5.6 Orbital Energy

The results of this research leads to a question of whether soliton energy will influence orbital debris energy. We conduct a preliminary calculation based on orbital debris with radius $a = 0.5$ cm in a circular orbit of $V_d = 7.26$ km/s at 1200 km altitude, in the region of High LEO 1 in as described in Table 3.1. The Debye length is $\lambda_D = 1.38$ cm, the plasma density is $n_0 = 10^{11}\text{m}^{-3}$, and the electron temperature is $T_e = 0.35$ eV. Soliton amplitude for sub-centimeter debris ranges from 1-2x the background density, and the soliton width ranges from 5-20x the Debye length. We will assume that the soliton amplitude is $n_s = 1.5n_0$, the soliton width is $w = 10\lambda_D$, the soliton speed is $V_s = 8.26$ km/s. The volume of the soliton becomes $x_s = 2\pi w^3 = 0.0165\text{m}^3$.

As discussed in Chapter 3, the surface potential of spherical debris in hydrogen dominated plasma is $\Phi_s = -2.51k_bT_e/e = -0.88$ eV in the thick sheath domain, which is when the debris is smaller than the Debye length. The charge of the debris becomes $Q_D = 4\pi\epsilon_0 a\Phi_s$. Therefore, potential energy of the debris in the presence of the background plasma is $U_{E_0} = 1/4\pi\epsilon_0 \sum_{i=1}^{n_0 x_s} Q_D q_i/\lambda_D = -4\text{x}10^{-9}$J. Similarly, the potential energy of the debris in the presence of the background plasma and a precursor soliton is $U_{E_1} = U_{E_0} + 1/4\pi\epsilon_0 \sum_{i=1}^{n_s x_s} Q_D q_i/\lambda_D = U_{E_0} + 1.5U_{E_0} = 2.5U_{E_0}$. The change in potential energy is $\Delta U_E = U_{E_1} - U_{E_0} = 1.5U_{E_0} = -6.9\text{x}10^{-9}$J.

The kinetic energy of the spherical debris is $K_{E_d} = 1/2m_dV_d^2$, where the assumed density of the debris is $n_d = 2$ g/cm^{-3} and the mass of the debris is $m_d = 4/3\pi a^3 n_d = 10^{-3}$kg. The mass of the soliton is calculated assuming a packet

of hydrogen ions with ion mass equal to the proton mass $m_i = m_p = 1.67\text{x}10^{-27}$kg. Then, the mass of the soliton is $m_s = n_s x_s m_i = 2.76\text{x}10^{-18}$kg. Therefore, the debris kinetic energy is $K_{E_d} = 2.6\text{x}10^{4}$J and the soliton kinetic energy is $K_{E_s} = 9\text{x}10^{-11}$J.

It is assumed that the soliton kinetic energy is negligible and the soliton potential energy can cause a change in total orbital debris energy, where $E = -(\mu/2r)m_d$. The debris will decrease in orbital altitude as the total energy, E, decreases. To calculate the amount of time for the debris to decrease from 1200 km altitude to 1000 km altitude, we calculate the total energy for the number of precursor solitons produced at each orbit. N_s is the number of precursor solitons produced in a single orbit, which decreases exponentially as the debris velocity approaches the supercritical limit. The 0.5 cm debris in this example produces $N_s = 6.6\text{x}10^{6}$ precursor solitons at 1200 km altitude, $N_s = 2.9\text{x}10^{6}$ precursor solitons at 1000 km altitude, and pinned solitons below 1000 km altitude. For debris with mass $m_d = 1$ g, the orbital energy at 1200 km altitude is 27.57 kJ, and the orbital energy at 1000km altitude is 28.31 kJ. Assuming an exponential decrease in the number of precursors solitons produced as the altitude decreases, as detailed in Chapter 3 and shown in Figure 3.14, the total estimated time for the debris to decrease in altitude from 1200 km to 1000 km is 5.29 years. Similarly, the time for 0.5 cm debris at an 2000 km altitude would descend to 1000 km altitude in 10.95 years. This estimation largely depends on the the velocity of the debris relative to the supercritical velocity of the debris in the current plasma environment.

These calculations are for the precursor solitons that propagate from the center of the debris, which have a higher density and frequency when compared to the

precursor solitons produced along the width of the debris and described in Chapter 5. For orbital debris in the presence of pinned solitons, $N_s = 1$, and the change in energy per orbit is again $U_{E_0} = -6.9\text{x}10^{-9}$J. Therefore, the generation of precursor solitons will act as a drag force on the debris, causing it to decrease in altitude, until it enters a region where pinned solitons are produced. It is theorized that orbital debris will become grouped at altitudes defined by their previous precursor soliton generation. For debris originating at altitudes and latitudes within the regions identified for precursor soliton generation in Figure 3.27, the precursor solitons will cause a decrease in altitude until the minimum altitude is reached for the given debris size and plasma environment.

5.7 Conclusion

In Chapters 3-4, we identified the orbital altitudes and latitudes where solitons can be created from orbital debris, which have amplitudes above the threshold of detectability from current ground and space sensors [60, 61, 62]. We modeled the soliton altitude, latitude, width, frequency, and propagation distance as a function of debris size and speed. Now, we conclude that precursor solitons will be accompanied by 3D ring solitons, which will propagate along the debris velocity vector at radii defined by the debris width and at predictable intervals. These transverse solitons will allow for additional opportunity to measure previously undetectable orbital debris, in a region where the characteristics of the sub-centimeter debris population are largely uncertain.

Chapter 6: Conclusions and Future Work

Currently, the small orbital debris concentrations in High LEO are not well understood. NASA's small orbital debris estimations are largely based on *in-situ* measurements during the Space Shuttle mission at altitudes lower than 600 km, and it is expected that these measurements underestimate the amount of debris at higher altitudes [6]. With the increase in frequency of satellite launches, the gap in understanding the small debris population only worsens the risk for catastrophic failure to satellites. As stated by Nicholas Johnson, the former NASA chief scientist for orbital debris, "The greatest risk to space missions comes from non-trackable debris," [102].

We have demonstrated that charged orbital debris can create pinned solitons in the O+ dominated regions of mid-latitude low LEO, at altitudes below 800 km, and precursor solitons in H+ dominated high LEO, at altitudes above 800 km. Debris with radius 0.5 cm can produce precursor solitons at altitudes down to 1000 km, 0.5 mm radius debris can produce precursor solitons at altitudes down to 1700 km, and micron sized debris can produce precursor solitons at altitudes down to 1850 km. When compared to the SSN estimates for orbital debris as illustrated in Figure 2.1, precursor solitons will be produced in the regions above 800km altitude

where orbital debris density is the highest. Precursor solitons are more likely to occur in mid-latitude regions, which cannot be observed by current ground based radar and optical methods. Further, as opposed to ground based radar, where the object detection size decreases rapidly with altitude, we are able to measure even smaller sized objects with increasing altitude, and will be able to measure undetected objects in the 1400-1600 altitude range. Models were generated to predict the amplitude and width of solitons, and frequency of soliton production, in order to assess the detectability of the signal and enable on-orbit mapping of sub-centimeter orbital debris. This research can be further refined by extending simulations beyond the fKdV equation, which invokes the long wavelength assumption, and using the fully nonlinear set of fluid equations. As shown in [57], the fKdV equation is in agreement with the fully nonlinear equations for waves of where the amplitude is smaller than the wavelength, but starts to diverge as the forcing function velocity increases and approaches the supercritical velocity limit. Additionally, we assumed that the electron distribution can be modeled by the Boltzmann equation. A more accurate representation will include the effects of magnetized electrons on the plasma density.

The propagation distance of solitons was calculated, which is necessary in order to assess the detectability of precursor solitons via satellite or ground observations, the time required to map detectable debris, and the number of sensors needed for mapping in a given mission window. We demonstrated that kinetic collisions will not produce damping above 400 km altitude. In the presence of Landau damping, the median propagation distance for precursor solitons is 10 km for 0.5 mm radius debris,

and 6 km for 0.5 cm radius debris. We show that precursor soliton propagation distances are influenced by seasonal and diurnal effects, with longer propagation distances during the summer when compared to winter, and day when compared to night. While the plasma environment is dynamic, we show that the plasma properties do not change more than 1% over the maximum propagation distances, thus the KdV coefficients will remain constant and the variable KdV equation is not needed for accurate modeling of these solitons. Pinned solitons in low LEO will not experience significant Landau damping due to the presence of the persistent debris force, and will continue to propagate until entering an area where pinned solitons cannot be produced. Additional damping processes should be considered moving forward, to include the time evolution effects of localized electric fields on the velocity distribution function [86].

In 3D space, precursor solitons will be accompanied by 3D ring solitons in the transverse plane, which will advance ahead of the debris along the debris velocity vector. The density and frequency of the soliton rings are defined by the debris width and speed. The predictions for 1D propagation of both pinned and precursor solitons are in agreement with the 2D and 3D projections. The 1D KdV numerical simulation, combined with the 2D and 3D KP transverse soliton spacing trends, provide the characteristics needed to evaluate the feasibility of soliton detection with existing sensors or design new detectors. With additional transverse solitons, the determination of the originating debris can be refined with fewer detections. More simulations are required with a higher number of samples in order to predict the transverse soliton spacing distance as a function of debris size and speed.

Further research is necessary to assess the feasibility of estimating the originating debris' size and speed from the characteristics of the soliton produced. In order to identify a soliton, more than one detection is required to verify that the soliton maintains its shape and speed during propagation [23], differentiating it from other plasma perturbations. Once detected, the soliton would need to be fit to existing models of soliton width, amplitude, velocity, and damping rate in order to identify a range of valid debris sizes and speeds which potentially created the soliton. Additional detections of soliton amplitude and frequency in the transverse directions will help to confirm the initial estimate for debris size and speed. As a proof of concept, existing ion density data can be queried to identify pinned or precursor solitons from known tracked debris objects. Once soliton detection techniques are designed, solitons will allow for mapping of sub-centimeter orbital debris in LEO, providing a capability to characterize the orbital debris population with existing sensor technology, in a region where orbital debris estimations are not fully understood.

Bibliography

[1] Kim Gaik Tay. Method of lines and pseudospectral solutions of the forced korteweg-de vries equation with variable coefficients arises in elastic tube. *International Journal of Pure and Applied Mathematics*, 116:985–998, Nov 2017.

[2] T. Yao-Tsu Wu. Generation of upstream advancing solitons by moving disturbances. *Journal of Fluid Mechanics*, 184(1):75, Nov 1987.

[3] EL Christiansen, JL Hyde, and RP Bernhard. Space shuttle debris and meteoroid impacts. *Advances in Space Research*, 34(5):1097–1103, 2004.

[4] NASA. *NASA Technology Roadmaps: TA 5: Communications, Navigation and Orbital Debris Tracking and Characterization Systems*, chapter 5.7 Orbital Debris Tracking and Characterization. NASA, 2015.

[5] Nasa orbital debris program office faq, December 2018.

[6] Michael A. Tsao, Hau T. Ngo, Robert D. Corsaro, and Christopher R. Anderson. An in situ measurement system for characterizing orbital debris. *IEEE Transactions on Instrumentation and Measurement*, 65(12):2758–2772, Dec 2016.

[7] M Matney. Nasa orbital debris program office quarterly news, Aug 2017.

[8] J Goree. Charging of particles in a plasma. *Plasma Sources Science and Technology*, 3(3):400–406, Aug 1994.

[9] Abhijit Sen, Sanat Tiwari, Sanjay Mishra, and Predhiman Kaw. Nonlinear wave excitations by orbiting charged space debris objects. *Advances in Space Research*, 56(3):429–435, Aug 2015.

[10] Sanat Kumar Tiwari and Abhijit Sen. Wakes and precursor soliton excitations by a moving charged object in a plasma. *Physics of Plasmas*, 23(2):22301, Feb 2016.

[11] Surabhi Jaiswal, P. Bandyopadhyay, and A. Sen. Experimental observation of precursor solitons in a flowing complex plasma. *Physical Review E*, 93(4), Apr 2016.

[12] P. A. Lindqvist, G. T. Marklund, and L. G. Blomberg. Plasma characteristics determined by the freja electric field instrument. *Space Science Reviews*, 70(3–4):593–602, Nov 1994.

[13] J.K. Shi, B.Y. Xu, K. Torkar, T.L. Zhang, and Z.X. Liu. An electrostatic model for nonlinear waves in the upper ionosphere. *Advances in Space Research*, 32(3):303–308, Jan 2003.

[14] Xiaofeng Li. Synthetic aperture radar observation of the sea surface imprints of upstream atmospheric solitons generated by flow impeded by an island. *Journal of Geophysical Research*, 109(C2), 2004.

[15] M. Widner. Plasma expansion into a vacuum. *Physics of Fluids*, 14(4):795, 1971.

[16] W. Alpers, Heng Wang-Chen, and Lim Hock. Observation of internal waves in the andaman sea by ers sar. In *IGARSS'97. 1997 IEEE International Geoscience and Remote Sensing Symposium Proceedings. Remote Sensing - A Scientific Vision for Sustainable Development*, pages 1287–1292. IEEE, 1997.

[17] D. Bilitza, D. Altadill, V. Truhlik, V. Shubin, I. Galkin, B. Reinisch, and X. Huang. International reference ionosphere 2016: From ionospheric climate to real-time weather predictions. *Space Weather*, 15(2):418–429, Feb 2017.

[18] *Limiting Future Collision Risk to Spacecraft*. National Academies Press, Nov 2011.

[19] Donald J. Kessler and Burton G. Cour-Palais. Collision frequency of artificial satellites: The creation of a debris belt. *Journal of Geophysical Research*, 83(A6):2637, 1978.

[20] JS Russell. Report of the fourteenth meeting of the british association for the advancement of science, york. 1844.

[21] D. J. Korteweg and G. de Vries. Xli. on the change of form of long waves advancing in a rectangular canal, and on a new type of long stationary waves. *The London, Edinburgh, and Dublin Philosophical Magazine and Journal of Science*, 39(240):422–443, May 1895.

[22] Soliton wave receives crowd of admirers. *Nature*, 376:373, August 1995.

[23] R. Trines, R. Bingham, M. W. Dunlop, A. Vaivads, J. A. Davies, J. T. Mendonça, L. O. Silva, and P. K. Shukla. Spontaneous generation of self-organized solitary wave structures at earth's magnetopause. *Physical Review Letters*, 99(20), Nov 2007.

[24] N. J. Zabusky and M. D. Kruskal. Interaction of "solitons" in a collisionless plasma and the recurrence of initial states. *Physical Review Letters*, 15(6):240–243, Aug 1965.

[25] J. L. Bona and R. W. Smith. The initial-value problem for the korteweg-de vries equation. *Philosophical Transactions of the Royal Society of London. Series A, Mathematical and Physical Sciences*, 278(1287):555–601, Jul 1975.

[26] B. Fornberg and G. B. Whitham. A numerical and theoretical study of certain nonlinear wave phenomena. *Philosophical Transactions of the Royal Society A: Mathematical, Physical and Engineering Sciences*, 289(1361):373–404, May 1978.

[27] Tony F. Chan and Tom Kerkhoven. Fourier methods with extended stability intervals for the korteweg-de vries equation. *SIAM Journal on Numerical Analysis*, 22(3):441–454, 1985.

[28] F.Z Nouri and D.M Sloan. A comparison of fourier pseudospectral methods for the solution of the korteweg-de vries equation. *Journal of Computational Physics*, 83(2):324–344, Aug 1989.

[29] Simon Ramo. Space charge and field waves in an electron beam. *Physical Review*, 56(3):276–283, Aug 1939.

[30] F. Hahn, W. Biedermann, Haagen, Ostertag, Albers, Stelzer, Haagen, Sponholz, and Küster. Infektion. *Zeitschrift für Krebsforschung*, 48(S4):258–262, Jul 1939.

[31] J. E. Feir. Discussion: Some results from wave pulse experiments. *Proceedings of the Royal Society of London. Series A. Mathematical and Physical Sciences*, 299(1456):54–58, Jun 1967.

[32] Henry C. Yuen and Bruce M. Lake. Nonlinear deep water waves: Theory and experiment. *Physics of Fluids*, 18(8):956, 1975.

[33] Henry C. Yuen and Bruce M. Lake. *Nonlinear Dynamics of Deep-Water Gravity Waves*, page 67–229. Elsevier, 1982.

[34] Alexis S Truitt and Christine M Hartzell. Simulating plasma solitons from orbital debris using the forced korteweg–de vries equation. *Journal of Spacecraft and Rockets*, accepted.

[35] A. V. Gurevich. *Nonlinear Phenomena in the Ionosphere.* Springer Berlin Heidelberg, 1978.

[36] Fabricio dos Santos Prol, Manuel Hernandez-Pajares, Paulo de Oliveira Camargo, and Marcio Tadeu de Assis Honorato Muella. Spatial and temporal features of the topside ionospheric electron density by a new model based on gps radio occultation data. *Journal of Geophysical Research: Space Physics*, Mar 2018.

[37] P. Sibanda and L. A. McKinnell. Topside ionospheric vertical electron density profile reconstruction using gps and ionosonde data: possibilities for south africa. *Annales Geophysicae*, 29(2):229–236, Feb 2011.

[38] Pencho Marinov, Ivan Kutiev, Anna Belehaki, and Ioanna Tsagouri. Modeling the plasmasphere to topside ionosphere scale height ratio. *Journal of Space Weather and Space Climate*, 5:A27, 2015.

[39] D. E. Hastings. A review of plasma interactions with spacecraft in low earth orbit. *Journal of Geophysical Research*, 100(A8):144–157, 1995.

[40] M. H. Denton. Bulk plasma properties at geosynchronous orbit. *Journal of Geophysical Research*, 110(A7), 2005.

[41] Atsuhiro Nishida. Average structure and storm-time change of the polar topside ionosphere at sunspot minimum. *Journal of Geophysical Research*, 72(23):6051–6061, Dec 1967.

[42] R.D. Leach, M.B. Alexander, Systems Analysis, Integration Laboratory (George C. Marshall Space Flight Center). Electromagnetics, and Environments Branch. *Failures and anomalies attributed to spacecraft charging*. NASA reference publication. National Aeronautics and Space Administration, Marshall Space Flight Center, 1995.

[43] Haruichi Washimi and Tosiya Taniuti. Propagation of ion-acoustic solitary waves of small amplitude. *Physical Review Letters*, 17(19):996–998, Nov 1966.

[44] Samuel S. Shen. *A Course on Nonlinear Waves*. Springer Netherlands, 1993.

[45] M. Nouri Kadijani and H. Zaremoghaddam. Effect of dust grains on dust-ion-acoustic kdv solitons in magnetized complex plasma with superthermal electrons. *Journal of Fusion Energy*, 31(5):455–462, Nov 2011.

[46] S. Sultana. Ion acoustic solitons in magnetized collisional non-thermal dusty plasmas. *Physics Letters A*, 382(20):1368–1373, May 2018.

[47] M. Cabral and R. Rosa. Chaos for a damped and forced kdv equation. *Physica D: Nonlinear Phenomena*, 192(3–4):265–278, Jun 2004.

[48] E. Ott. Damping of solitary waves. *Physics of Fluids*, 13(6):1432, 1970.

[49] V. Pierrard and J. Lemaire. Lorentzian ion exosphere model. *Journal of Geophysical Research: Space Physics*, 101(A4):7923–7934, Apr 1996.

[50] George Livadiotis. Statistical origin and properties of kappa distributions. *Journal of Physics: Conference Series*, 900:12014, Sep 2017.

[51] V. Pierrard and K. Stegen. A three-dimensional dynamic kinetic model of the plasmasphere. *Journal of Geophysical Research: Space Physics*, 113(A10), Oct 2008.

[52] V. Pierrard and M. Lazar. Kappa distributions: Theory and applications in space plasmas. *Solar Physics*, 267(1):153–174, Oct 2010.

[53] J. Lemaire and M. Scherer. Exospheric models of the topside ionosphere. *Space Science Reviews*, 15(5), Mar 1974.

[54] Gerd W. Prölss. *Physics of the Earth's Space Environment*. Springer Berlin Heidelberg, 2004.

[55] R. De Bibhas. Electric potential on solid spheres in a plasma. *Astrophysics and Space Science*, 30(1):135–147, Sep 1974.

[56] Dan M. Goebel and Ira Katz. *Fundamentals of Electric Propulsion*. John Wiley & Sons, Inc., Jul 2008.

[57] Roger Grimshaw, Montri Maleewong, and Jack Asavanant. Stability of gravity-capillary waves generated by a moving pressure disturbance in water of finite depth. *Physics of Fluids*, 21(8):82–101, Aug 2009.

[58] Zhao Jun-Xiao and Guo Bo-Ling. Analytic solutions to forced kdv equation. *Communications in Theoretical Physics*, 52(2):279–283, Aug 2009.

[59] Miki Wadati and Morikazu Toda. The exact n-soliton solution of the korteweg-de vries equation. *Journal of the Physical Society of Japan*, 32(5):1403–1411, May 1972.

[60] N. A. Zabotin and J. W. Wright. Ionospheric irregularity diagnostics from the phase structure functions of mf/hf radio echoes. *Radio Science*, 36(4):757–771, Jul 2001.

[61] M.T. Rietveld, J.W. Wright, N. Zabotin, and M.L.V. Pitteway. The tromsø dynasonde. *Polar Science*, 2(1):55–71, Mar 2008.

[62] Biagio Forte, Chris Coleman, Susan Skone, Ingemar Häggström, Cathryn Mitchell, Federico Da Dalt, Tommaso Panicciari, Joe Kinrade, and Gary Bust. Identification of scintillation signatures on gps signals originating from plasma structures detected with eiscat incoherent scatter radar along the same line of sight. *Journal of Geophysical Research: Space Physics*, 122(1):916–931, Jan 2017.

[63] H. S. S. Sinha. *Rocket-borne Langmuir probe for plasma density irregularities*, page 77–90. TERRAPUB, 2013.

[64] Roger Grimshaw, Efim Pelinovsky, and Xin Tian. Interaction of a solitary wave with an external force. *Physica D: Nonlinear Phenomena*, 77(4):405–433, Oct 1994.

[65] Stanley D. Shawhan. The menagerie of geospace plasma waves. *Space Science Reviews*, 42(1–2):257–274, Oct 1985.

[66] Gérard Belmont, Roland Grappin, Fabrice Mottez, Filippo Pantellini, and Guy Pelletier. *Collisionless Plasmas in Astrophysics*. Wiley-VCH Verlag GmbH & Co. KGaA, Oct 2013.

[67] NOAA-NGDC. Geomagnetic coordinate system (2010) [online], http://www.ngdc.noaa.gov/geomag/wmm/icons/wmm2010_coor.png.

[68] Jesper Lindkvist, Mats Holmström, Shahab Fatemi, Martin Wieser, and Stas Barabash. Ceres interaction with the solar wind. *Geophysical Research Letters*, 44(5):2070–2077, Mar 2017.

[69] Andrew Poppe and Mihály Horányi. Simulations of the photoelectron sheath and dust levitation on the lunar surface. *Journal of Geophysical Research: Space Physics*, 115(A8), Aug 2010.

[70] M. Benna, P. R. Mahaffy, J. S. Halekas, R. C. Elphic, and G. T. Delory. Variability of helium, neon, and argon in the lunar exosphere as observed by the ladee nms instrument. *Geophysical Research Letters*, 42(10):3723–3729, May 2015.

[71] R. E. Johnson, R. M. Killen, Jr. Waite, J. H., and W. S. Lewis. Europa's surface composition and sputter-produced ionosphere. *Geophysical Research Letters*, 25(17):3257–3260, Sep 1998.

[72] National Research Council. *Orbital Debris: A Technical Assessment*. National Academies Press, Jun 1995.

[73] D. L. Carpenter and C. G. Park. On what ionospheric workers should know about the plasmapause-plasmasphere. *Reviews of Geophysics*, 11(1):133, 1973.

[74] Chih-Hua Chang and Keh-Han Wang. Generation of three-dimensional fully nonlinear water waves by a submerged moving object. *Journal of Engineering Mechanics*, 137(2):101–112, Feb 2011.

[75] C. Katsis and T. R. Akylas. On the excitation of long nonlinear water waves by a moving pressure distribution. part 2. three-dimensional effects. *Journal of Fluid Mechanics*, 177(1):49, Apr 1987.

[76] Irene M. Moroz. The kadomtsev–petviashvili equation under rapid forcing. *Journal of Mathematical Physics*, 38(6):3110–3122, Jun 1997.

[77] V. Petviashvili and O. Pokhotelov. *Solitary waves in plasmas and in the atmosphere.* 1992.

[78] A.R. Seadawy and K. El-Rashidy. Dispersive solitary wave solutions of kadomtsev-petviashvili and modified kadomtsev-petviashvili dynamical equations in unmagnetized dust plasma. *Results in Physics*, 8:1216–1222, Mar 2018.

[79] K Annou, S Bahamida, and R Annou. Spherical kadomtsev–petviashvili equation for dust acoustic waves with dust size distribution and two-charges-ions. *Pramana*, 76(3):513–518, Mar 2011.

[80] Alexis S Truitt and Christine M Hartzell. Simulating damped ion acoustic solitary waves from orbital debris. *Journal of Spacecraft and Rockets*, submitted.

[81] L. A. Ostrovsky and Yu. A. Stepanyants. Do internal solitions exist in the ocean? *Reviews of Geophysics*, 27(3):293, 1989.

[82] L. A. Ostrovsky and Y. A. Stepanyants. Internal solitons in laboratory experiments: Comparison with theoretical models. *Chaos: An Interdisciplinary Journal of Nonlinear Science*, 15(3):37111, Sep 2005.

[83] H. MICHALLET and E. BARTHÉLEMY. Experimental study of interfacial solitary waves. *Journal of Fluid Mechanics*, 366:159–177, Jul 1998.

[84] L. D. Landau. On the vibrations of the electronic plasma. *J. Phys.(USSR)*, 10:25–34, 1946. [Zh. Eksp. Teor. Fiz.16,574(1946)].

[85] Kashif Arshad, S. Mahmood, and Arshad M. Mirza. Landau damping of ion acoustic wave in lorentzian multi-ion plasmas. *Physics of Plasmas*, 18(9):92115, Sep 2011.

[86] G. J. Morales and Y. C. Lee. Effect of localized electric fields on the evolution of the velocity distribution. *Physical Review Letters*, 34(4):242–242, Jan 1975.

[87] Yashika Ghai, N. S. Saini, and B. Eliasson. Landau damping of dust acoustic solitary waves in nonthermal plasmas. *Physics of Plasmas*, 25(1):13704, Jan 2018.

[88] S. Oyama, C. Lathuillere, S. Maeda, and B. J. Watkins. Summer-winter dependences of day-night differences in the ion temperature in the polar upperfregion. *Geophysical Research Letters*, 31(5), Mar 2004.

[89] Roger Grimshaw. Internal solitary waves in a variable medium. *GAMM-Mitteilungen*, 30(1):96–109, Apr 2007.

[90] Junkichi Satsuma. N-soliton solution of the two-dimensional korteweg-devries equation. *Journal of the Physical Society of Japan*, 40(1):286–290, Jan 1976.

[91] B. B. Kadomtsev and V. I. Petviashvili. On the Stability of Solitary Waves in Weakly Dispersing Media. *Soviet Physics Doklady*, 15:539, December 1970.

[92] S. Ahmad, Ata ur Rahman, S. A. Khan, and F. Hadi. Damped kadomtsev–petviashvili equation for weakly dissipative solitons in dense relativistic degenerate plasmas. *Communications in Theoretical Physics*, 68(6):783, Dec 2017.

[93] S. Clarke, K. Gorshkov, R. Grimshaw, and Y. Stepanyants. Decay of kadomtsev–petviashvili lumps in dissipative media. *Physica D: Nonlinear Phenomena*, 366:43–50, Mar 2018.

[94] Christian Klein, Christof Sparber, and Peter Markowich. Numerical study of oscillatory regimes in the kadomtsev–petviashvili equation. *Journal of Nonlinear Science*, 17(5):429–470, Jun 2007.

[95] A.A Minzoni and N.F Smyth. Evolution of lump solutions for the KP equation. *Wave Motion*, 24(3):291–305, Nov 1996.

[96] Zhiming Lu and Yulu Liu. The generation of lump solitons by a bottom topography in a surface-tension dominated flow. *Zeitschrift für Naturforschung A*, 60(5):328–334, May 2005.

[97] Wencheng Hu, Wenhua Huang, Jie Shen, and Zhiming Lu. The generation of symmetric and asymmetric lumps by a bottom topography. *Wave Motion*, 75:62–71, Dec 2017.

[98] Aurel Bulgac, Michael McNeil Forbes, Michelle M. Kelley, Kenneth J. Roche, and Gabriel Wlazłowski. Quantized superfluid vortex rings in the unitary fermi gas. *Physical Review Letters*, 112(2), Jan 2014.

[99] N.A. Veretenov, S.V. Fedorov, and N.N. Rosanov. Topological vortex and knotted dissipative optical 3D solitons generated by 2D vortex solitons. *Physical Review Letters*, 119(26), Dec 2017.

[100] P Kelley. Solving a physics mystery: Those 'solitons' are really vortex rings. University of Washington. Available at `https://www.washington.edu/news/2014/02/03/solving-a-physics-mystery-those-solitons-are-really-vortex-rings/`, February 2014.

[101] Boris A. Malomed. (invited) vortex solitons: Old results and new perspectives. *Physica D: Nonlinear Phenomena*, 399:108–137, Dec 2019.

[102] Mark Garcia. Space debris and human spacecraft. NASA. Available at `https://www.nasa.gov/mission_pages/station/news/orbital_debris.html`, Apr 2015.